



Long-term AGN Variability Study for the Cherenkov Telescope Array Data Challenge

Amanda Evelyn de Araujo Carvalho

Master Dissertation

Advisor:

Ulisses Barres de Almeida

Rio de Janeiro, RJ

2020



Amanda Evelyn de Araujo Carvalho

Long-term AGN Variability Study for the Cherenkov Telescope Array Data Challenge

Master Dissertation

Dissertation presented in the post graduation program of Centro Brasileiro de Pesquisas Físicas as partial request for obtainment of degree in Master of physics.

Advisor:

Ulisses Barres de Almeida

Rio de Janeiro, RJ

2020

RESUMO

Os Núcleos Ativos de Galáxias (AGNs) são alguns dos objetos mais notáveis no céu de altas energias. Eles produzem poderosos jatos que são sítios excelentes para a produção e aceleração de partículas até muito altas energias. A astrofísica dos raios gama tem crescido muito nas últimas décadas revelando uma riqueza surpreendente de fenômenos no final do espectro eletromagnético. O futuro Cherenkov Telescope Array mudará nossa compreensão do Universo no regime de energia raios gama, aumentando em cerca de uma ordem de magnitude o número de AGNs detectados em VHE, e permitindo-nos compreender melhor os processos físicos nesses ambientes extremos.

O programa de monitoramento de AGNs do CTA nos ajudará na compreensão da complexa variabilidade do fluxo dessas fontes, que varia em escalas desde poucos minutos até vários anos. Este programa produzirá constantemente curvas de luz refinadas de longo prazo e espectros de alta qualidade, ao longo do tempo de operação do telescópio, por cerca de 30 anos, bem como fornecerá alertas para outras instalações para que possam seguir o alto estado de fluxo de energia em observações de vários comprimentos de onda.

Neste trabalho participamos do primeiro CTA Data Challenge (DC-1) - um conjunto de tarefas desenvolvido pelo Consórcio CTA com o objetivo de aprimorar o software de análise e o planejamento científico do observatório. Em nosso caso particular, estivemos focados no estudo de séries temporais e análise de variabilidade de AGNs, que se insere no programa de monitoramento do CTA, baseado na geração de curvas de luz das fontes de uma amostra de monitoramento pré-definida.

ABSTRACT

Active Galactic Nuclei are among the most remarkable objects in the Very High Energy sky. They produce powerful outflows which are excellent sites for the production and acceleration of particles up to and beyond the TeV regime. Gamma-ray astrophysics has grown enormously in the last decades, revealing an amazing richness in the Universe as seen from end of electromagnetic spectrum. The future Cherenkov Telescope Array will change our understanding of astrophysics in the gamma-ray regime, increasing in about one order of magnitude the number of detected VHE AGNs, and allowing us to better understand the physical processes taking place at these extreme environments. The AGN monitoring program of CTA will lead us to the comprehension of the complex flux variability of these sources, which show complex variability in multiple timescales, from few minutes to several years. This observational program will constantly produce refined long-term light curves and high-quality spectra throughout the operation time of the observatory, as well as provide alerts to other facilities so that they can follow-up the very high energy flux state in multi-wavelength observations.

This work was part of the first CTA Data Challenge (DC-1) – a set of simulation and data analysis tasks developed by the CTA Consortium with the goal of improving the CTA software and refining the CTA science case. In our particular case we focused in the study of time series and variability analysis of AGN as part of the CTA AGN monitoring Key Science Program, in which we successfully produced a set of light curves for the pre-selected sample of sources within the CTA KSP programme, and available in the CTA DC-1 sky model.

Dedico este trabalho a meus pais Edna e Jorge

Acknowledgements

Agradeço primeiro a Deus por ter me dado a oportunidade de participar deste trabalho. Depois agradeço meus pais a quem dedico este trabalho por nunca terem medido esforços para me ajudar nesta jornada. Sou grata também a meus irmãos, Gláucia e Eder, por serem sempre fontes de força e coragem, juntamente com a madrinha, Hevelen e todas as tias e primos, por todas as orações e palavras de carinho e aconchego.

Gostaria de agradecer também ao Ulisses por ser sempre me inspirar, iluminar e alegrar meus dias de trabalho através da sua paciência, dedicação e benevolência. Agradeço também ao Bernardo por ter me ensinado grande parte do que eu sei de análise de dados.

Por fim, não posso deixar de mencionar o Matheus por sempre me motivar com todo amor e nunca me deixar desistir. Ao professor Renato Las Casas que sempre me ajuda e impulsiona a chegar cada vez mais longe. E a todas minhas eternas amigas da MoP II por todo o carinho e apoio emocional. E por ultimo agradeço a todos os meus anjos que já não brilham mais aqui na Terra, mas fizeram parte de todo esse caminho comigo.

List of Figures

2.1	Structure of an Active Galactic Nuclei. Adapted from: [7].	10
2.2	Image of the galaxy NGC 4261 nucleus, where the gray scale represents the planetary camera calibrated image. Credits: [30]	14
2.3	Superluminal motion scheme	15
2.4	Classification and Unification scheme of AGNs developed by Urry and Padovani in 1995. Credits: [14]	17
2.5	Circinus Galaxy, an example of Seyfert type II galaxy observed by the telescope Hubble. Credits: [2]	18
2.6	Image of the quasar 3c273 taken from Sloan Sky Digital Survey (http://classic.sdss.org/iotw/archive.html)	18
2.7	Classification of AGN according with the radio and optical properties. Addapted from: [45]	19
2.8	LINER galaxy NGC4102. Credits: ESA/Hubble, NASA and S. Smartt (Queen's University Belfast)	21
2.9	First image of a black hole powered jet from the blazar 3C279 using the Event Horizon telescope(EHT). Credits:J.Y. Kim (MPIfR), Boston University Blazar program, and the EHT Collaboration.)	22
2.10	Motion of a charged particle in the presence of magnetic field. Credits: [43]	22
2.11	Cones of radiation emission at some points of trajectory of the accelerated particle. Credits: [43]	24
2.12	Vectors of the Synchrotron radiation projected in the plane of the sky. Credits: [43]	24
2.13	Faraday Diagram representing the inverse Compton scattering. Credits: [19]	25
2.14	First optical image of the jet of the galaxy M87 the image is a superposition of three CCD images in yellow, red and near-infrared (V, R and I). Credits:ESO	27
2.15	Optical jet of M87, images took by the HST over a period of four years. The angular velocity of the components is about ~ 23 mas/yr. Assuming that M87 is at distance of $D = 16Mpc$, the components velocities can reach $\sim 6c$. Addapted from:[44]	28
2.16	SED of the blazar Mrk 421 measured with Fermi and MAGIC telescopes. Adapted from:[23]	31

2.17	Blazar sequence. Where he fitted curves are analytic curves that was obtained assuming first that the ratio of synchrotron to Inverse Compton peak frequencies is constant and second that the amplitude of the inverse-Compton peak is proportional to the radio luminosity. Adapted from:[19]	32
3.1	Development of gamma-ray air showers. [3]	37
3.2	Polarization in a dielectric produced by a passage of a charged particle. (a) At low velocity (b) At high velocity. [31]	38
3.3	Huygens construction for Cherenkov front waves. Half Cherenkov Cone with angle $\Theta = \cos^{-1} \frac{1}{\beta n}$ for a particle traveling with $v > \frac{c}{n}$.Credits:[31]	39
3.4	In the figure above the solid lines represents the spectra of the Cherenkov light for different energies at 10 km of altitude, and the dashed lines represents the correspondents spectra at 2200 m of altitude. The UV-blue part of the spectra is modified due the Rayleigh-scattering of the air molecules with ($d < \lambda$). The photons with wavelength $\propto (\lambda^{-(1-1.5)})$ suffer Mie scattering due the presence of aerosols and water droplets in the atmosphere, in addition, the light with $\lambda < 280nm$, is completely attenuated by absorption of ozone molecules presents in the atmosphere above 10 km of altitude, with introduces a cut-off of the spectrum. Credits:[47]	40
3.5	Cherenkov lateral radius of the light pool at the ground for different altitudes with related Cherenkov angles. Credits: Tibaldo L.[1]	41
3.6	Schematic development of the hadronic shower. Credits:[47]	42
3.7	Left: electromagnetic gamma shower. Right: Hadronic proton shower. The initial energy for both particles is 100 GeV. As expected the hadronic shower is much more spread than the electromagnetic. In fact, the hadronic shower looks like a collection of sub electromagnetic showers. Credits: [47]	44
3.8	Hillas parameters used to described the Cherenkov image at the camera.Adapted from: [25]	45
3.9	Example of an array of telescopes observing a Cherenkov Shower simultaneously. Adapted from: [25]	46
3.10	Stereo parametrization scheme used for the reconstruction of the Cherenkov shower. Credits: [27]	47
3.11	Layouts of the telescopes arrays in both hemispheres.Credits: CTA [4]	48
3.12	In the Left are the three different SST prototype designs, in the medium the two MST prototype designs and in the right the LST prototype design. Image credit: Gabriel Pérez Diaz, IAC [4]	49

4.1	Region proposed for the extragalactic survey in light blue. The GPS is indicated in darker blue. The red points are a hypothetical example of the sources to be detected in the survey. The black points are the extragalactic and unidentified Fermi-LAT hard-spectrum sources (2FHL catalogue) and the green points show the AGNs that have already been detected so far by IACTs. Credits [22].	59
4.2	Simulated events for AGN monitoring program in the sky. Credits: Jürgen Knödlseder, 08/25/2017	60
4.3	FITS header of the light curve file, where we can get information such as the dimension, length of the table and the reference MJD where observations started.	64
4.4	Extract of the original light curve with the columns of norm and time. The time in the table is given in seconds so it was necessary to convert the TIME column to MJD dividing by 86400 s and adding the reference MJD where the observation started.	65
4.5	Overview of all the tools available in ctools. Credits: [32]	68
4.6	1dc folder structure. Inside the caldb folder is contained the instrument response functions that are necessary for the analysis of the simulated CTA data, in the data folder there is the calibrated, reconstructed and background reduced event data. The files obs_agn_baseline.xml, obs_egal_baseline.xml, obs_gc_baseline.xml, and obs_gps_baseline.xml are observation definition files containing a list of observations. Lastly the models folder contains the definitions of all source and background models that were used for simulating the data. Credits: [5]	70
4.7	Format of the event file	71
4.8	Sky map of the source PKS 0716+714	74
4.9	output of the csresmap tool	77
4.10	output of the cslightcrv tool	78
4.11	Header of the LIGHTCURVE table	78
4.12	Light Curve of the source PKS0716+714 generated with ctools analysis	79
4.13	Light curve of the source PKS 0716+714	80
4.14	Energy dispersion matrix for the source PKS0716+714	81
4.15	Light curve of the source 3C66A in 30GeV - 50TeV with energy dispersion.	83
4.16	Residual map of the source 3C66A	83
4.17	Light curve of the source B1222+216 with energy dispersion	84
4.18	Angular Resolution of CTA North	85
4.19	Light curve of the source PKS2233-148 with energy dispersion	86
4.20	Data of the source PKS2233-148 available: model(green), analysis(red)	86
4.21	Light curve of the source PKS 1454-3541:	87
4.22	Data from the source PKS 1454-3541: model(green), analysis(red)	87
4.23	Light curve of the source PKS 1502+106	88
4.24	Data from the source PKS1502+106:model(green), analysis(red)	88

4.25	Residual fit of the source PKS 1502+106	90
4.26	Spectral fit of the source PKS 1454-354. The color black represents the data from the analysis and blue the simulated source	92
A.1	Light curve of the source PKS1510-189. This analysis in general overestimate a little the simulated model during the long term component and during the flare.	95
A.2	Light curve of the source Mrk421. This light curve also shows a overestimation of the flux during the flares, revealing a problem in the algorithm during the background subtraction.	96
A.3	Light curve of the source Ton 599. The long term component of this light curve is good, but the analysis overestimate the source during the flare	96
A.4	Light curve of the source PKS1424-41. This light curve always overestimate the simulated model.	97
A.5	Light curve of the source 3C279 with energy dispersion	97
A.6	Light curve of the source PKS 0454-234 with energy dispersion	98
A.7	Light curve of the source S41749+70.	98

List of Tables

3.1	Main characteristics of CTA telescopes and the three cameras prototypes, where PMT is photomultiplier and SIPMT is silicon photomultiplier. [4]	51
4.1	AGN simulated sources for the long term monitoring	61
4.1	All the point sources have a power-law type spectrum, where the spectral index is the best fit photon number power-law index and the pivot-energy is the energy at which the error on differential flux is minimal. The flux was obtained integrating the photons from 10 to 500 GeV according to 1FHL. The data of the first four sources were obtained from TeVcat catalogue(http://tevcat.uchicago.edu/), the fifth to ninth sources were taken from 2FHL(https://fermi.gsfc.nasa.gov/ssc/data/access/lat/2FHL/) and the remaining ones from 1FHL (https://www.ssdsc.asi.it/fermi1fhl/)	62
4.2	Model file of the source PKS0716+714 containing the source type, spectral, spatial and temporal models. Where RA is the right ascension coordinate of the source, DEC is the declination, Prefactor and Index are the components of the power law function used to describe the source, already described above, and lastly the light curve file contain the values of time and normalized flux which needs to be multiplied by normalization value and scale to recover the real value. To recover all the different parameters real value it is necessary to multiply each value by the correspondent parameter scale.	64
4.3	Model file of the source Ton599 containing the source type and the spectral model file. Where RA is the right ascension coordinate of the source, DEC is the declination, Prefactor and Index are the components of the power law function used to describe the source, already described above, and lastly the light curve file contain the values of time and normalized flux which needs to be multiplied by normalization value and scale to recover the real value. To recover all the different parameters real value it is necessary to multiply each value by the correspondent parameter scale. The spectra file contains columns of energy and the correspondent flux for each energy value.	66

4.4	IRFs available in the first CTA Data Challenge for the northern and southern arrays, they were optimised for an exposure time of 50 hours and two different zeniths of 20 °and 40 °, specified in the IRF names respectively as z20 and z40.	71
4.5	Output log event file from the ctselect tool. Where RoI is the region of interest which in this case is 5°around the central position of the source.	72
4.6	Output XML file from the tool ctselect with details of each observation. Response specifies the instrument response function that applies to the event file. The IRF are stored in the caldb folder, its function is to classify the measured events into source and those attributed to any background.	72
4.7	Likelihood model of the source PKS0716+714 containing the source spectral parameters and the background. Where RA is the right ascension position of the source and DEC is the declination. The spectrum type of the source is described by a simple power law function where the pivot energy is the energy at which the function was normalized. To recovery the real values of the parameters they value needs to be multiplied by its correspondent parameter scale.	75
4.8	Light Curve parameters	80

Contents

Resumo	i
Abstract	iii
Dedication	v
Acknowledgements	vii
List of Figures	ix
List of Tables	xiii
Contents	1
1 Introduction	5
1.1 The Very High Energy Gamma-Ray Sky	5
2 Active Galactic Nuclei	9
2.1 Active Galactic Nuclei	9
2.2 Morphology	9
2.2.1 Supermassive Black Hole	10
2.2.2 Accretion Disk	11
2.2.3 Broad Line Region	12
2.2.4 Narrow Line Region	13
2.2.5 Torus	13
2.2.6 Jets	13
2.2.6.1 Beaming	15
2.2.7 Radio Loud and Radio Quiet	16
2.3 Classification	16
2.3.1 Seyfert Galaxies	17
2.3.2 Quasi-Stellar Objects	18
2.3.3 Radio Quiet and Radio Loud/Jetted and Non-Jetted AGN	19
2.3.4 Radio Galaxies	20
2.3.5 LINERs	20

2.3.6	Blazars	21
2.4	Pancromatic Jets	21
2.4.1	Synchrotron Radiation	22
2.4.2	Inverse Compton	24
2.4.3	Shock particle acceleration	26
2.4.4	Optical Jets	27
2.4.5	X-Ray Jets	28
2.4.6	Gamma-ray Jets	29
2.4.6.1	Hadronic Models	29
2.4.6.2	Leptonic Models	29
2.5	Blazars	30
2.5.1	Blazar Sequence	30
2.5.2	Gamma-ray Blazars	32
2.5.3	Propagation of gamma-rays through the Extragalactic Background Light	33
2.6	Blazar Variability	34
3	Cherenkov Telescope Array	35
3.1	The Cherenkov Telescope Array	35
3.2	Cherenkov Radiation	36
3.3	Imaging Atmospheric Cherenkov Telescopes	40
3.3.1	Hadronic Shower	42
3.3.2	Gamma-Hadron separation	43
3.3.3	Imaging technique	43
3.3.4	Stereoscopy	45
3.3.5	Shower Reconstruction	46
3.4	CTA Observatory	47
3.5	Extragalactic Survey	52
3.6	AGN monitoring	53
4	CTA Data Challenge	55
4.1	Introduction	55
4.2	Data Challenge	57
4.3	Data Model	63
4.4	Ctools	66
4.4.1	Data structure	67
4.5	Methods	69
4.5.1	Light Curves	80
4.6	Results:	82
4.6.1	Source 3C66A:	83

4.6.2	Sources PKS0716+714, B1222+216, PKS1510-089, Mrk421, Ton 599, PMNJ2345-1555, 3C279, S41749+70, PKS 0454-234 and PKS 1424-41	84
4.6.3	Sources PKS1454-354, PKS2233-148 and PKS 1502+106	84
4.7	Discussion:	87
5	Conclusion	93
A	Light Curves	95
	Bibliography	101

Chapter 1

Introduction

1.1 The Very High Energy Gamma-Ray Sky

This dissertation is focused on the high-energy gamma-ray Universe and more specifically in its extreme astrophysical sources. There are today approximately 180 VHE gamma-ray sources detected with ground-based telescopes [22]. The majority of those are Active Galactic Nuclei (AGNs). AGNs are extremely luminous galaxies, whose luminosity derives from processes happening at the center of the galaxies, and is dominated by non-thermal radiation. The AGNs are separated into several classes according with their observed characteristics. The vast majority of the AGN detected sources belong to the sub-class of Blazars [22]. Blazars are characterized by the presence of a strong Doppler boosted non-thermal radiation, coming from plasma outflowing at relativistic speeds from the central engine. This outflow happens in the form of large-scale collimated structures, namely jets, which can be extended for several Mpc in length and are aligned with the line of sight.

Blazars are believed to be very efficient particle accelerators, and to be potential accelerators of cosmic-rays inside their relativistic jets, via mechanisms not yet completely understood, but that are likely associated to internal shocks developing in the plasma flow[19]. In fact, understanding the origin of these mechanisms is one of the principal objectives in observing these sources at gamma-ray energies. An advantage of using gamma-rays for such studies is that we can directly trace the regions of the source where energy dissipation and particle acceleration is taking place, in this way tracing the potential sites of cosmic ray production. Direct observations of the particles cannot do this, since cosmic rays are deflected from a straight path as they travel towards Earth, due intervening magnetic field lines. Assuming in first order that the blazar standard emission is composite of synchrotron and inverse-Compton mechanisms, we can probe electron populations of energies of the order of 10^{14} and protons with energies up to 10^{20} (see chapter 2).

Very-high energy gamma-ray astrophysical processes started being studied in 1989, when Weekes detected for the first time gamma-rays with energies of the order of \sim TeV

coming from the Crab Nebula using the IACT technique [25]. In 1991, NASA launched EGRET (Energetic Gamma Ray Experiment Telescope) with the purpose of collecting data on gamma-rays ranging from 30 MeV to 30 GeV. Then, in 2008 the Fermi-LAT telescope was inaugurated, with a good energy resolution between 100 MeV to 100 GeV, however, for photon energies above 100 GeV the flux is so low that its collection area becomes prohibitive for the study of most source classes. At such energies, ground-based gamma-ray astronomy is favoured instead, due to the much higher photon collection area achieved through the imaging atmospheric Cherenkov technique.

When the gamma-rays reach the atmosphere, they create a pair electron-positron due to their interaction with the electrical field of the air molecules, and creates a cascade of particles that propagates downwards through the atmosphere (see chapter 3 for a detailed explanation). This interaction generates a shower of particles which in turn produce Cherenkov radiation which arrives at the ground with a footprint which extends over several 100 m [29]. The Cherenkov radiation is captured by the ground telescopes and, depending on the image properties of the Cherenkov photons collected, properties of the primary gamma-ray such as energy and direction of arrival can be reconstructed. Since the 1989 discovery by the Whipple telescope, almost two hundred VHE gamma-ray sources have been discovered using Cherenkov telescopes.

A turning point on the evolution of the technique was the use of a method called stereoscopy, a method by which several telescopes are spread on the ground and combine their simultaneously detected Cherenkov light from a given event to allow for the tridimensional reconstruction of the shower, granting better precision in the derivation of the primary gamma-ray properties [25]. Nowadays, the IACT telescopes in operation are represented by three major observatories: H.E.S.S located in Namibia, VERITAS in the United States of America, and MAGIC in Spain. However, due to the necessity of improving the sensitivity of the telescopes to detect more sources and collect more details of the already-detected ones, the astronomical community gave rise to a global consortium with the objective of building the next-generation IACT observatory, the Cherenkov Telescope Array (CTA). The CTA will be the largest and most sensitive ground-based instrument built until today in the very-high energies [22]. To cover the very ample energy range from 30 GeV to 50 TeV, CTA will be composed by circa one hundred telescopes of three types – Large, Medium and Small-Sized Telescopes – spread in two sites, one in the Northern and another in the Southern hemisphere. The CTA Observatory operations are expected to start in 2022 and the completion of the project construction is expected to happen by 2025. Until there, the data from the prototypes will be available for the consortium to help test and improve the CTA software, and to do some timely science.

CTA is expected to discover more than one thousand new gamma-ray sources in the sky, increasing in at least one order of magnitude the number of detected Blazars, which will help in the understanding of the physics behind these remarkably energetic sources [22].

Blazars are very interesting objects due to their complex spectral variability, which happens in bursty events of short timescales, that can vary from minute-duration spikes to long modulations in the scale of weeks in the high-energies. Although the current IACTs are able to detect variability on the scales of minutes for very extreme events, CTA will detect important temporal features like minimal variability times and the periodicity of the burst-like events at a much greater rate, which could provide some answers to the question of the size and possible location of the VHE emission region, as well as elucidate the physical mechanisms behind VHE radiation production, as well as particle acceleration.

A long-term monitoring program of AGNs such as will be conducted by CTA is extremely useful to help us understand the complex variability properties of these objects. The long-term monitoring program of CTA has been planned for several reasons, amongst them the necessity to identify the quiescent states of a sample of AGNs and estimate their duty cycle, as well as identify the various potential emission zones of blazar jets, and to find their location relatively to the evolving jet morphological features. Besides that, with the CTA long-term monitoring we should be able to clarify whether the VHE variability is dominated by the jet physics or by the accretion flow in the disk [22].

The central focus of this work is in the preparation of the long-term monitoring program of CTA, in particular the verification of the analysis software and the observational plan through our participation in the first CTA Data Challenge. The long-term monitoring program of AGNs has the goal to provide long-term light curves for a well-sampled simulated set of sources (see chapter 4) covering several types of AGNs (UHBL, HBL, IBL, LBL, FSRQs, and radio galaxies). Each source will be observed on average for ~ 30 min once a week with the full CTA array. With the long-term light curves, and the regular observations, it will be possible to track the flux variability of all sources. Even though the study of long-term flux variation is the focus of this program, using the Small-sized telescopes (SSTs) in the southern array during the observations will permit extending the spectral coverage of HBLs and UHBLs during high states above 10 TeV with good sensitivity, testing the limiting energy of these sources[22].

This thesis is organized as follows: Chapter 2 gives an introduction to AGNs and the major physics topics processes necessary to explain these extreme environments, and is mainly focused on blazars and jets, which are the central subjects for CTA. In chapter 3 we give a better description of how CTA will work, as well as introduce the AGN monitoring program, which is the focus of this work. Following that, in chapter 4 we describe the CTA software, the CTA Data Challenge (DC) – which is a set of simulated high-level science data tasks, with the goal of preparing and verifying the analysis tools and software. In our contribution to the DC, we were tasked with the study of the long-term AGN variability component of CTA science, whose results we present here, describing the set of light curves of the simulated sources. Lastly in chapter 5, we present the conclusions of our work.

Chapter 2

Active Galactic Nuclei

2.1 Active Galactic Nuclei

Active Galactic Nuclei (AGN) are extreme luminous galaxies, being sometimes more than a thousand times brighter than normal galaxies. This luminous process happens at the center of the galaxy and can not be explained by the light of the stars, in view of their vast bandwidth spectra, suggesting that their emission is dominantly non-thermal. This amount of radiation coming from such a small region as is the galactic nucleus, causes AGN to be the most powerful and extreme astrophysical phenomena in the universe.

There are today approximately 180 VHE sources detected with ground based telescopes and from these sources $\sim 40\%$ are AGNs [22]. Among these AGNs, 5 of them are radio galaxies and the remaining majority are Blazars. Blazars are very interesting objects due to their complex spectral variability, which happens in bursty events of short timescales, of the order of minutes, to long modulations in the scale of years. The future ground based Cherenkov Telescope Array (CTA) will improve in at least one order of magnitude the number of detected Blazars, which will help in the understanding of the physics behind these remarkably energetic sources. Our purpose in this chapter is to give a brief introduction of the morphology and classifications of AGNs, then focus on Blazars and their outflows (jets) which are fundamental to understanding AGN variability.

2.2 Morphology

The AGN is composed by an accreting supermassive Black Hole in the center of the host galaxy. The accretion disk around the SMBH is further surrounded by gas clouds and an obscuring torus of dust. In some cases, there is the presence of jets, which may generate radio-bright lobes at large distances from the AGN, towards their termination points (see fig. 2.1). The AGN phenomenon happens when the disk material falls onto the SMBH, releasing in the process large amounts of radiation as a result to thermalised or relativistic particle

populations that are accelerated in the process.

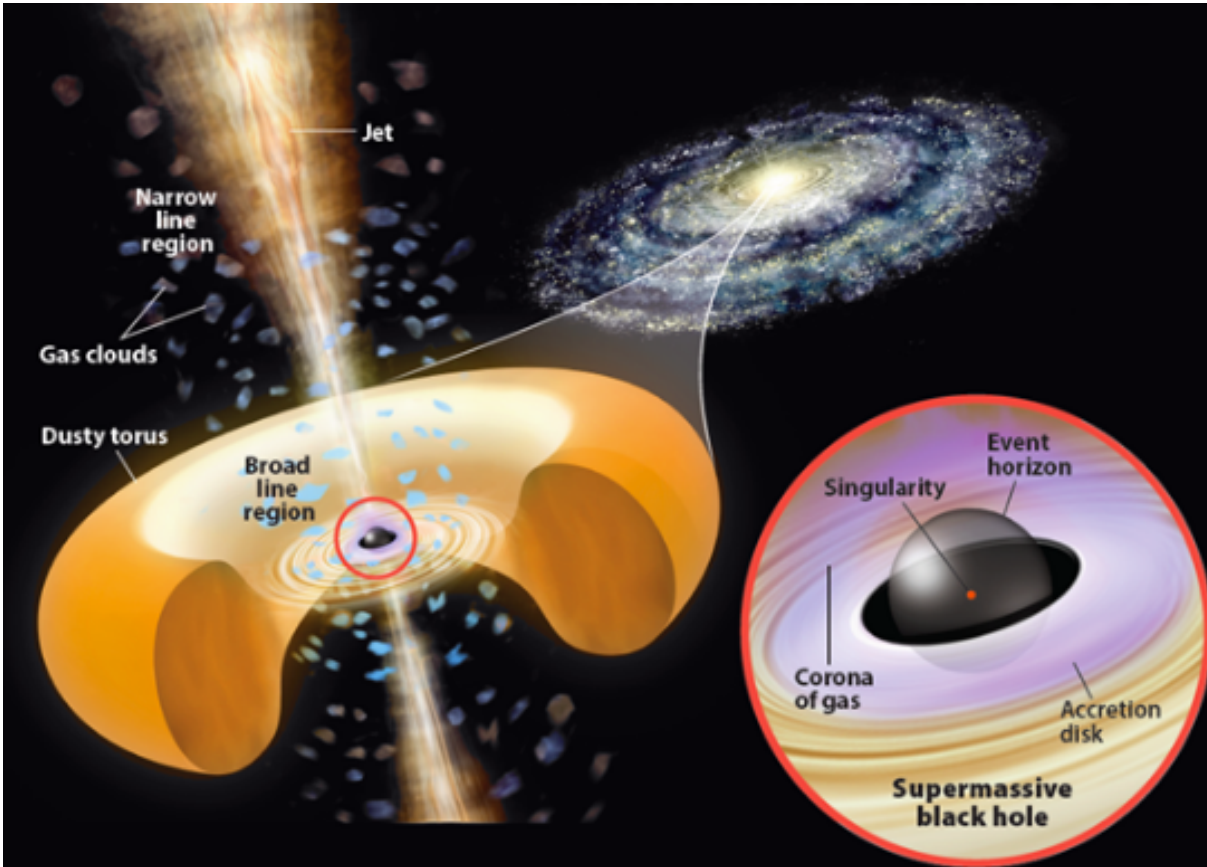


Figure 2.1: Structure of an Active Galactic Nuclei. Adapted from: [7].

2.2.1 Supermassive Black Hole

There are several evidences for the existence of SMBHs in the center of galaxies. One of them comes by looking at the movement of the innermost stars, as is the case of the Milk Way. Another way is by looking at the luminosity variability of some AGNs. Considering a typical variability of ~ 1 day, we can determine the spatial extent of the source, given that the variability timescale is proportional to the source size, as constrained by the time needed for information to travel over the entire emitting source, or at least the most of it. Thus: $R < c\Delta t \sim 1 \text{ lightday} \sim 3 \times 10^{15} \text{ cm}$, where R is the size of the source, c is the velocity of light and Δt is the temporal variability. This radius is comparable with the Schwarzschild radius (r_s) of a black hole with $10^9 M_\odot$ which is $r_s \sim 3 \times 10^{14} \text{ cm}$. Considering that the production of energy in AGN comes only from the accretion of matter onto a SMBH, then we have that the radiation produced near the Schwarzschild radius propagates outwards and interacts with the infalling material. In this interaction, the radiation transfers momentum to the matter, which can be translated into an outward radiation force. For the material to be able to fall into the SMBH the gravitational force needs to be larger than the radiation force.

For simplicity, considering a completely ionized gas, where the interaction is mostly due to scattering of photons by free electrons (Thomson scattering), the mean radiation force on a single electron at distance r from the center is:

$$F_{rad} = \sigma_e \frac{L}{4\pi r^2 c} \quad (2.1)$$

where $\sigma_e \sim 6.65 \times 10^{-25} \text{ cm}^2$ is the Thomson scattering cross-section, L is the luminosity and c is the velocity of light. Satisfying the condition where $F_{rad} \leq F_{gravitational}$ we have:

$$\sigma_e \frac{L}{4\pi r^2 c} \leq \frac{GM_e m_p}{r^2} \quad (2.2)$$

$$L \leq \frac{4\pi G c m_p}{\sigma_e} M_e \quad (2.3)$$

$$L \approx 1.26 \times 10^{38} (M_e / M_\odot) \text{ erg s}^{-1} \quad (2.4)$$

where L is the Eddington luminosity of a black hole of mass M_e . Therefore, a lower limit of the SMBH mass can be derived considering that the Eddington luminosity is proportional to M_e , thus:

$$M_e > M_{edd} := \frac{\sigma_e}{4\pi G c m_p} L \approx 8 \times 10^7 \left(\frac{L}{10^{46} \text{ erg/s}} \right) M_\odot \quad (2.5)$$

2.2.2 Accretion Disk

The gas falling into the SMBH loses potential energy and converts it into kinetic energy. Due to the angular momentum, the falling material cannot fall directly to the SMBH. Instead it rotates around it, while frictioning and transferring momentum to other particles of the gas. This interaction results in a disk-shaped gas configuration oriented perpendicular to the direction of the angular momentum vector. The disk rotates differentially, with Keplerian velocity, and this causes the gas to heat up by internal friction and to radiate. Furthermore, this friction also causes a slight deceleration of the rotational velocity, causing the gas to slowly move inwards.

According to Virial's theorem, the infalling material will radiate half of the potential energy with luminosity:

$$\Delta L = \frac{GM_\bullet \dot{m}}{2r^2} \Delta r \quad (2.6)$$

where M_\bullet is the mass of the SMBH, \dot{m} is the accretion rate, (which is the falling mass into the SMBH per unit time). If there is enough time for thermal equilibrium to happen, the local disk emission will radiate as a black body with temperature as [44]:

$$T(r) = \left(\frac{GM_\bullet \dot{m}}{8\pi\sigma_{SB} r^3} \right)^{\frac{1}{4}} \quad (2.7)$$

valid in the range where $r \gg r_S$.

From this analysis we can conclude that inwards, the temperature of the disk increases $\propto r^{-\frac{3}{4}}$. Generally, the total emission of the disk can be approximated as a superposition of black bodies for different rings dR at different temperatures. Therefore, the resulting spectrum has a broader energy distribution, extending from the external part in blue/UV band to the inner part in the X-ray band. In this way one could think that the observed variability in x-rays is related to the size changes in the inner structure of the SMBH [19].

2.2.3 Broad Line Region

The Broad Line Region (BLR) is the hotter, deeper region inside the SMBH gravitational well, where broad emission lines are produced due to intense movement of the gas. The gas that emits these lines is heated by the radiation that comes from the disk and, in general, has large bulk velocities of $\sim 10000 \text{ km/s}$. These velocities can be measured from the width of the velocity distribution of the components in the emitting region. Considering the gas at a distance r from the SMBH, the characteristic velocities of the emission lines are:

$$V_{rot} \sim \sqrt{\frac{GM_{\bullet}}{r}} = \frac{c}{\sqrt{2}} \left(\frac{r}{r_S} \right)^{-\frac{1}{2}} \quad (2.8)$$

For a velocity of $v \sim c/30$, the radial distance is:

$$\left(\frac{r}{r_S} \right) \sim 500$$

Then the broadening of the emission lines are produced by Kepler rotation when the radius is $\sim 1000r_S$.

Among the allowed broad lines are also semi-forbidden emission lines as CIII] and NIV. The classification into forbidden, semi-forbidden and allowed transitions is made using quantum mechanical transition probabilities, or the resulting mean time for a spontaneous transition happen followed by radiation. Allowed transitions corresponds to electric dipole radiation, which has a large transition probability, and the lifetime of the excited state is small, typically around 10^{-8} s . For forbidden transitions, the time-scales are usually larger $\sim 1 \text{ s}$, because their transition probability is substantially lower. The semi-forbidden transitions have a lifetime between these two extremities. To distinguish between these kinds of transitions, a double square bracket is used for forbidden transitions (as [OIII]), while for semi-forbidden lines is used a single square bracket (as CIII]).

Because of the high temperature in the BLR, the collisional de-excitation rate of the atoms are higher, and no forbidden lines are observed. This, combined with model calculations give us the estimation of the density of the gas of $\sim 3 \times 10^9 \text{ cm}^{-3}$ [44]. Furthermore, it is also possible to estimate the temperature of the emitting region from the ionization stages of the elements, which in this case is $\sim 20000 \text{ K}$. Adding it all up, together with appropriate photoionization models, it is possible to measure the volume of the emission region of the

gas. It turns out that the estimated volume of the gas is much smaller than the total volume of the BLR. This indicates that the volume of the BLR is concentrated in gas clouds instead of the gas being spread homogeneously over the entire volume of the AGN.

2.2.4 Narrow Line Region

Besides the BLR, most AGNs also show some narrow emission lines. The Narrow Line Region (NLR) is the outer region of the central engine, where the narrow emission lines are produced. These lines are also sustained by the radiative flux originated in the disk and have a typical width of $\sim 400 \text{ km/s}$. The classic lines observed in the NLR are $\text{Ly}\alpha$, CIV, and the forbidden [OIII]. The presence of these forbidden lines suggests that the density of the gas in the NLR is lower than in the BLR because in this case the time between two collisions is bigger than the average lifetime of the forbidden transitions. The NLR can be extended over $\sim 100 \text{ pc}$, and for this reason, no variability of the narrow line intensities has been found until today.

The morphology of the NLR is two cone-shaped areas at opposite poles of the AGN, which indicate that the ionization in AGNs is anisotropic, depending directly on the direction of the continuum radiation. The temperature of these regions is about $\sim 16000 \text{ K}$, and together with information on their density, a structure of clouds also emerges here.

2.2.5 Torus

The first dusty torus image was taken in 1993 [30] by Jaffe et al., using the space telescope Hubble, observing the galaxy NGC 4261 (see fig. 2.2).

The torus is composed of an opaque material around the central engine. According to Mason [36] the torus is small, in the way that its emission never been resolved at $\sim 0.3''$ which is the angular resolution of some mid-IR ground-based telescopes. The torus is also clumpy at small scales, evidence of which is present by luminosity changes tied to variable column densities, as discrete clouds cross the line of sight [36]. Observation in the IR suggests that in larger scales the torus is structured, the emitting region is distributed in a disk perpendicularly oriented to the NLR, and extended along the polar direction. This component is the most responsible for the obscuration, and the collimation of the outgoing radiation. Finally, the torus is dynamic, being composed of material that is coming in or out from the SMBH.

2.2.6 Jets

Jets are linearly extended structures, with sizes of up to $\sim 1 \text{ Mpc}$, often showing some internal structure as twists and knots. They transport energy and connects the core of the SMBH with the cosmic environments.

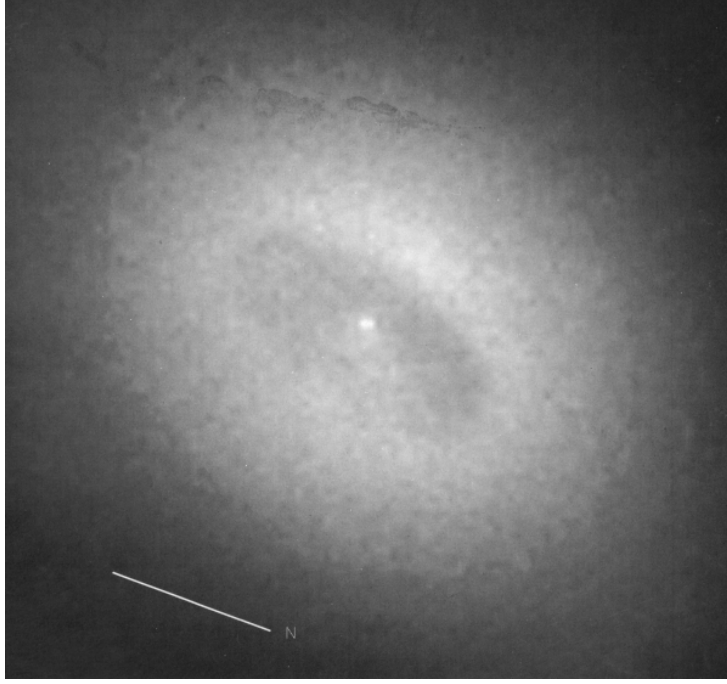


Figure 2.2: Image of the galaxy NGC 4261 nucleus, where the gray scale represents the planetary camera calibrated image. Credits: [30]

In 1964, J. Terrell demonstrated that the non-thermal emission in compact extragalactic sources came from relativistically moving plasma, and was associated to the observation of the so called superluminal motion. The superluminal motion is based on the fact that the relative motions of the components of the plasma are observed at apparent superluminal velocities. Consider a portion of the radiating plasma moving from the central engine at a distance D , with velocity v and angle ϕ with respect to the line-of-sight (see Fig.2.3).

Consider that in the time $t = 0$ the portion of plasma is close to the core. Then at the time $t = t_e$ the plasma has a distance vt_e from the initial position, then the observed separation is $\Delta r = vt_e \sin\phi$. At the time t_e the photons have a smaller distance from the observer than at $t = 0$. This implies that the photons emitted at different times will reach the observer at:

$$\Delta t = t_e - \frac{vt_e \cos\phi}{c} = t_e(1 - \beta \cos\phi) \quad (2.9)$$

where $\beta := \frac{v}{c}$. Consequently, the apparent velocity (v_{app}) of the moving jet on the sky is:

$$v_{app} = \frac{\Delta r}{\Delta t} = \frac{v \sin\phi}{1 - \beta \cos\phi} \quad (2.10)$$

We can obtain the maximum apparent velocity when the condition $(\sin\phi)_{max} = \frac{1}{\gamma}$ where $\gamma = (1 - \beta^2)^{\frac{1}{2}}$ is the Lorentz factor. Then, the maximum apparent velocity is: $v_{app} = \gamma v$

Considering $\beta_{app} = \frac{v_{app}}{c}$, the superluminal motion occurs when $\beta_{app} > 1$.

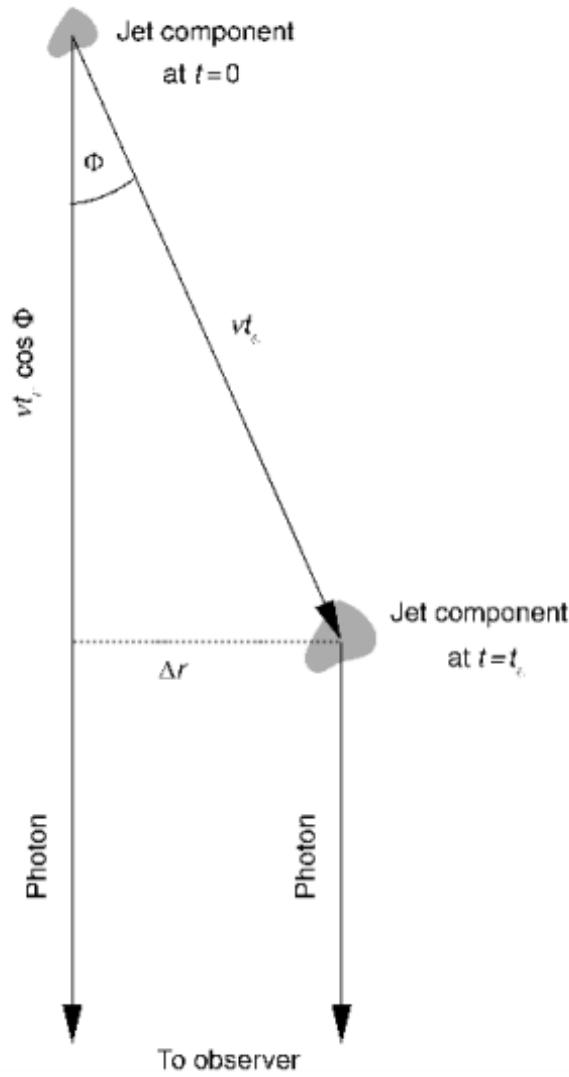


Figure 2.3: Superluminal motion scheme

2.2.6.1 Beaming

Another important effect that happens with the source due the relativistic motion is the beaming of the radiation. The beaming is explained by Special Relativity which says that a moving source emits isotropically in its rest-frame, but in another frame the emission pattern is anisotropic and the angular distribution depends on its velocity. Thus the emission of the radiation happens preferentially in the direction of the velocity vector of the source, which turns the source brighter if it moves in the direction of the observer by a factor of:

$$D_+ = \left(\frac{1}{\gamma(1 - \beta \cos \phi)} \right)^{2+\alpha} \quad (2.11)$$

compared with the source in the rest-frame, where α is the spectral index. This effect makes the jet pointing towards us to have its flux amplified with respect to the counter-jet. In this case the radiation of the jet is weakened by a factor:

$$D_- = \left(\frac{1}{\gamma(1 + \beta \cos \phi)} \right)^{2+\alpha} \quad (2.12)$$

This can explain why the jets most of the times appear to be one-sided.

2.2.7 Radio Loud and Radio Quiet

The morphology of the AGNs in the radio regime depends on the observed frequency and usually can be very complex, consisting of several different extended source components and one compact central one. In general, the extended source is observed in the form of two radio lobes situated more or less symmetrically around the optical position of the AGN. Frequently, these lobes are connected to the central core by jets. The observed length-scales of the total extent of the radio source can reach values of up to 1 Mpc.

There are two classes of AGNs: the “radio-loud” (RL) and the “radio-quiet” (RQ). These classifications were made by Sandage in 1965, who realised that there were many similar strong radio sources in the sky that were never been detected by radio telescopes at that time. Later it was understood that these sources were “radio-faint”. Indeed, for the same optical power the radio powers of the radio quiet (RQ) quasars are a few orders of magnitude smaller than those of their radio loud (RL) counterparts. In fact, this is how radio quiet quasars are characterised: relatively low radio-to-optical flux density ratios ($R \lesssim 10$) and radio powers ($P_{1.4GHz} \lesssim 10^{24} WHz^1$) [38]. More than that, it is important to make clear that the two classes represents intrinsically different objects. The RL AGNs emit a large fraction of their energy non-thermally over the whole electromagnetic spectrum while the multi-wavelength emission of the RQ AGNs is dominated by thermal emission, related with the emission of the accretion disk. The most impressive difference between the two classes lies in the hard X-ray to γ -ray band: Most of the RL sources emit all the way up to GeV and TeV, while most of the RQ sources have a sharp cut-off at energies $\lesssim 1$ MeV. Furthermore, no RQ AGN has ever been detected in γ -rays with the exception of NGC 1068 and NGC 4945, two Seyfert galaxies in which the γ -ray emission is thought to be related to their starburst component [38].

Finally, according with Padovani in 2017 [38], the biggest differences between the two classes is the presence (or absence) of a strong relativistic jet. In this way, the relative strength of the radio emission between the two classes is just a consequence of this fundamental physical difference.

2.3 Classification

In 1995 Urry and Padovani developed a system to classify the AGNs according to their orientation to the line of sight, and the amount of luminosity irradiated. The scheme represented in the fig. 2.4 shows how the different types of AGN are related with the way that the observer is looking at the jet. If the observer is viewing the jet face-on, it will see the non-thermal radiation dominating the spectrum of the source, and blazars and flat spectrum

radio quasars (FSRQ) will be seen. As the observer's line of sight moves away from the jet, it will start to see the accretion disk and broad line region, and objects such as Quasars and Seyfert galaxies are seen. When the observer is at side view, the torus will obscure the radiation from the center of the AGN and only objects such as Narrow line radio galaxies (NLRG) and Seyfert type 2 galaxies can be seen.

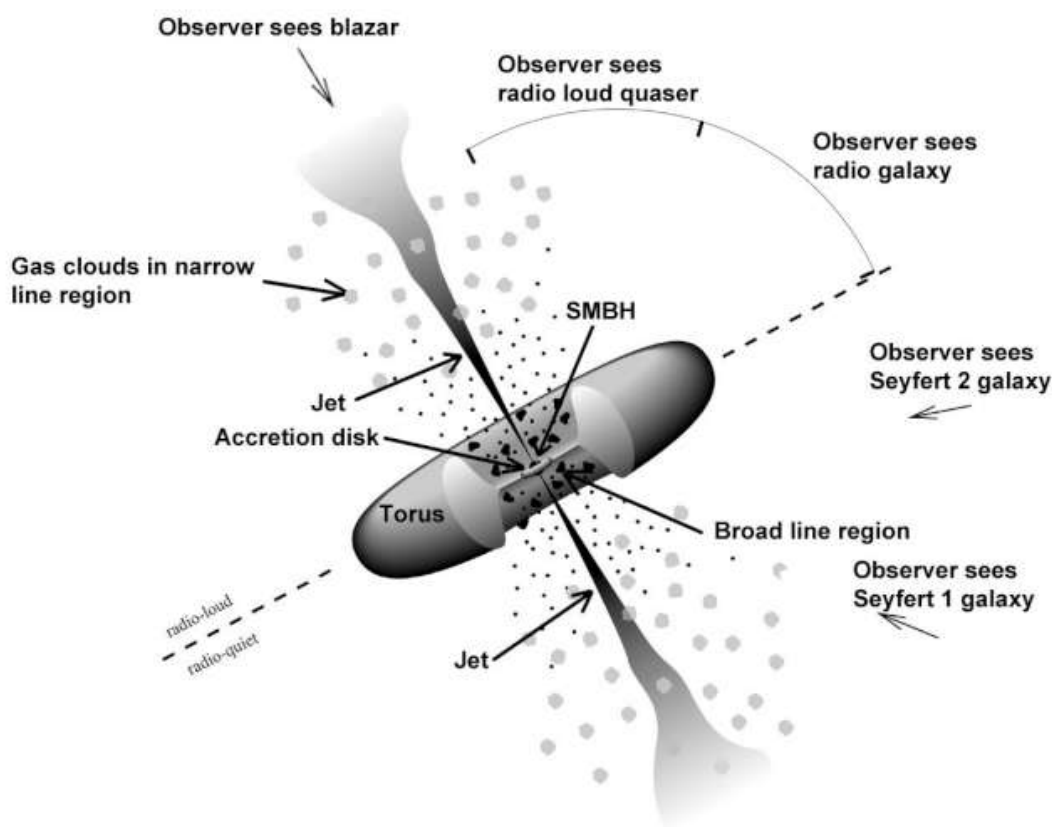


Figure 2.4: Classification and Unification scheme of AGNs developed by Urry and Padovani in 1995. Credits: [14]

2.3.1 Seyfert Galaxies

Seyfert Galaxies were discovered by Carl Seyfert in 1943, who noticed that the optical spectra of several galaxies were dominated by nuclear broad emission lines. Their luminosity is lower compared with other AGNs, being possible to observe the host galaxy. Seen through a big telescope, Seyferts look like normal spiral galaxies with a bright nucleus (see fig. 2.5).

There are two subclasses of Seyfert galaxies based on the presence of the broadness of the permitted emission lines. The type I Seyferts are characterized by the presence of narrow lines superposed to the broad permitted lines and the type II Seyferts have only the narrow lines present in the spectra.



Figure 2.5: Circinus Galaxy, an example of Seyfert type II galaxy observed by the telescope Hubble. Credits: [2]

2.3.2 Quasi-Stellar Objects

Quasars or Quasi-Stellar Objects (see fig. 2.6) are characterized by their large UV flux, as well as strong and broad emission lines. Their nuclear luminosity can be more than a thousand times the galaxies luminosity, outshining they host galaxy and appearing as a bright point source on optical images, hence the designation as "quasi-stellar".

The spectrum of quasars differs from the Seyferts through the stellar absorption features, which are very weak in quasars. Also, QSOs have weaker narrow lines when compared with the broad lines, in relation to the Seyfert galaxies.



Figure 2.6: Image of the quasar 3c273 taken from Sloan Sky Digital Survey (<http://classic.sdss.org/iotw/archive.html>)

Quasars emit at mostly all wavelengths, from the radio to the X-ray. In general, the continuum spectrum of a quasar can be described as a power law: $F_\nu = C\nu^{-\gamma}$ where γ is the spectral index, C is a constant and F_ν is the flux at that frequency interval. For $\gamma = 0$ the spectrum is flat, whereas for $\gamma = 1$ the spectrum has the same energy emitted in every logarithmic frequency interval.

2.3.3 Radio Quiet and Radio Loud/Jetted and Non-Jetted AGN

The concept of Radio loudness is based on the ratio of the radio flux (5GHz) to the optical flux (B-band) of the source $\frac{F_5}{F_B} \geq 10$. Sometimes it is also related with the host galaxy and with the SMBH spin. The table below 2.7 shows the classification of the sources according with their radio loudness and optical properties:

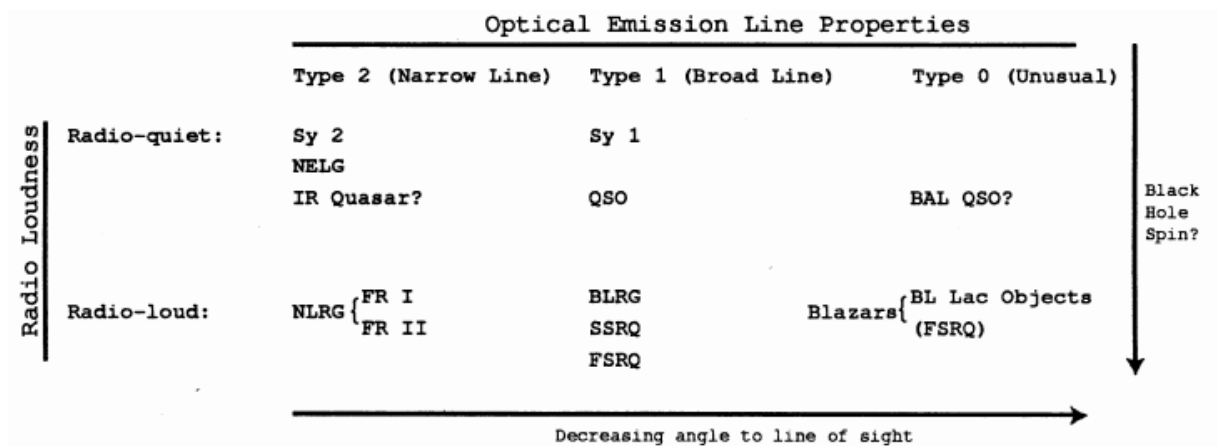
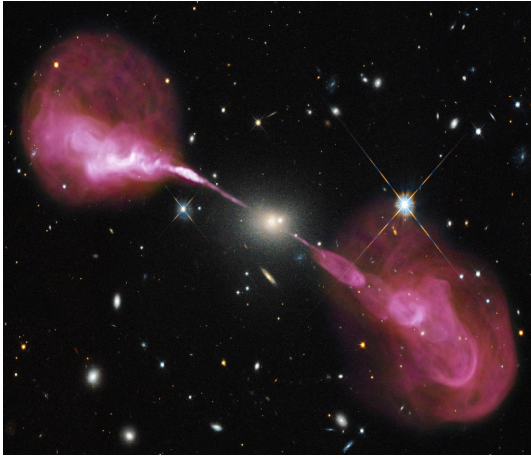


Figure 2.7: Classification of AGN according with the radio and optical properties. Addapted from: [45]

Almost 90% of the AGNs are radio quiet(RQ) 2.8(b) with spectra dominated by the thermal emission from the accretion disk. The radio loud (RL) 2.8(a) sources are a completely different class of AGNs with spectra mostly dominated by non-thermal emission coming mainly from the jet, and this is the most important difference between the two classes: the presence of the jet. In 2017, Padovani [39] suggested that the distinction between the sources should be done on the basis of jetted and non-jetted, instead of Radio Loud and Radio Quiet.

There are three principal characteristics to distinguish between the two classes. The first one is the direct evidence of the jet, that can be asserted very easily for bright radio sources where the jet is resolved. The second one is to look for other strong characteristics that only jets can reach, such as the emission in $\gamma - ray (\geq 1 MeV)$. Thirdly one should consider the correlation of radio-excess and the far-infrared (FIR) emission, since both FIR and radio emission are strongly correlated in non-jetted AGNs.



(a) Image of the radio loud AGN 3C348. Credits: NASA/ESA/S. Baum and C. O’Dea (RIT)/R. Perley and W. Cotton (NRAO/AUI/NSF)/Hubble Heritage Team (STScI/AURA)



(b) Image of the Radio quiet AGN Messier 77. Credits: Hubble Telescope <https://www.spacetelescope.org/news/heic1305>

2.3.4 Radio Galaxies

Radio galaxies were the first extragalactic objects discovered in optical images. Mostly, radio galaxies are elliptical galaxies with some activity in the nucleus.

The morphology of radio galaxies can often be described in terms of extended and compact sources. The extended sources are spatially resolved and usually have two regions of radio emission, one in each side symmetrically from the core, that can be extended to megaparsecs (Mpc). The extended sources can be divided into two classes: The Fanaroff-Riley Type I (FRI) are generally weaker radio sources, characterized by a bright core and decreasing luminosity outwards. Their typical luminosity is $L_{\nu}(1.4\text{GHz}) \leq 10^{32} \text{erg s}^{-1} \text{Hz}^{-1}$ [44]. The Fanaroff-Riley Type II (FRII) galaxies are more luminous than the FRI and are characterized by increasing brightness away from the core. Usually their luminosity is $L_{\nu}(1.4\text{GHz}) \geq 10^{32} \text{erg s}^{-1} \text{Hz}^{-1}$. The FRII galaxies also are characterized by the presence of strong jets, transporting energy from the core to the radio luminous regions (radio lobes).

The compact radio sources usually have the size $\sim 0.01 pc$ and sometimes are not resolvable even with interferometric methods. The spectra of these sources are often flat, with $\gamma \leq 0.5$, extended for several orders of magnitude in frequency. This characteristic is normally attributed to the presence of small unresolved sources or some inhomogeneity of the source.

2.3.5 LINERs

Low ionization nuclear emission-line region (LINER) galaxies (fig. 2.9) are a very low luminosity class of AGNs discovered in 1980 by Heckman [28]. They represent almost 50 % of the detected spiral galaxies [41]. They look like Seyfert II galaxies spectroscopically, only that their low-ionization lines of [OI] and [NII] are stronger.

In 1981, Baldwin, Phillips and Terlevich [18] showed that objects with similar emission lines could be distinguished through the ratio of the intensity of two pairs of lines. Hence we can distinguish the LINERs from the Seyfert II by their low value of $[\text{OIII}]/\text{H}\beta$ compared with $[\text{NII}]/\text{H}\alpha$.



Figure 2.8: LINER galaxy NGC4102. Credits: ESA/Hubble, NASA and S. Smartt (Queen's University Belfast)

2.3.6 Blazars

Blazars are radio sources with very variable radiation in time-scales from minutes to years. There are two types of blazars: BL Lacertae sources (BL Lac) and Flat Spectrum Radio Quasars (FSRQs). The main difference between the two classes is in their emission lines, which are strong and quasar-like for the FSRQs and weak or even absent for BL Lacs [37]. Another difference founded in these objects is that the FSRQs sources are generally discovered in redshift higher than 2, while BL Lac objects are usually much closer, with the redshift ≥ 0.6 .

Without the BL Lac emission lines it is extremely difficult to determine the redshift of these objects. Sometimes there is a presence of some absorption lines which are believed to come from the host galaxy, and they are used to derive the redshift of the BL Lac. In epochs of very low luminosity it is possible to observe some emission lines, this makes the BL Lacs appear as Optically Violently Variables (OVV). The OVVs are characterized by their short-timescales variability in optical, of the order of ≥ 0.1 magnitude in less than one day.

2.4 Pancromatic Jets

Jets are responsible for producing the most part of the non-thermal radiation that we observe from AGNs, especially in blazars. To characterized this radiation, first it is important to understand the mechanisms that produce it. For this reason, below we will briefly present

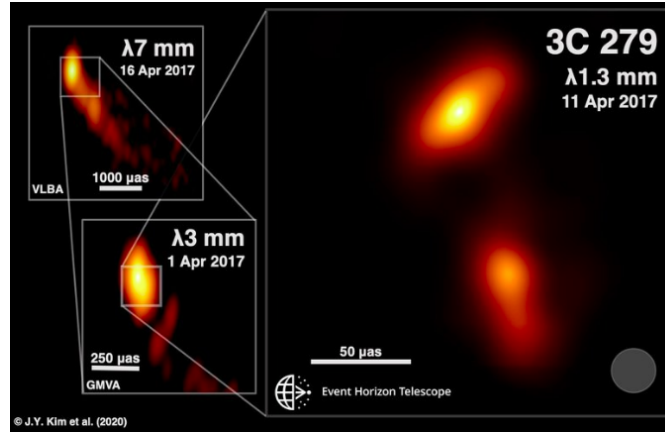


Figure 2.9: First image of a black hole powered jet from the blazar 3C279 using the Event Horizon telescope(EHT). Credits:J.Y. Kim (MPIfR), Boston University Blazar program, and the EHT Collaboration.)

two of the most important radiation processes that happens in jets. Then we will briefly discuss the acceleration mechanism that happens due the shocks waves internally in the jets to then, finally, present some observational properties of the jets in different wavelengths.

2.4.1 Synchrotron Radiation

Electrons and other charged particles in a magnetic field move along a helical path (see fig. 2.10. Consequently they are continuously accelerated by the Lorentz force. Since accelerated charges emit electromagnetic radiation, this motion of the charges lead to the emission of the so-called synchrotron radiation.

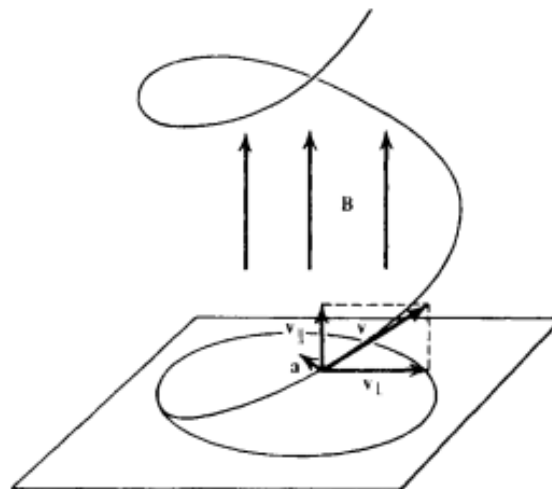


Figure 2.10: Motion of a charged particle in the presence of magnetic field. Credits: [43]

For an electron of mass m_e , momentum \mathbf{p} and charge e , the power of the emitted

radiation is given by:

$$P = \frac{2}{3} \frac{e^2}{m_e^2 c^3} \dot{\mathbf{p}}^2 \quad (2.13)$$

The equation above is the Larmor formula for an accelerated electron in the classical limit, and the radiation frequency is given by the Larmor frequency:

$$\nu = \frac{e\mathbf{B}}{2m_e c} \quad (2.14)$$

The Larmor equation can also be derived for relativistic charges, which is the case of the charged particles in the astrophysical jets. To do this it is necessary to derive the power equation above with respect to the proper time ($d\tau = \gamma dt$, where γ is the Lorentz factor given by: $\gamma = (\sqrt{1 - (v/c)^2})^{-1}$) and replace the momentum derivative $\dot{\mathbf{p}}^2$ by the squared quadrimomentum ($\mathbf{p}'^2 - (1/c^2)E'^2$) which is invariant in relation to other observers. Then the Larmor formula of the radiation for the relativistic charged particles is [19]:

$$P = \frac{2}{3} \frac{e^2}{m_e^2 c^3} \left(\frac{E}{mc^2} \right)^2 \left[\mathbf{p}'^2 - \frac{1}{c^2} \dot{E}^2 \right] \quad (2.15)$$

Considering that the electron is moving in an uniform field, it will move around the magnetic field line in a circular path, then the total intensity of the radiation can be integrated over all solid angles and is given by:

$$P = \frac{2}{3} \omega_B \frac{e^2}{r} \beta^3 \left(\frac{E}{m_e c^2} \right)^4 \quad (2.16)$$

Where $\beta = v/c, B_{\perp} = B \sin \theta$ and θ is the angle between the direction of the charge velocity and the direction of the magnetic field. $r = \gamma m_e c v / e B_{\perp}$ is the Larmor radius of the motion and $\omega_B = e B_{\perp} / \gamma m_e c$ is the Larmor frequency.

As a consequence of the dependence of the electric field with the angle θ , the spectrum of the synchrotron radiation will suffer some aberration. Effects of beaming in the emitted radiation will be concentrated in a narrow direction around the velocity of the particle. The observer will then see a confined pulse of radiation during a time interval smaller than the gyration period of the particle (see fig. 2.11). With this, the spectrum of the synchrotron radiation will be spread over a broader region than, the spectrum of a pulse of radiation generate during a time interval of the order of the gyration period of the particle $\omega_B / 2\pi$ [43].

The figure 2.11 shows that, for individual particles, the observer sees the pulse of radiation in the points where the cone of emission includes the direction of observation (line-of-sight), represented in the fig. 2.11 by the interval between points 1 and 2.

Before we move on, another important point to notice in the synchrotron radiation is its polarization. For an individual particle, the radiation is elliptically polarized. However,

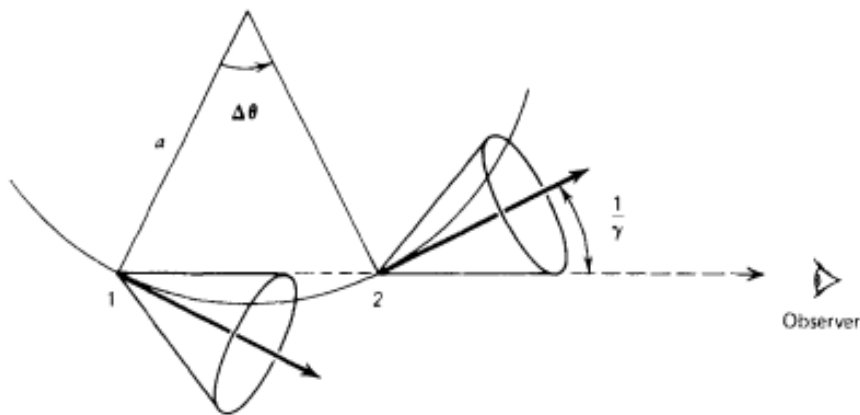


Figure 2.11: Cones of radiation emission at some points of trajectory of the accelerated particle. Credits: [43]

for a distribution of particles, the polarization varies smoothly with the pitch angle θ . In this case, the emission cone contributes equally for both sides of the line of sight, so the elliptical component of the radiation cancels out, with only the radiation linearly polarized remaining. Therefore, the synchrotron radiation can be characterized by its power per unit frequency in the parallel and perpendicular directions to the projection of the magnetic field in the sky, as exhibit in the fig. 2.12, which allow to characterise the state of the magnetic field of the emitting region through polarisation-sensitive measurements, conducted usually in radio and optical.

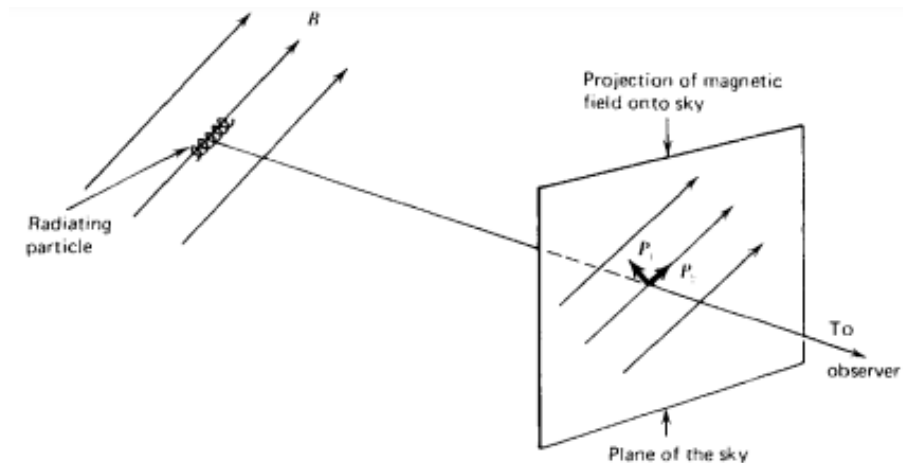


Figure 2.12: Vectors of the Synchrotron radiation projected in the plane of the sky. Credits: [43]

2.4.2 Inverse Compton

In regions of some density of photons and charged particles with moderate magnetic field, the high energy particles will transfer momentum to the photons and boost them up to the highest energies. This phenomenon is called the inverse-Compton scattering 2.13.

The scattered radiation can be described in terms of the ratio between the amount of energy radiated by the scattering system in a certain direction and the energy flux density of the incident radiation. The total scattering cross-section is given by [19]:

$$d\sigma = \frac{\langle dS \rangle}{\mathbf{S}} \quad (2.17)$$

Where \mathbf{S} is the Poynting flux of the incident ray and $\langle dS \rangle$ is the average energy radiated per solid angle.

Considering now the non-relativistic case, where the dipole radiation is given by $dS = (e^4/4\pi m^2 c^3)(\mathbf{E} \times \mathbf{n})^2 d\Omega$ and the Poynting vector $\mathbf{S} = c/4\pi E^2 \mathbf{n}$, we obtain:

$$d\sigma_T = \left(\frac{e^2}{mc^2} \right)^2 \sin^2 \theta d\Omega = r^2 \sin^2 \theta d\Omega \quad (2.18)$$

The formula above is called the Thompson's scattering formula. Where θ is the angle between the incident and scattered direction, r is the gyroradius of the electron, $d\Omega = \sin\theta d\theta d\phi$, and ϕ is the angle around the polar axis.

In the relativistic case, collisions will be effectively head-on due the solid angle aberration. From this we have that the energy of the photon in the center of the momentum frame is $h\nu \approx \gamma h\nu'(1 - \cos\theta')$, this implies a boost of $\gamma^2 h\nu$ in the energy of the electron for the inverse Compton scattering. From this we can see that very high energy photons are created by very energetic electrons as a result of the process. This is how the gamma-rays are thought to be created in the jets of Blazars and escape the opacity constraints from the dense radiation fields internal to the jets.

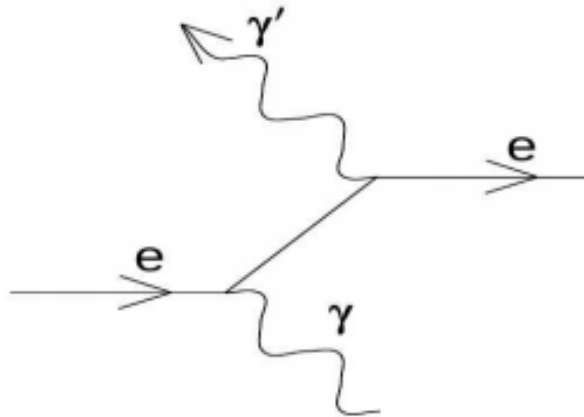


Figure 2.13: Faraday Diagram representing the inverse Compton scattering. Credits: [19]

The spectrum of one single particle of the inverse Compton emission can be derived considering a region with electron energy density $\epsilon_0 = \gamma mc^2$. The flux of the energy radiated

is $(cdtdn/d\Omega)\delta(\epsilon - \epsilon_0)$. In the momentum frame, the scattering cross section is given by:

$$d\sigma = \frac{1}{2}r^2(1 + \cos^2\theta')\delta(\epsilon - \epsilon_0)d\epsilon d\Omega' \quad (2.19)$$

The equation above can be used to derive the energy distribution of the scattered photons in the observer frame. This was firstly done in 1970 by Blumenthal and Gould and the result is [19]:

$$\frac{dN_{\gamma,\epsilon}}{dt d\hat{\epsilon}} = 8\pi r^2 cn(\epsilon) d\epsilon f(\hat{\epsilon}) \quad (2.20)$$

where ϵ is the energy of the incident photon, ϵ' is the energy of the scattered photon, γ is the Lorentz factor of the electron, $\hat{\epsilon} = \epsilon'/4\epsilon\gamma^2$ is the energy scattered in terms of its maximum value and lastly $f(\hat{\epsilon}) = 2\hat{\epsilon} \ln \hat{\epsilon} + \hat{\epsilon} + 1 - 2\hat{\epsilon}^2$ is a broad distribution of energy. This distribution has its maximum at low energies of the scattered electrons $\epsilon'_{max} = 4\epsilon\gamma^2$ and this maximum corresponds to the head-on transfer of energy from the electron to the photon.

2.4.3 Shock particle acceleration

There are two important features that give us the confidence that are shock waves in the jets that accelerate particles to relativistic energies to create the observed synchrotron and inverse-Compton spectra. The first one are the inhomogeneities founded in the radio and x-ray images of the extragalactic jets. Some of these inhomogeneities are also known as knots, which are localised pieces of high intensity emission along the jet, where energy dissipation in form of radiation is mostly happening.

Below we show an early optical image of the galaxy M87 took by the Nordic Optical Telescope at La Palma, Canarian Islands, Spain [9]. In this picture it is possible to clearly identify the presence of the knots as the point-like structures in the right.

In 1978 M.J Rees identify these knots in M87 and noticed that they happen due some irregularities in the velocity flux, to which follows an increase in emissivity of the plasma. As an example, if the flow speed v_j changes on a timescale Δt by a factor $\Delta v_j/v_j \gtrsim M_j^{-1}\Gamma_j^{-2}$, where M_j is the flow Mach number and Γ_j is the bulk Lorentz factor, then the faster material will reach the slower flow ahead in the time $\sim v_j\Delta t/\Delta v_j$. This will create a shock wave that propagates with speed v_j , compressing the magnetic field lines along the direction of motion and accelerating particles by transfer of the bulk motion into microscopic velocity of the particles. These re-accelerated particles will in turn emit more intensively in interacting with the magnetised plasma downstream of the shocks, generating the enhanced brightness areas identified as the knots in the images.

Particle re-acceleration such as described above is the second important evidence in support of the existence of shock waves in the jets. In fact, jets generally have a size of the order of Mpc, whereas the lifetime of one electron emitting synchrotron radiation in a strong magnetic field is about 10^5 years, much inferior to the time the plasma need to cross

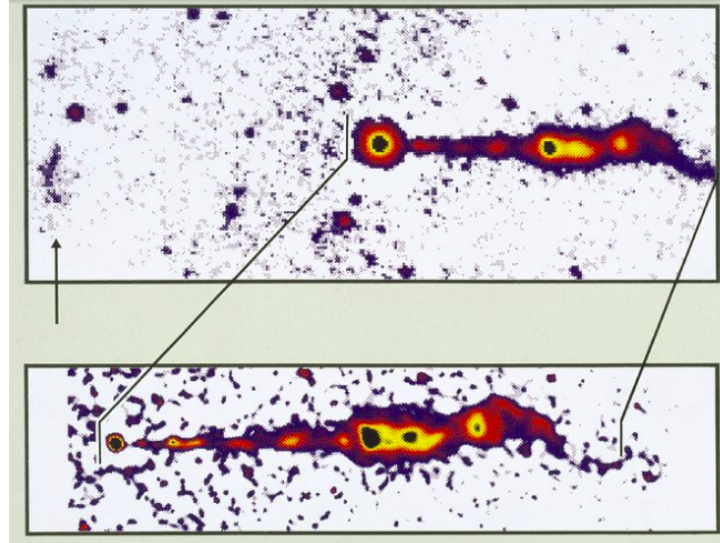


Figure 2.14: First optical image of the jet of the galaxy M87 the image is a superposition of three CCD images in yellow, red and near-infrared (V, R and I). Credits:ESO

the jet. In this perspective, there is no time for the electron to get out of the AGN and arrive at the extremities of the jet without the presence of the shock waves reprocessing and re-accelerating the particle population.

2.4.4 Optical Jets

The first observations of jets were made in the optical waveband for the galaxies M87 and 3C373. In these observations they noticed that the jets were linear structures pointing radially away from the center of the galaxy.

Generally the optical jets are narrower, shorter, more structured than the radio jets and never have been identified in the counter-side of the galaxy, even when radio observations shows a presence of second jet (see for example [42],[44]). One of the remarkable features of the jet, the superluminal motion, was identified in an optical jet by the telescope Hubble during a period of observation of ~ 4 years(see fig. 2.15).

Besides the structure of the optical jet being slight different to that of the radio jets, the position of the knots along the structure of both wavelengths agree very well. This is an indicative that the radiation process happening in the optical jets is also synchrotron radiation from the same particle populations. The relativistic electrons producing synchrotron radiation lose their energy via emission of radiation faster than the lower-energy particles emitting at peak frequency in radio. Since the cooling time for electrons emitting synchrotron radiation at optical wavelengths are in the order of $\sim 10^3(B/10^{-4}G)yr$, they cannot travel more than $\sim 1Kpc$ of distance without losing their energy. Therefore, since the observed size of the optical jets is much bigger than that, it is implied that these emitting electrons cannot be originated in the disk itself, as we already noted before. Instead they must be

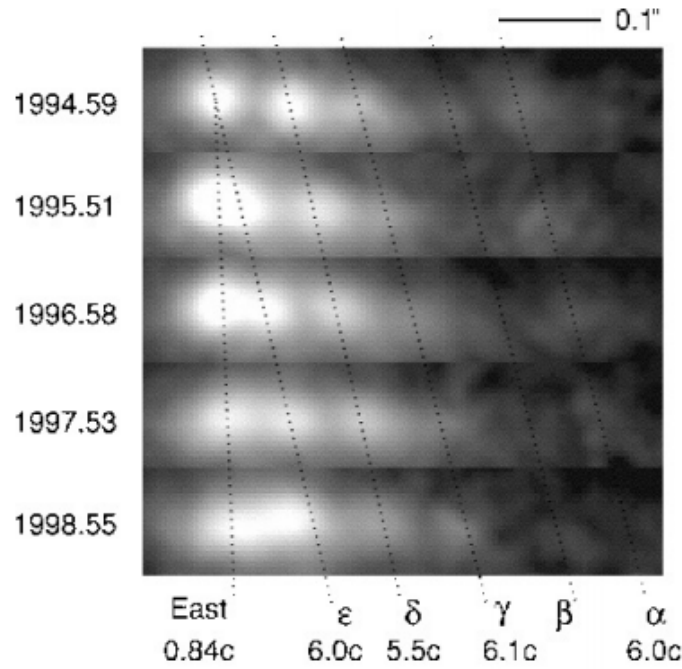


Figure 2.15: Optical jet of M87, images taken by the HST over a period of four years. The angular velocity of the components is about ~ 23 mas/yr. Assuming that M87 is at distance of $D = 16Mpc$, the components velocities can reach $\sim 6c$. Adapted from:[44]

produced locally in the jet.

The spectrum of the optical jets commonly follows a power law $F_\nu \propto \nu^\alpha$, with the index α representing in general a slightly steeper spectrum than the radio one.

2.4.5 X-Ray Jets

The Chandra satellite identified many jets emitting also in X-rays [44]. Approximately 50% of the flat-spectrum radio quasars with radio jets also appear in the x-ray images.[44] Besides the corresponding radio image often shows the presence of opposite jets, they were never identified in the X-rays, confirming the beaming effect in the X-ray band.

The energetic electrons present in the jet which are responsible for the production of the radio emission can also generate *x-ray* emission by inverse Compton scattering. The correlation of the spatial distribution among the radio, optical and x-ray emission suggests that they also can be originated in the same region of the jet via synchrotron emission. The Lorentz factor of the electrons generating synchrotron radiation may reach values of $\gamma \sim 10^4$ [44]. Such electrons can scatter the radio photons into x-rays by inverse Compton scattering, generating an effect called synchrotron self-Compton radiation.

Another possible source of radiation for the inverse Compton effect can come from the photons of the Cosmic Microwave background (CMB). The relativistic electrons can scatter the photons of CBM producing X-rays. In fact, in most cases, the detected X-rays come

from the Compton-scattering of CMB radiation [44].

The inverse-Compton scattering is not the only way to produce x-rays in the jets. In some sources as FRI for example, the responsible for the x-ray emission is the synchrotron radiation. This is evidenced by the X-ray variability observed in the knots of some galaxies, like M87 for example. The cooling times of the electrons here are much smaller due to the larger Lorentz factor (γ), associated to the direct synchrotron emission, as opposed to the timescales associated to the inverse Compton scattering. The short cooling time-scales mostly in the FRI radio sources implies also a necessity for a local acceleration of the electrons. On the other hand the required energies for the electrons are $\sim 100 TeV$ which is very high for an electron emitting synchrotron. This fact turns unclear which acceleration processes may be responsible for these very high energies [44].

2.4.6 Gamma-ray Jets

The Very High energy radiation emitted from blazars originates in the jet. Currently there are two broad classes of models thought to explain the production of γ -ray inside the jets. These models are hadronic, when the responsible particles for emission are protons, or leptonic, when the jet is composed by electrons and positrons. The validity of these models vary depending on the assumed composition of the jet.

2.4.6.1 Hadronic Models

The hadronic models generally are disfavored in relation to leptonic models due the fact that they required particles accelerated to energies up to $10^{20} eV$ to be capable of explaining the observed blazars fluxes, which is challenging for any theoretical model currently available [16].

In a hadronic process, an electromagnetic pair-cascade can develop inside the jet producing γ -rays if a significant fraction of the kinetic power in the jet is converted into acceleration of the protons, and if those protons reach the threshold for p- γ pion production. For a photo-pion cross-section of about $\simeq 10^{-28} cm^{-2}$ this threshold is in the order of $\simeq 0.03 E_{19}^{-1}$. Electromagnetic cascades can give rise to γ -rays from: π^0 -decay into 2γ and π^\pm -decay ($\mu^\pm \rightarrow e^\pm$) [21]. These reactions require, for the protons be accelerated to the ultra-relativistic energies ($10^{19} eV$), a high magnetic fields of the order of tens of Gauss. The differentiation between the reaction channels can be made based on the fact that pion-cascades (π^0 and π^\pm) generate featureless γ -ray spectra, while p-synchrotron cascades produces a double-bumped γ -ray spectra.

2.4.6.2 Leptonic Models

The leptonic model is generally preferred instead of the hadronic model due to three main reasons. First, in the leptonic model, the shock acceleration can more easily explain

the energies of the electrons which produce the VHE γ -rays. Second, the density of the particles and the magnetic field in the jet, added to the boosting and radiation-enhancement mechanisms, easily give rise to conditions favouring synchrotron and inverse Compton processes to develop, which are necessary to explain the observations. In fact, their cooling times are comparable to the dynamic time of the sources, inferred from the light-crossing times ($R/c \lesssim \text{hour}$), and this implies a very efficient radiation mechanism. Lastly, the correlated character of the blazar SED emission, with its double bump structure, is very well fitted within the leptonic emission model predictions.

In the leptonic models, the Synchrotron-self Compton(SSC) mechanism arises as a tendency to explain the origin of the target photons for the inverse Compton scattering. In this mechanism, the soft photons are provided by the synchrotron emission of the same particles responsible for the inverse Compton upscattering. This implies that in this model, the synchrotron emissivity depends linearly on the electron distribution, and the inverse Compton scattering depends quadratically. Therefore, if an increase in the source luminosity is registered due to injection of electrons, the inverse Compton bump variability will be bigger by a factor N_e than the one of the synchrotron. Thus, a Compton dominance of the source is seen if the injection of energetic particles is very large. Opposite to that, an increase of the magnetic field will decrease the ratio ($Luminosity_{Compton}/Luminosity_{Synchrotron}$), shifting the peak of the two distributions by equal amounts towards higher energies.

In conclusion, one could think that the high-energy emission from the jets are completely correlated with the its density and particle composition. Distinguish all these spectral characteristics is very important to classify the type of AGN and its radiation mechanisms.

2.5 Blazars

As mentioned, blazars are radio-loud AGNs with their relativistic jets pointing towards us, being therefore mostly characterised by a dominant non-thermal emission. The spectral energy distribution (SED) of blazars is often seen extending from the radio up to TeV γ -ray bands, and presenting two broad components in the νF_ν plane (see fig. 2.16).

The position of the SED peaks are variable, depending on the state of the source, and generally are accompanied by short-timescale variability in the flux level [19]. Thus, blazars are subdivided in categories forming a multi-band continuum according with their spectral properties, which form a presumed "blazar sequence".

2.5.1 Blazar Sequence

Due to the variation of its bimodal SED, blazars are classified in a range varying from low-frequency-peaked (or radio selected) BL Lacs (LBLs), which are more bolometrically luminous and whose synchrotron peak lies in the optical bands, to high-frequency-peaked (or

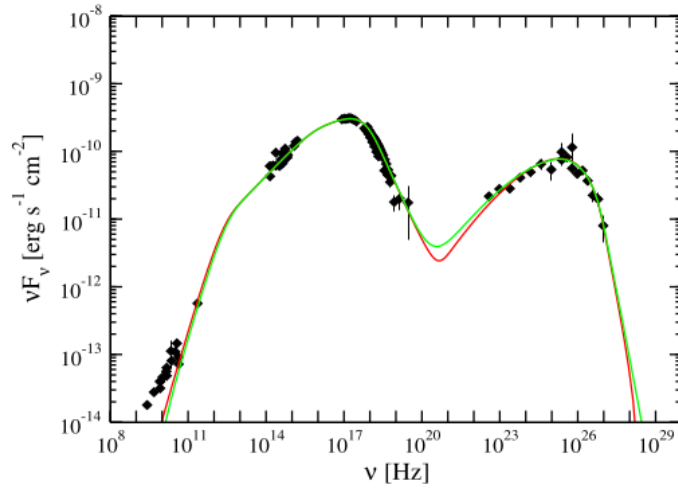


Figure 2.16: SED of the blazar Mrk 421 measured with Fermi and MAGIC telescopes. Adapted from: [23]

x-ray selected) BL Lacs (HBLs), with synchrotron peak emission situated in the keV range. There is also a third class of intermediate-frequency-peaked BL Lac (IBLs), intermediate between LBL and HBL. This spectral sequence reflects in an anti-correlation between the synchrotron peak of the emission and the corresponding energy density at this frequency. This phenomenology has traditionally been explained in terms of synchrotron-self-Compton and external-Compton models. In the external Compton model, the origin of the seed soft photons are the radiation fields external to the emitting zone (see [19] for details). In both models mentioned, the SED sequence indicates an evolution of the physical properties of the emission region, namely the jet power and the intensity of the diffuse radiation field surrounding it, and which serves as target photons for the inverse Compton scattering.

The main idea behind the Blazar sequence (see. fig 2.17) is that X-ray luminosity can be used to trace the density of seed photons and strong radio fluxes indicates the power in the jets.

The nature of the second SED component, which extends until the γ -ray band is still under debate. Through the observed luminosity and the frequency of emitted photons of blazars it is possible to see that they are physically enhanced by beaming with δ^4 , where $\delta \equiv [\Gamma(1 - \beta \cos \theta)]^{-1}$ is the bulk Doppler factor of a flow for a jet viewing angle θ [19]. One could think that this suggests a correlation between both factors, however the evidences found in blazars show exactly the opposite. The blazar sequence in the leptonic scenario is demarcated by a decrease in energy of the electrons emitting at the peaks of the SED at the same time that the energy density of the seed photons for inverse Compton scattering and the source power increases.

Today through the gamma-ray observations this simplified view of the Blazar sequence is being challenged. Studies with the brightest blazars detected with Fermi indicates

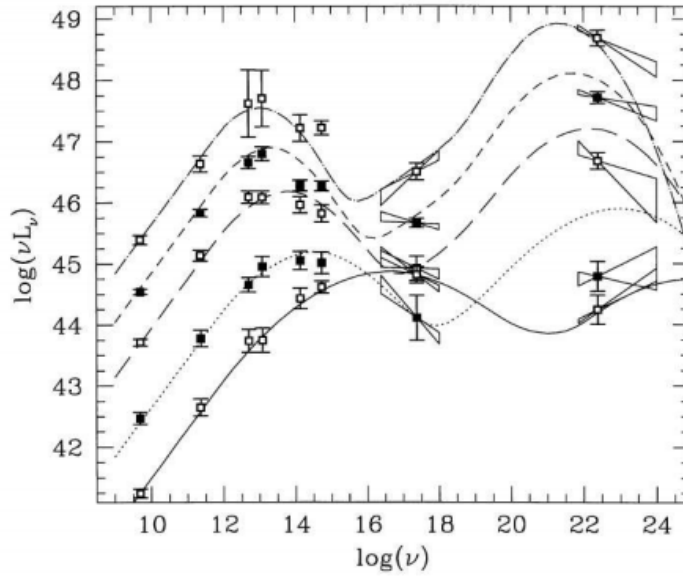


Figure 2.17: Blazar sequence. Where the fitted curves are analytic curves that were obtained assuming first that the ratio of synchrotron to Inverse Compton peak frequencies is constant and second that the amplitude of the inverse-Compton peak is proportional to the radio luminosity. Adapted from: [19]

a good correlation between the jet power and the accretion disk, suggesting an important correlation link between these two processes [19].

2.5.2 Gamma-ray Blazars

Blazars dominate the γ -ray sky. To observe these sources at these very high energetic bands is very important to understand the acceleration process that happens at these extreme environments.

Currently there are two operational γ -ray space telescopes: the “Astro-Rivelatore Gamma a Immagini LEggero” (AGILE), launched in 2007 and the Fermi Gamma-Ray Space Telescope, launched in 2008. The largest catalogue of γ -ray sources made so far is the 3FGL, including 3033 objects, with the majority of them being blazars. Altogether, there are 415 FSRQs (all LSP), 657 BL Lacs (mostly of the HSP type), and 402 blazars of uncertain type (which are assumed to be blazars due to their radio to γ -ray SED, but there is not yet an observation of these objects in optical to classify them firmly as FSRQ or BL Lac) [40].

An interesting aspect about the LAT objects is that they form a complementary sample to the TeV sources, because the GeV blazars tend to be weaker TeV emitters, what makes them belong to the radio-optical sample rather than the X-ray selected blazars. The anticorrelation between the GeV-TeV bands is associated with the high density of soft IR/optical photons in quasars, providing an effective environment for the production of gamma-rays through Inverse Compton scattering, but also the maximum energy limit of the scattered ra-

diation, a characteristic that can be observed in the “redder as brighter” relation exposed in Figure 2.17.

Finally, GeV blazars also tend to have superluminal jets, which differ from the subluminal propagation seen in the radio maps of TeV objects, most probably due to jet deceleration [19]. Apart from that, the intergalactic absorption of TeV γ -rays from distant sources generate different spectral properties in both populations of blazars.

The observational properties of blazars in gamma-rays are being increasingly probed with the development of new technologies and the detection of new sources. There is a very interesting recent study which shows a detection of a possible correlation between the black hole mass and the gamma-ray emission, suggesting a possibility of existence of a threshold black hole mass for the start of strong jet activity, both in gamma-rays and radio [46].

Given the relatively limited sensitivity of ground-based telescopes, the most of the analyses made with TeV blazars are done when these sources are in a high-state (flaring) and this imposes an intrinsic bias in the studies which prevent more accuracy on the determination of the physics of the blazar jets. With the improved sensibility of the future telescope CTA, it is expected that more sources will be detect, also in the quiet state, and this will help understand the process behind these sources.

2.5.3 Propagation of gamma-rays through the Extragalactic Background Light

The extragalactic background light (EBL) is a broad-band radiation in which the local universe is immersed. This radiation is composed by the Infra-red component from the integrated and redshifted starlight (1-5 μm) as well as the reprocessed radiation by dust (100-200 μm). Moreover the EBL acts by suppressing the VHE flux in the γ -ray spectrum of extragalactic sources.

The main mechanism by which gamma-rays are absorbed by the EBL is the photon-photon pair production, where the incident gamma-ray interacts with a softer photon and produces an electron-positron pair: $\gamma_1 + \gamma_2 \rightarrow e^- + e^+$. The energy threshold of this interaction is: $E_{\gamma,TeV} = 0.26/E_{TeV}$. Due the fact that the incident gamma-ray carries most of the momentum before the reaction, the electron-positron pair created is beamed in the direction of motion of the gamma-ray, generating a cascade of gamma-pair in space.

The expected peak of the EBL in the source spectra appears in the near-IR ($\sim 1 \mu\text{m}$), indicating for example that the 1 TeV photons will be more attenuated than softer 0.2 TeV photons. Therefore, the spectrum of distant blazars will be steepened proportionally to the redshift of the source. Lastly, it is important to mention that the most important characteristic of the EBL is the limitation that she causes in the observation of distant sources likewise the constraints in the extension of the observations to the very high energies

2.6 Blazar Variability

Blazars are often detected in the gamma-ray band when they are in a high state due to the sensitivity of the current IACTs which are not capable to generally detect these objects in a quiescent phase. When blazars are in these high states they are evidenced by strong and burst-like flaring episodes which are characterized by very short and non-periodic variability events, due to the fast cooling times of the VHE-emitting electrons ($\sim 10\text{TeV}$).

The fast variability mostly encountered in the VHE emission of blazars, as the superburst of PKS 2155-304 in 2006 [20], is an indication that their emission region is extremely compact, which either can be the compact region around the SMBH or substructures inside the jet [19].

The most accepted concept is that fast variability occurs when electrons are accelerated in small volumes (sub-regions) of the jet. The electrons with the highest-energy, radiating at high frequencies, lose most of its energy within a thin section close to the acceleration site. While electrons with lower energies radiate at the lower frequencies over a larger volume. However, the lower-frequency outburst starts at the same time as the high-frequency flare and declines first, while the larger emitting region fills with electrons.

The current IACTs are able to detect variability on the scales of minutes. Studying these transient events can define the physical constraints for their emission process. CTA will detect important temporal features like minimal variability times and putative periodicity of the burst-like events, which could provide some definite answers to the question of the size and possible location of the VHE emission region, and the physical emission mechanisms, such as particle acceleration and cooling time.

Chapter 3

Cherenkov Telescope Array

3.1 The Cherenkov Telescope Array

The field of very-high energy (VHE) ground-based gamma-ray astronomy effectively started in 1989 when the Fred Lawrence Whipple Observatory detected the first TeV emission signal from the Crab Nebula using the Imaging Atmospheric Cherenkov (IAC) technique. After that, the HEGRA observatory (High-Energy-Gamma-Ray Astronomy) began to function and achieved the most energetic detection at the time, measuring emission up to 16 TeV from the blazar Markarian 501 (Mrk 501). HEGRA stop functioning in 2002 and gave place to the third generation of IAC Telescopes, in particular the MAGIC (Major Atmospheric Gamma Imaging Cherenkov) Telescope, which started to functioning in 2004 at the same site of the Roque de Los Muchachos in La Palma, in the Canary Islands. Together with MAGIC, other two instruments formed the third generation of IACTs, namely VERITAS (Very Energetic Radiation Imaging Telescope Array System) in Arizona, in the United States and H.E.S.S. (High-Energy Stereoscopic System), in the Khomas Highlands, in Namibia, which started between 2004 and 2007.

Ground-based gamma-ray astronomy keeps growing with the development of new instruments, such as the construction of HAWC (High Altitude Water Cherenkov Observatory) in 2015, which uses a complementary technique to the IACTs and consists of on an array of 300 water Cherenkov detectors. Its main advantage is the capacity of operate 24 hours a day, while the IACTs can only operate during the night, and in moonless conditions. Conversely, HAWC, which is based on the water Cherenkov technique has a limited sensitivity and angular resolution.

The Cherenkov Telescope Array (CTA), designed to be the next-generation atmospheric Cherenkov observatory, will be the largest and most sensitive ground-based instrument built until today in very high energies. To cover the very ample energy range, CTA will be composed by three types of instruments – Large, Medium and Small-Sized Telescopes – spread in two sites, one in the Northern and another in the Southern hemisphere.

CTA will allow to answer some fundamental questions in physics, which can be grouped in three major themes [22]:

Theme 1: Understanding the Origin and Role of Relativistic Cosmic Particles

- What are the sites of high-energy particle acceleration in the universe?
- What are the mechanisms for cosmic particle acceleration?
- What role do accelerated particles play in feedback on star formation and galaxy evolution?

Theme 2: Probing Extreme Environments

- What are the characteristics of relativistic jets, winds and explosions?
- What physical processes are at work close to neutron stars and black holes?
- How intense are radiation fields and magnetic fields in cosmic voids, and how do these evolve over cosmic time?

Theme 3: Exploring Frontiers in Physics

- What are the nature of dark matter? How is it distributed?
- Are there quantum gravitational effects on photon propagation?
- Do axion-like particles exist?

Lastly, besides being designed for detection of gamma rays, CTA has a great potential for a wide range of astrophysics and astroparticle physics research based on observations of cosmic-rays.

3.2 Cherenkov Radiation

CTA will capture the Cherenkov light produced by high energy particles in the atmosphere. Discovered in 1934 by Pavel Cherenkov this homonymous kind of radiation is a secondary product of the primary cosmic-rays (or VHE gamma-rays) reaching the atmosphere. When the cosmic rays interact with the atoms in a material medium (e.g., atmosphere or water) they produce a cascade of secondary particles. Here we will focus on gamma rays reaching the atmosphere because this is what our experiment detects.

There are two process that happen at the moment when the gamma-ray reaches the atmosphere. First, they interact with the electric field of the air nuclei and produce a pair

$e^- e^+$. Since the rest mass of the electron ($0.5 \text{ MeV}/c^2$) is very tiny compared with the energy of the gamma-ray ($> 1 \text{ MeV}$), the rest of the energy is converted into kinetic energy of the electron. When the electron passes near a charged atom it loses kinetic energy (via Bremsstrahlung) and produces gamma radiation. The distance scale interaction between the gamma-ray and the nuclei is given by the radiation length X_0 , defined as the distance over which the secondary electrons will lose energy until $1/e$ of the initial kinetic energy of the electron with is equal to $7/9$ of the mean free path for pair creation.

This parameter also governs the altitude of the first interaction of the gamma-ray with the atmosphere, for the atmosphere X_0 is $\approx 37.1 \text{ g}/\text{cm}^2$ and for a gamma-ray photon of 100 GeV the altitude of the first interaction is $\approx 20 \text{ Km}$ above the sea level. Every time that the length X_0 is crossed, one of the two process takes place:

$$\begin{cases} \gamma \xrightarrow{\frac{7}{9}X_0} e^- + e^+ \\ e^- \xrightarrow{\frac{7}{9}X_0} e^- + \gamma \end{cases}$$

This generates a cascade that propagates through the atmosphere (see fig.3.1). The cascade stops when the energy of the charged particle is not enough to produce a new pair. Approximately 10% of the primary gamma ray's energy reaches an observation level of 5.2 km above seal level in the form of particles.

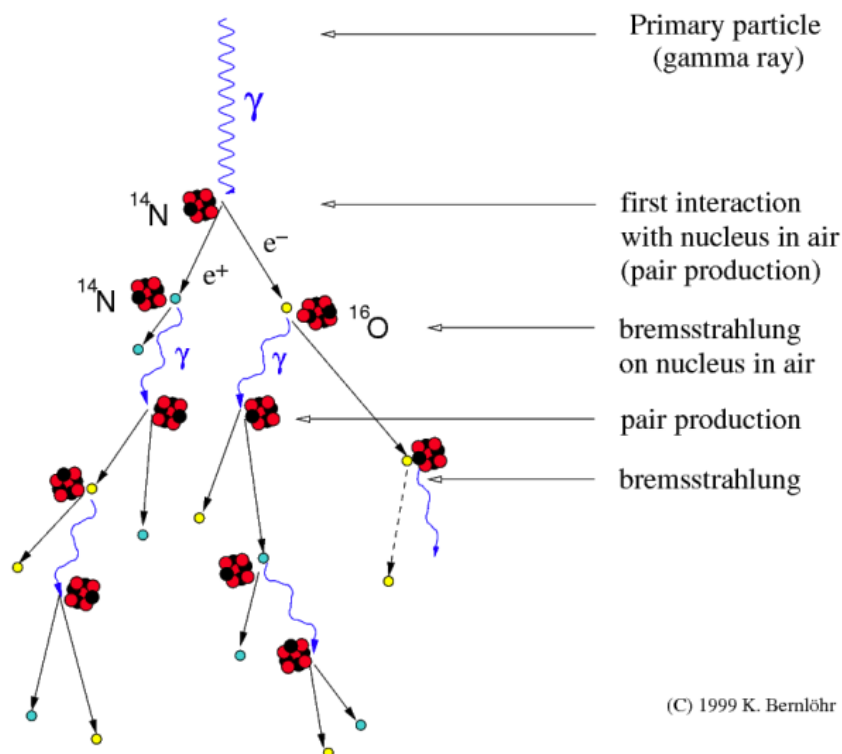


Figure 3.1: Development of gamma-ray air showers. [3]

The second process that happens as a result of gamma ray-induced cascade is polarization of the medium. When a charged particle travels through a transparent medium, like

the atmosphere, it polarizes the atoms in the neighborhood of the position of the particle trajectory. An electron travelling in the atmosphere with velocity lower than the phase velocity of the light has a symmetrical electromagnetic field around itself. Then, at long distance, there is no residual field and no radiation (see fig. 3.2(a)). If the electron is travelling with velocity bigger than the velocity of the light in the medium, (fig. 3.2(b)) the polarization will no longer be symmetrical around the axis in which the electron is moving, so there will be a resultant field and therefore radiation.

Each instantly polarized atom radiates an electromagnetic pulse at the moment of the depolarization. In general, the wavelets from all parts of the track interfere destructively, but when the electron is moving faster than light the wavelets interfere constructively, resulting in a remaining field at long distances, and therefore radiation that propagates away. This *Cherenkov radiation* will be emitted while the Lorentz factor of the particle is

$$\gamma > \gamma_0 = \frac{n(z)}{\sqrt{n(z)^2 - 1}}$$

where $n(z) = 1 + \eta(z)$ is a function dependent of the altitude z . This dependence establishes a threshold of energy below which no radiation is emitted by the medium. This threshold corresponds to an electron energy of $E_{min} = \gamma_0 m_e c^2 = 44 \text{ MeV}$ for an electron at 10 km above sea level. [19]

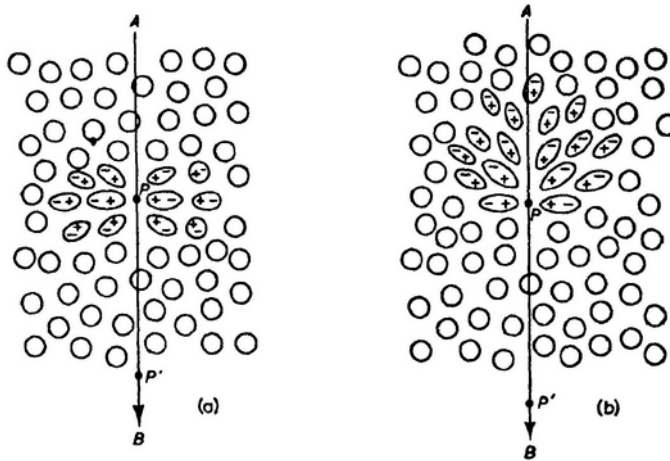


Figure 3.2: Polarization in a dielectric produced by a passage of a charged particle. (a) At low velocity (b) At high velocity. [31]

The Cherenkov radiation will be emitted in a cone of radiation with angle Θ_c around the trajectory of the particle, where:

$$\cos \Theta_c = \frac{1}{\beta n(z)}$$

In figure 3.3 is shown half of the Cherenkov cone formed by shock waves fronts that interferes constructively due the perturbations in the atmosphere.

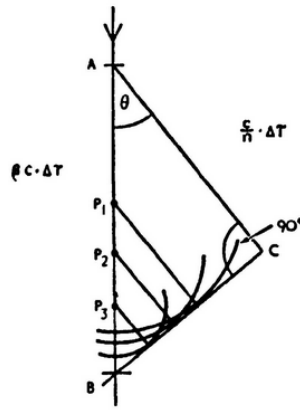


Figure 3.3: Huygens construction for Cherenkov front waves. Half Cherenkov Cone with angle $\Theta = \cos^{-1} \frac{1}{\beta n}$ for a particle traveling with $v > \frac{c}{n}$. Credits: [31]

The spectrum of Cherenkov light is peaked at short wavelengths (UV-blue), since the UV is absorbed over the atmosphere by ozone molecules, the radiation has a bluish characteristic and can easily be detected by optic experiments on the ground. Figure 3.4 shows the spectrum of the Cherenkov radiation in function of the wavelength for different energies of the primary gamma-ray. The Cherenkov spectrum is given by the Frank-Tamm relation: [19]

$$\frac{d^2 N}{dx d\lambda} = \frac{2\pi\alpha}{\lambda^2} \sin^2 \theta$$

which give us the differential number of Cherenkov photons emitted per unit path length dx in the wavelength interval $(\lambda, \lambda + d\lambda)$ at Cherenkov angle Θ_c and $\alpha = 1/137$ is the fine structure constant. Integrating the equation above for small angles ($\sin \Theta \approx \Theta$) over the peak emission of 280-640 nm and the area of the shower of $\approx 10^{4-5} m^2$, then multiplying by the total path length $\sim 10^5$ cm we arrive that the total number of Cherenkov photons detected on the ground is about 10^7 .

Another important characteristic of the Cherenkov showers to be considered is their duration. Due to the low refractive index of air the speed of the energetic particles and the speed of the emitted photons are almost the same, so that the non-absorbed photons arrive at the ground within a pulse of duration:

$$\Delta t = \frac{d}{c} \left(\frac{n-1}{n} \right)$$

where d is the total path length $\sim 10Km$ according to [19], c is the speed of light, and n for the air is $\simeq 1.0003$, which gives us the duration of ≈ 9 ns for the center of the shower. Since the shape of the pulse front along the light pool's extent is curved, in the borders the duration can get to $\sim 100ns$, due the Cherenkov emission from the particles away from the shower axis and the lateral spread, this factor is very important for the observation techniques.

The lateral distribution of the Cherenkov shower is given by multiple Coulomb scattering [17] with a quantity known as the Moliere radius R_{mol} (cm) which the physical signifi-

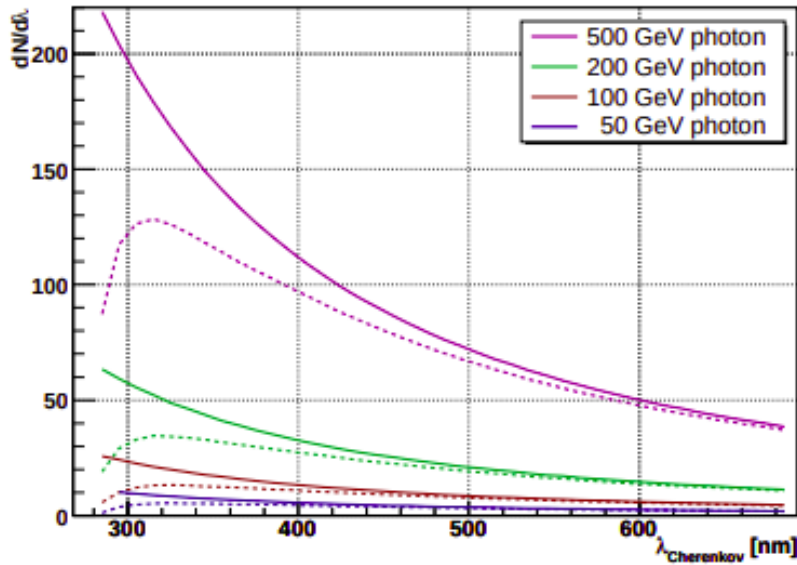


Figure 3.4: In the figure above the solid lines represents the spectra of the Cherenkov light for different energies at 10 km of altitude, and the dashed lines represents the correspondents spectra at 2200 m of altitude. The UV-blue part of the spectra is modified due the Rayleigh-scattering of the air molecules with ($d < \lambda$). The photons with wavelength $\propto (\lambda^{-(1-1.5)})$ suffer Mie scattering due the presence of aerosols and water droplets in the atmosphere, in addition, the light with $\lambda < 280nm$, is completely attenuated by absorption of ozone molecules presents in the atmosphere above 10 km of altitude, with introduces a cut-off of the spectrum. Credits:[47]

cance is that it is the radius of a cylinder containing almost 90% of all the secondary particles produced in the shower and is given by:

$$X_{mol} = X_0 \frac{E_s}{E_c}, \text{ and } R_{mol} = \frac{X_{mol}}{\rho}$$

where $E_s = 21MeV$, $R_{mol} \approx 80m$ at sea level and at the position of shower maximum (for a vertical 1 TeV shower) $R_{mol} \approx 200m$. The lateral spread can be described by the Cherenkov angle Θ , considering the refraction index $n = n_o \exp(-h/h_o)$ function of height, the light generated at a height (h) with angle $\Theta = \sqrt{2(n-1)}$ will propagate away from the region where most of particles concentrates. The distance(r) at which the photons reach the ground away from the axis is given by:

$$r = h \sqrt{(n-1) \exp(-h/h_o)}$$

where h_o is the height at which the emission is maximum. The figure 3.5 below illustrates the several distances hit with varying of the Cherenkov angle.

3.3 Imaging Atmospheric Cherenkov Telescopes

There are basically two classes of Atmospheric Cherenkov telescopes: Sampling Atmospheric Cherenkov Telescopes(SACT) and Imaging Atmospheric Cherenkov Telescopes

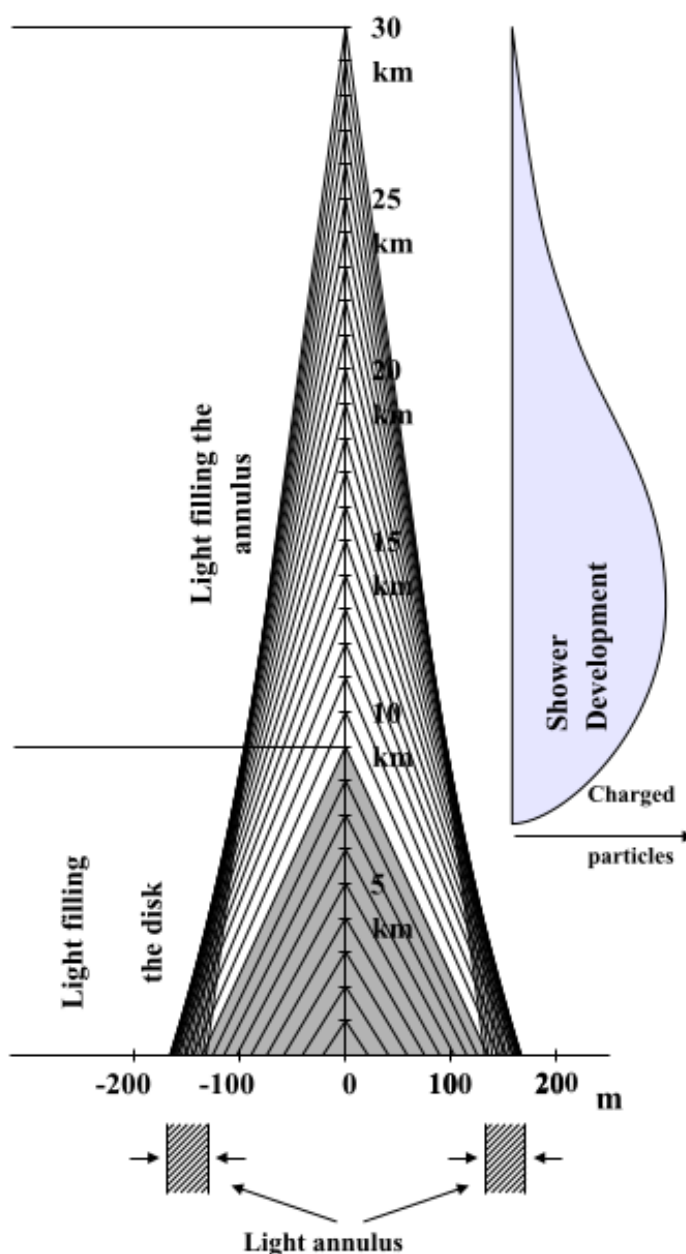


Figure 3.5: Cherenkov lateral radius of the light pool at the ground for different altitudes with related Cherenkov angles. Credits: Tibaldo L.[1]

(IACTs). The SACTs are made of a large array of mirrors covering a large fraction of the light pool of the gamma-ray shower on the ground that records the light intensity at each position along the ground. The IACTs are basically a wide-field optical telescope consisting of a large reflector with a high-speed photomultiplier camera in the focal plane. To detect the faint flashes of the Cherenkov light against the dark night sky background, short exposures and large reflectors are required. For a telescope the signal-to-noise ratio (S) is:

$$S \propto \left(\frac{A_m \epsilon}{\tau \Omega_{pix}} \right)$$

where A_m is the square root of the mirror area, ϵ is the reflectivity of the optics and quantum efficiency of the camera, τ is the square root of the signal-integration timescale and Ω_{pix} is the solid angle of the pixels.

To detect an event the minimum threshold necessary comes from the energy threshold (E_{th}) of the instrument, since (E_{th}) is inversely proportional to S , to minimize the threshold it is necessary to maximize the mirror area of the telescopes. To minimize the integration time, it is required high speed detectors and electronics, which ideally must be of the order of the shortest timescale of the Cherenkov light wave front (ns). Furthermore, the minimum angular size of the shower is given by the angular extent of the core of the lateral distribution $\sim 0.1^\circ$ for a few hundred GeV shower. In this way, the pixel size reduced to this angular scale gives an improvement in both triggering and shower reconstruction. Finally, to resolve the structure of the shower image, the angular resolution of the telescope should be 0.1° .

3.3.1 Hadronic Shower

The hadronic shower is initiated when charged cosmic-rays, mostly protons and alpha particles, interact with the atmosphere and gives origin to secondary particles cascade. Most of the created particles are pions (90%), then kaons (10%) and other hadrons (p, \bar{p}, n, \bar{n}) as shown below in fig. 3.6.

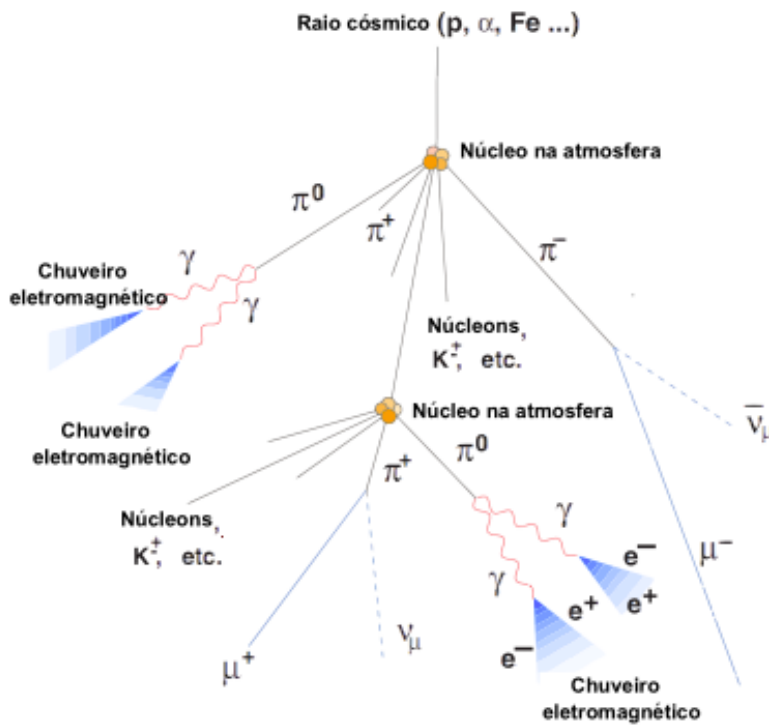


Figure 3.6: Schematic development of the hadronic shower. Credits:[47]

The production of particles via hadronic interaction continues until the energy per nucleon is smaller than the energy threshold for pair production of pions ($\sim 1\text{ GeV}$). Charged

pions sometimes decay into muons and neutrinos before interacting again, where the muons basically only interact via ionization, meaning that they mostly undergo unabated to the ground. The pions (π^0) have a short lifetime ($\tau_{\pi^0} \approx 10^{-17} s$) while the charged pions (π^\pm) have a longer life ($\tau_{\pi^\pm} \approx 10^{-8} s$) before decaying into muons.

With the decay of π^0 into $\gamma\gamma$ an electromagnetic sub-shower is developed. This process suppresses the hadronic interaction and the initial energy of the hadronic shower ends up in electromagnetic components.

3.3.2 Gamma-Hadron separation

It is a big challenge separating the hadronic showers from the gamma showers to achieve a significant suppression of the background created by the cosmic-rays, although there are some significant differences between them.

Considering the fact that hadronic interactions produce much more particles than in the electromagnetic interaction, we have that the hadronic shower is much more spread sideways than the electromagnetic one. With this, at large distances from the shower axis, we have much more light in the hadronic shower than in the electromagnetic one. In fig. 3.7 we show an illustration of both types of showers. For these same reason, electromagnetic showers are more compact, and we have a much more pronounced Cherenkov ring in the electromagnetic shower than in the hadronic one. Considering the small lateral extent of the electromagnetic shower, the Cherenkov image that appears in the camera of the telescope is an ellipse (dependent of the energy of the shower and the relative core location).

By combining several images of a same shower it is possible to reconstruct the location of the source that gave origin to the primary γ -ray. For hadronic showers, instead, the galactic and extragalactic magnetic fields make the direction of the cosmic rays to be isotropic, facilitating therefore the separation of gamma-ray from cosmic-ray induced shower events.

3.3.3 Imaging technique

The basic principle of the Imaging technique is the primary particles arriving at the atmosphere, interacting with it and generating secondary particles and Cherenkov radiation. The radiation will reach the ground and be reflected by the mirrors of the telescopes sitting inside the Cherenkov light pool, and be captured by the cameras.

The photomultiplier cameras are composed by an arrangement of pixels with detectors that convert the Cherenkov photon into a photoelectron and amplifies this to a measurable current. This signal can be combined to estimate the number of Cherenkov photons that hit each pixel. By combining several photomultipliers, the camera registers the intensity of the signal and its arrival time in each pixel creating in this way an image of intensities at

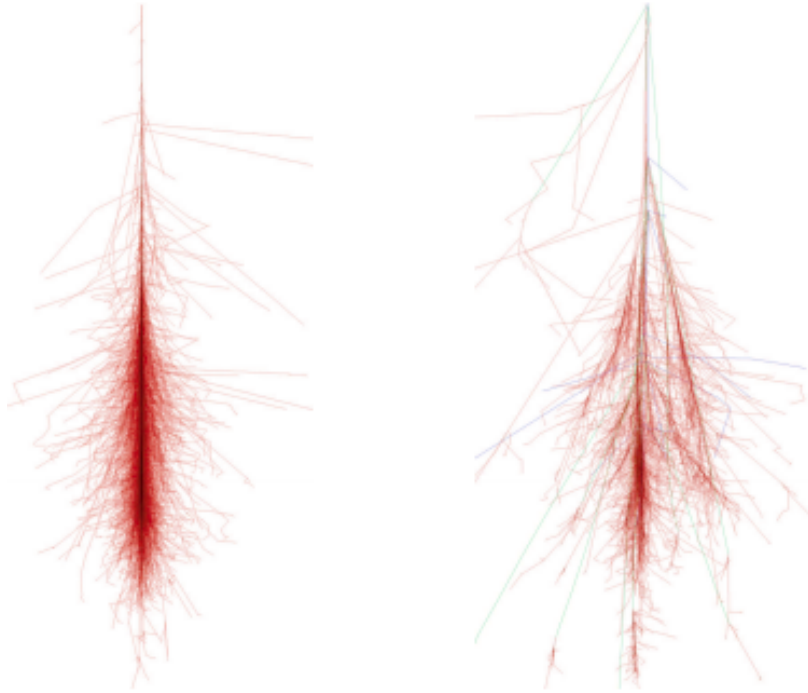


Figure 3.7: Left: electromagnetic gamma shower. Right: Hadronic proton shower. The initial energy for both particles is 100 GeV. As expected the hadronic shower is much more spread than the electromagnetic. In fact, the hadronic shower looks like a collection of sub electromagnetic showers. Credits: [47]

the camera.

In 1985, Hillas [29] proposed a series of parameters that characterize the shape and orientation of the Cherenkov images in the cameras. The fig. 3.8 below exhibits these original parameterisation by Hillas and one possible example of Cherenkov image of the shower as detected in the camera.

The original Hillas parameters used in the gamma/hadron separation for monoscopic observations are listed below, for reference, even if today observations are usually stereoscopic and other techniques, frequently based on neural networks, are used for gamma/hadron separation:

$$\begin{aligned}
 Distance &= \sqrt{\langle x \rangle^2 + \langle y \rangle^2} \\
 Width &= \sqrt{\frac{\sigma_x^2 + \sigma_y^2 - z}{2}} \\
 Miss &= \sqrt{\frac{1}{2}(u \langle x \rangle^2 + v \langle y \rangle^2) - \left(\frac{2\sigma_{xy} \langle x \rangle \langle y \rangle}{z} \right)} \\
 Alpha &= \sin^{-1} \left(\frac{Miss}{Distance} \right)
 \end{aligned}$$

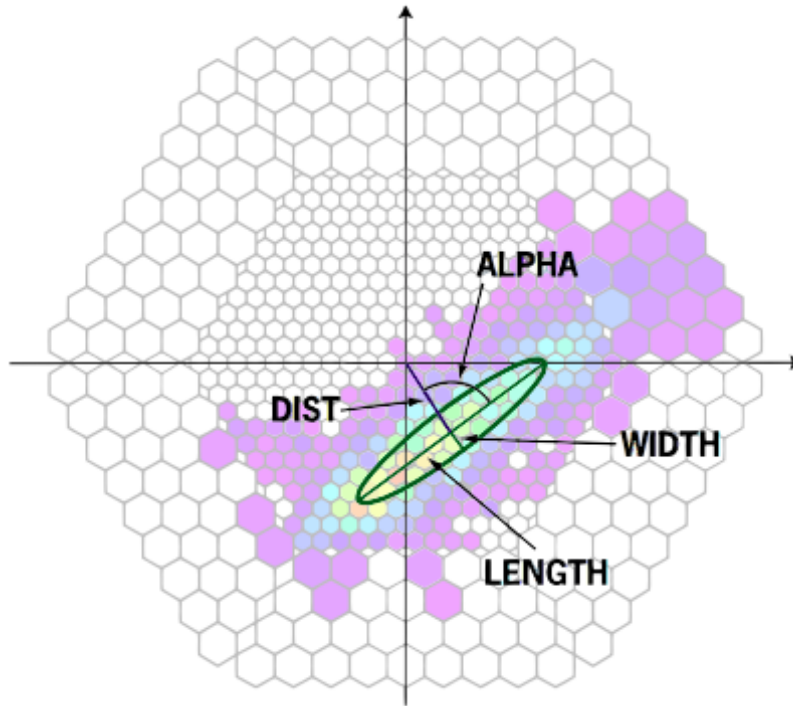


Figure 3.8: Hillas parameters used to described the Cherenkov image at the camera. Adapted from: [25]

$$Lenght = \sqrt{\frac{\sigma_x^2 + \sigma_y^2 + z}{2}}$$

where $z = \sqrt{d^2 + 4\sigma_{xy}^2}$, $d = \sigma_x^2 - \sigma_y^2$, $u = 1 + \frac{d}{z}$ and $v = 2 - u$. A thorough description of these parameters is given by Fegan [24]. The parameter Miss is the perpendicular distance between the major axis of the image and the centre of the field of view of the camera.

3.3.4 Stereoscopy

Stereo imaging is the concept of observation of a same shower simultaneously with at least two telescopes separated by a distance comparable with the size of the Cherenkov light-pool on the ground. An illustration is shown in fig. 3.9. This technique can improve several aspects of the observation in comparison to mono observations, such as angular resolution, energy threshold, the identification of the signature of the hadrons and gamma-rays as well as the suppression of the background of different origins and the reconstruction of the shower in 3d.

The integration area of multi-telescope systems is equivalent to the total geometrical area of the array, as opposed to the effective area of a single telescope which is determined by the radius of the Cherenkov light pool itself.

There are two conditions that dictate the effective energy threshold of the imaging telescopes. The first one determines that the trigger rate due to photons from the night sky

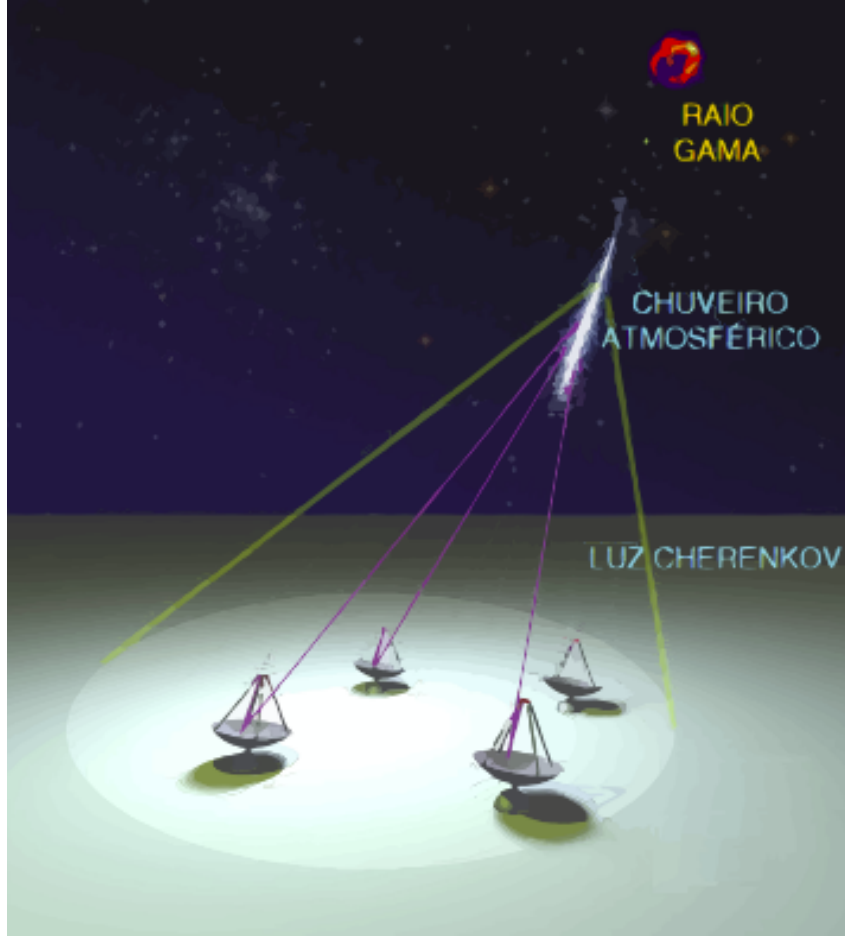


Figure 3.9: Example of an array of telescopes observing a Cherenkov Shower simultaneously. Adapted from: [25]

background (NSB) cannot exceed the detection rate of γ -rays. The trigger criteria for the suppression of the background normally used is the requirement of a signal above the threshold in several neighboring pixels. In this way high-resolution cameras with pixel size ~ 0.1 are more effective in lowering the energy threshold by using high trigger multiplicity. The second condition for the energy threshold is that the number of photoelectrons in the image needs to be great enough for image analysis (~ 100).

3.3.5 Shower Reconstruction

The detection of the Cherenkov shower images with two or more telescopes allow the precise reconstruction of the shower core position through determination of the impact parameter. For the data analysis of multi-telescope observations the Hillas parameters can be extended to derive weighted combinations of the length and width parameters, namely, the mean-scale-width (MSW) and mean-scale-length (MSL) defined as in [19]:

$$MSP = \frac{1}{N_{tel}} \sum_{i=1}^{N_{tel}} \frac{p_i - \langle p_i \rangle}{sd(p_i^{sim}(Z, size, r))}$$

where the parameter p_i can be either length or width. Here $sd(p_i^{sim}(Z, size, r))$ is the standard deviation for a given zenith angle Z , impact distance r and image size, and $\langle p_i \rangle$ is the mean value of the parameter.

Beyond the Hillas image parameters there are additional stereoscopic exhibited in fig. 3.10 – these are “disp1” and “disp2”, which are the related angular distance of the shower image center of gravity from the reconstructed shower direction of origin; and θ which is the angular distance of the reconstructed shower direction from the expected source position. These parameters improve the analysis allowing to calculate new parameters like the height of the shower maximum, which turns out to be very useful for background suppression because the shower cores of electromagnetic showers happens at higher altitude than for the hadronic case.

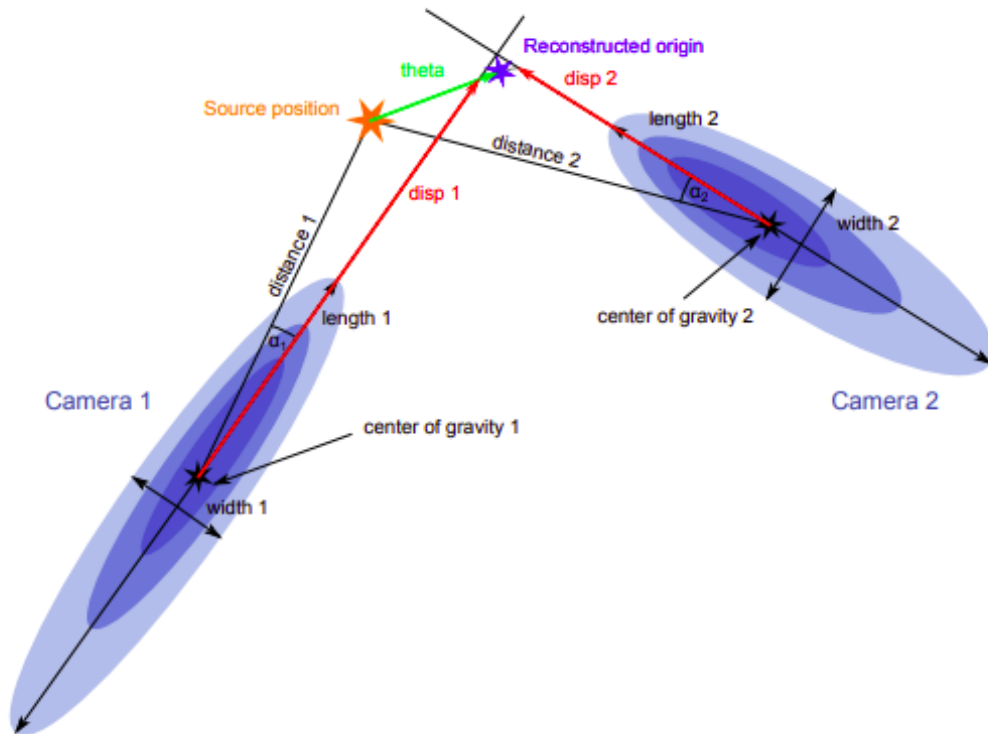


Figure 3.10: Stereo parametrization scheme used for the reconstruction of the Cherenkov shower. Credits: [27]

3.4 CTA Observatory

The Cherenkov Telescope Array will be composed by more than 100 telescopes spread over two sites, 19 of them will be localized in the northern hemisphere in La Palma, Spain at 2200m of altitude, and other 99 telescopes will be in the southern hemisphere in Paranal, Chile, at 2800 m of altitude. The planned layouts of the telescopes in both hemispheres are

exhibited in fig.3.12. The arrangements will improve the capabilities of the telescopes in detecting rapidly variable objects such as AGN flares, Gama Ray Bursts (GRB), etc.

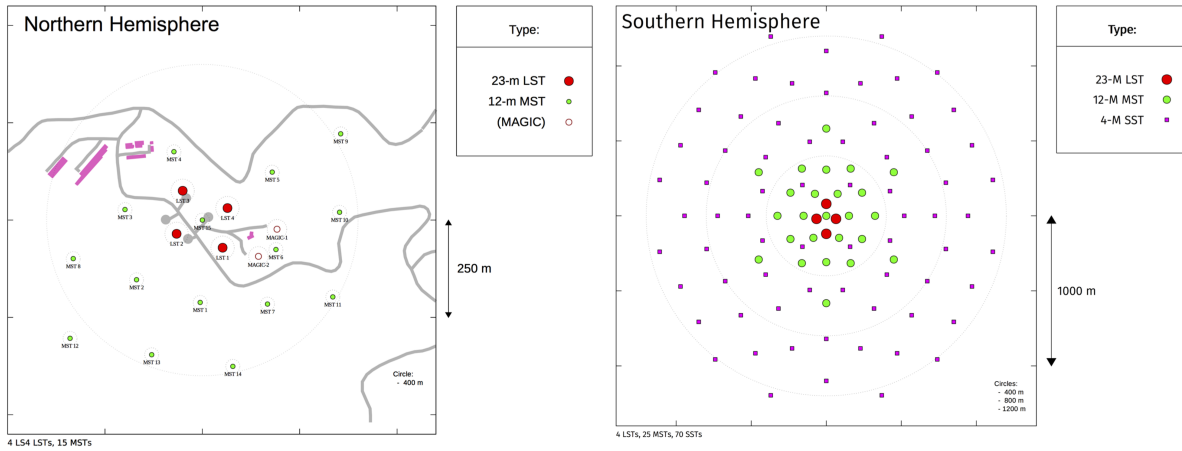


Figure 3.11: Layouts of the telescopes arrays in both hemispheres. Credits: CTA [4]

With the goal of improving the detector sensibility in the energy range from 20 GeV to at least 300 TeV, as well as improving the effective collection area, CTA will use three different sizes of telescopes: 8 being Large-Sized Telescopes (LST), 40 Medium-Sized Telescopes (MST) and 70 Small-Sized Telescopes (SST). The CTA is in the pre-construction phase, where the prototypes are already installed and undergone extensive testing, to make sure that they are functioning as expected. Besides, CTA requires only three telescopes, the CTAC constructed six telescopes and 7 different camera prototypes, after some tests they will choose among them the one that had the best performance. They locate three telescope prototypes close to the labs that developed them (MST, SST GCT and SST 1M), and three other prototypes are already installed at a site appropriated for astronomical observations (LST, SCT and SST ASTRI). Since LST is very large, the prototype has already been installed in the final location, and after commissioning it will become part of the final array. The LST and the SST ASTRI prototypes have in fact already detected their first TeV gamma-ray coming from the Crab Nebula [34].

Currently there are three different SST prototypes. The SST design is a dual-mirror Schwarzschild-Couder aplanatic configuration, where the primary mirror has 4.3 m diameter segmented into hexagonal facets and the secondary mirror is monolithic. The proposed camera consists of 2048 on silicon photomultipliers (SiPMs) pixels which gives a field of view of $\approx 9^\circ \times 9^\circ$. Due to its large field of view, the SSTs were developed to capture the most energetic showers. Since these high energetic showers ($\sim 100 \text{ TeV}$) have very low flux due to the fact that the emission of the sources often follows a power law that rapidly decrease for high energy, CTA will use an array composed of 70 SSTs spread over an area of $\sim 2000 \text{ m}^2$ in the southern hemisphere, raising the chances of capturing the high energetic gamma-rays.

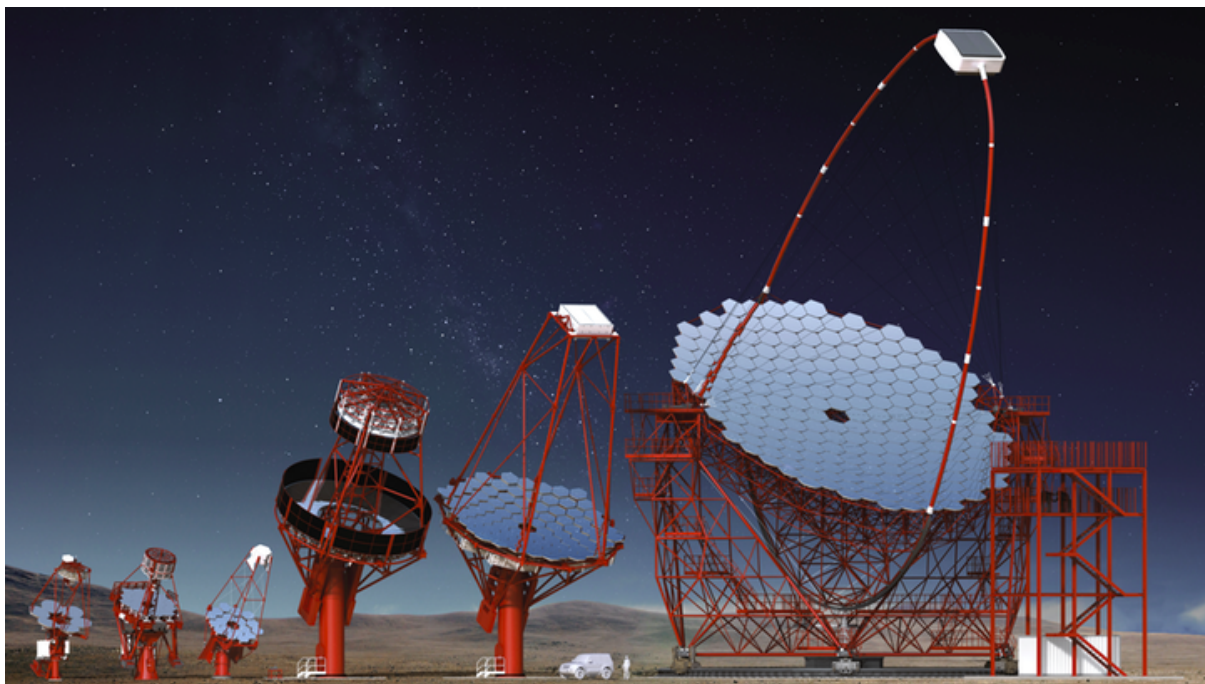


Figure 3.12: In the Left are the three different SST prototype designs, in the medium the two MST prototype designs and in the right the LST prototype design. Image credit: Gabriel Pérez Diaz, IAC [4]

The MST is a modified Davies-Cotton telescope with a reflector diameter of 12 m, and a focal length of 16 m. The reflector is actually a composition of ~ 90 hexagonal-shaped mirrors that are aligned with an active mirror control assembly with the purpose of creating a uniform reflector. There will be 25 MSTs spread in the Southern hemisphere and 15 in the Northern hemisphere. The expected energy range sensitivity of the MSTs is from 150 GeV to 5 TeV. Currently there are two camera prototypes being developed for MSTs. Both cameras use photomultiplier tubes and will have a large field of view ($\sim 8^\circ$) which will allow the MSTs to take rapid scans of the sky.

The LST is an alt-azimuth telescope with a 23 m diameter of parabolic reflective surface, supported by a tubular structure made of carbon fibre and steel tubes. There will be four LSTs in the center of both hemispheres' arrays. The camera of the LSTs is made of photomultiplier tubes which together have a collection area of 400 m^2 . This will provide the LST with an energy range sensitivity of 20 GeV to 150 GeV. With this sensitivity, LST will be capable of detecting galactic transients, high red-shift active galactic nuclei and gamma ray bursts (GRBs). In addition, to be able to detect the GRBs, the LSTs will re-position itself within 20 seconds to any point in the sky.

CTA it is expected to discover more than one thousand new gamma-ray sources in the sky. Likewise, it will provide more precise morphological characteristics of extended sources localized in the galactic plane, and allow for the detection of weaker galactic sources than

the ones known today. CTA will also probe extreme environments like the surroundings of neutron stars and the black hole event horizon, as well as search for the nature of the dark matter leading to an unexplored new physics frontier. The Observatory operations are expected to start in 2022 and the completion of the project construction is expected to happen by 2025. Until there, the data from the prototypes will be available for the consortium to help test and improve the CTA software, but also to do some timely science.

	Large Sized Telescope		Medium Sized Telescope		Small Sized Telescope
	FlashCam	NectarCam	FlashCam	SCT	
Required Energy range(TeV)	0,02 - 3		0,08 - 50		1 - 300
Number of telescopes	4		25 (S) + 15 (N)		70 (S)
Optical designed	Parabolic		Schwarzschild Couder		Schwarzschild-Couder
Primary reflector diameter (m)	23,0		11,5		4,3
Secondary reflector diameter(m)	-		-		1,8
Effective mirror area (m^2) (including shadowing)	370		88		8
Focal length (m)	28		16		2.15
Total weight(t)	103		82		19
Field of view(deg)	4.3		7.5		10.5
Number of pixels in Cherenkov camera	1855		1764		11328
Pixel size (deg)	0.1		0.17		0.067
Photodetector type	PMT		PMT		SiPM
Positioning time to any point in the sky (>300 elevation)(s)	30		90		60

Table 3.1: Main characteristics of CTA telescopes and the three cameras prototypes, where PMT is photomultiplier and SiPM is silicon photo-multiplier. [4]

3.5 Extragalactic Survey

Until today, no extragalactic survey has been performed using IACTs. The wide field of view of CTA, together with the unprecedented sensitivity means that CTA surveys will in general reach one or two orders of magnitude deeper than current datasets. Deeper fields will be obtained for some key regions hosting some prominent targets. At the same time, wider surveys will be making some population samples and searching for the unexpected.

The CTA extragalactic survey will provide datasets of 1000h, covering 25% of the sky to a depth of $\sim 6mCrab$, it will be the first time that such a large portion of the sky is observed uniformly at these energies and with this sensitivity.

The extragalactic survey will provide a catalogue of the detected extragalactic gamma-ray sources containing: the significance of the detection; the source location; the time intervals for the observations and for detected flares, as well as the differential energy spectrum of the source; the integral flux, alongside with variability and the association of the detected signal with known objects. The uniqueness of the survey will enable to search for large scale structures and for new source classes. In addition, it will allow the possibility to study flaring activities in a regime of 0.1 to at least 10 TeV, helping to understand, for example, the flaring duty cycles in blazars. The uniform exposure of the survey will allow the measure of the luminosity function and the number density of sources depending on their flux (the so-called log N - log S distribution). It will be the first attempt for a complete log N-log S study of closeby blazars in very high energy gamma rays.

In the extragalactic sky, the main source gamma-ray-emitting objects are blazars (BL Lacs and FSRQs), which are believed to produce gamma rays inside their relativistic jets, via mechanisms not yet completely understood. We expected the detection of 30-150 blazars within the survey, among them are the extreme blazars (sources with hard spectra and gamma-ray peak in the range of 100 GeV-10 TeV). These objects can help in the study of the extragalactic background light (EBL). Due the high sensitivity of CTA, sources 40 times weaker than the currently known objects will be detected, leading to an increase in distance by a factor of ~ 6

Beyond Blazars, it is expected that CTA will detect clusters of galaxies, Seyfert 2 galaxies and ultra-luminous infrared galaxies (ULIRGs) which are sources that have been proposed to emit VHE gamma rays but none have been detected so far. Aside from that, the survey is sure to detect gamma-ray sources without clear association with known objects (the so-called dark sources) as well as sources where no strong non-thermal emission is detected, which can be a signature of unknown physics, as for example, the decay into gamma rays of a new particle, such as dark matter candidates.

3.6 AGN monitoring

Long-term monitoring program of AGNs is extremely useful to help us understand the complex variability properties of these objects. The long-term monitoring program of CTA became necessary for several reasons, amongst them is to identify the quiescent states of a sample of AGNs and estimate their duty cycle (i.e. the probability of being active at a given time) as well as send signals for targets of opportunities during specific events.

Characterize the VHE variability properties of AGNs is also very important to define the mechanisms at the origin of the temporal evolution, and to distinguish features induced by specific bursts. Long-term multiwavelength monitoring also contributes to identify the various emission zones, and to find they location relatively to the others. With the CTA long-term monitoring we should be able to clarify whether the VHE variability is dominated by the jet physics or if the origin of the variability primarily lies in the accretion flow, as well as to distinguish between variability due to the dynamics of the central engine from the variability caused by radiative processes.

In the long-term monitoring program of CTA it will be provide long-term light curves and time resolved spectra for a well-sampled sources covering all types of AGNs (UHBL, HBL, IBL, LBL, FSRQs, and radio galaxies). Each source will be observed on average ~ 30 min once a week during its period of detectability with full array. This would result in ≈ 12 h per year per source, leading to greater than seven standard deviation ($> 7\sigma$) detections of the sources in their low-activity state, sufficient for construct their spectra. For the brighter sources, the spectra can be extracted once a week or a month. Altogether, the regular observations will permit tracking of the flux variability of all sources in the form of long-term light curves.

For the currently proposed list of sources (see table 4.1), the total exposure time (180 h) would be split into 132 h of yearly observation time for the north array and 48 h for the south array. Even though the goal of this program, i.e. study the long-term flux variation, can be achieved with LSTs and MSTs, the observation with SST component in the north array would be useful for extending the spectral coverage of HBLs and UHBLs during high states above 10 TeV with good sensitivity.

After five years of operation, the list of the sources will be reviewed and reduced to the ten most interesting objects, in terms of variability patterns, for further monitoring over at least more ten years.

Beyond the studies of intrinsic AGN properties, monitoring AGNs at different redshifts will also provide constraints on cosmic background radiation and in some fundamental physics of the space-time. Indeed, the long-term monitoring of AGNs is thought to focus on variability, it is possible to pursue different scientific goals that requires almost the same type of data.

Chapter 4

CTA Data Challenge

4.1 Introduction

The Cherenkov Telescope Array (CTA) will improve our understanding of gamma-ray astrophysics. CTA will cover a photon energy range from 20 GeV to at least 300 TeV, and improve several performance aspects in comparison with the current generation of Imaging Atmospheric Cherenkov Telescopes (IACTs). The detection sensitivity will reach about 1/1000 of the Crab Nebula flux (1 mCrab) within 50 hours of observing time, which will provide access to populations of TeV sources over the entire Galaxy, and allow to detect AGN variability on a sub-minute time scale. The field-of-view will vary between 4-8°, depending on telescope type, making it possible the detection of extended and diffuse sources of gamma-ray emission. In the highest energies, the angular resolution will achieve about 1 arcmin, providing the necessary resolution to resolve Supernova remnants and nearby starburst galaxies. [34]. CTA, together with experiments throughout the spectrum of observational techniques, will allow for multi-messenger and multi-wavelength science that can lead us to a better understanding of the universe.

Today there are 227 TeV-emitting sources known (according to the TevCat Catalogue – <http://tevcat.uchicago.edu/>). These gamma-ray sources can be associated with pulsars, supernova remnants (SNRs), starburst galaxies and active galactic nuclei (AGN). Those places are the most powerful accelerators of particles in the universe and to understand how cosmic particle acceleration happens is one of the fundamental questions of astrophysics that CTA will allow us to explore. Overall, the CTA science goals comprise three major themes: [22]

Theme 1: Understanding the Origin and Role of Relativistic Cosmic Particles

Theme 2: Probing Extreme Environments

Theme 3: Exploring Frontiers in Physics

To answer the questions inside each of these themes (already detailed in chapter 3)

the CTA Consortium (CTAC) – composed by scientists from all over the world who were responsible for first proposing and designing CTA – prepared a science program made by one Program of Dark Matter Search and 9 Key Science Projects (KSPs) which are a set of surveys and observations projected to efficiently address the multiple science questions within the CTA themes. The CTA KSPs are:

- Galactic Centre Survey (GC): The inner portion of our galaxy contains several gamma-ray emitters like the Super Massive Black Hole (SMBH), Supernova Remnants (SNRs), dense molecular clouds and strong massive stellar activity. The aim of this KSP is to better understand the acceleration of the cosmic rays in the central region and the nature of the central gamma-ray source.
- Galactic Plane Survey (GPS): The goal of this KSP is to provide a census of the Galactic gamma-ray sources as SNRs, Pulsar Wind Nebulae (PWNe), detect new sources of TeV gamma-rays, in particular PeVatrons – sources emitting gamma-rays up to and beyond 100 TeV, and therefore able to produced cosmic-ray particles of PeV energies, equivalent to knee of the cosmic-ray spectrum –, as well as provide a list of promising targets for deeper targeted observations in the future.
- Large Magellanic Cloud Survey (LMCS): Similarly to the GPS, this galaxy offers populations of SNRs, PWNe and the possibility to study the transport of the cosmic rays into the Interstellar medium. The galaxy is host to some of the most active star-forming regions known, and therefore provides a different perspective into the cosmic-ray propagation studies than we would see at our own Galaxy, allowing us to a better understanding of the phenomenon.
- Extragalactic Survey (EGAL): The main objective of this KSP is to construct an unbiased Very High Energy extragalactic catalogue with sensitivity limit of 6 mCrab above 125 GeV. The EGAL Survey will connect with the GPS in such a way that all Galactic latitudes will be covered.
- Galactic Clusters: Galactic clusters are great environments to find cosmic rays accelerated by structure formation process and AGNs. The goal of this KSP is to detect diffuse gamma-ray emission from clusters of galaxies, as well as to probe how cosmic-ray particles (mainly protons) can impact on the cluster environment, besides the study of cosmic-ray acceleration, propagation and confinement itself.
- Cosmic Ray PeVatrons: The first plan of this KSP is to make deep observations of the already-known sources with hard spectra ($\approx E^{-2}$). Then try to understand how in the Galaxy the cosmic rays are accelerated up to PeV energies and what is the distribution of PeVatrons over the Galaxy, as well as to look for new sources, in conjunct with the GPS KSP.

- Star Forming Systems (SFS): The SFS KSP will provide the relation between the high energy particles and the Star Formation Rate in systems on several scales, trying to understand how is the impact when particles are accelerated in the surroundings of the Interstellar medium.

The final two KSPs, dedicated to the study of AGNs and Transient Phenomena in General, are the scientific focus of this work. The Transient phenomena KSP will cover the catastrophic events from neutrons stars and black holes (BH). Six different classes of targets were proposed for study: Gamma Ray bursts (GRBs); High energy neutrino transients; Galactic Transients; Gravitational Wave transients; X-ray, optical and radio transients and Serendipitous VHE transients. Their goal is to find the astrophysical origin of these sources and the physical mechanisms that drives them. In the AGN KSP the goal will be to understand of how such a small region as the BH event horizon has capacity to accelerate particles up to very high energies. This knowledge can help us explain how is the emission of blazars, what causes their variability from small to long time scales, where the emission of the radio-loud galaxies originates, and what classes of AGN emit very-high energy photons.

To support the science of the KSPs, the first CTA data challenge was created, as a set of tasks which will be described in the next section, simulating the observations of each KSP during the first three years of operations of CTA. CTA will partly operate as an open-proposal observatory. The CTA Consortium will have 40% of the time of CTA to explore the KSPs and, after some proprietary period, the KSPs data will be publicly released through the CTA data archives.

4.2 Data Challenge

The data analysis software of CTA is currently under implementation and is under extensive testing. In 2017 CTAC created the first of a series of planned data challenges, each one aimed at a different focus and with increasing level of realism, associated with instrumental imperfections and the detection process.

The Data Challenge is a set of simulated high-level science data i.e, event-reconstructed properties such as direction, energy and time of the gamma-ray showers. The focus of the data challenge is to familiarize the scientists with the CTA analysis tools, prepare the community for the analysis with the real data, as well as to ultimately validate the features of the purpose-built science tools packages. It also aims at encouraging the development of new algorithms and make sure that CTA data and tools are as compatible as possible with the external resources available in the community. [13]

At first, four KSPs were simulated for the first data challenge (DC-1), being them the Galactic Plane Scan (GPS), the Galactic Centre Survey (GC), the Extragalactic Survey (EGAL) and an Active Galactic Nuclei (AGN) monitoring program. Each KSP is responsi-

ble for developing some science tasks that can be investigated with the data available in the data challenge. For the Galactic sky model all the known bright sources were taken from the gamma-cat catalogue (<https://gamma-cat.readthedocs.io/index.html>). The fermi bubbles and the bright pulsars were taken from fermi-lat, being that only the 12 most energetic pulsars were considered from the first FHL catalogue (<https://fermi.gsfc.nasa.gov/ssc/data/access/lat/1FHL/>). The SNR were taken from the study of Cristofari et al, published in 09 August 2013 (<https://doi.org/10.1093/mnras/stt1096>) where only young SNR were simulated. Lastly the 5 known gamma-ray binaries were modelled: LS 5039, LS I+61 303, PSR B1259-63, 1FGL J1018.6-5856 and HESS J0632+057.

The extragalactic survey is proposed to cover a fourth of the sky with full-array observations of ≈ 1000 h over the first 10 years of CTA operations. In the first data challenge 500h of observations were simulated. The extragalactic sky model has in total 551 sources reported as extragalactic objects or unidentified sources with $|b| > 10^\circ$. Among these sources, 46 were taken from TeGeV Catalog (<https://www.ssdsc.asi.it/tgevcats/>) with an additional of 11 sources also reported in the TeGeV Catalog but with no redshift reported, later found in 2FHL. Another 271 sources were taken from 1FHL but from these 271, 87 did not have redshift reported, so the redshift was taken later from 2FHL catalog. Subsequently it was simulated more 185 sources with redshift selected from 3FGL, being them:

- 60 Flat Spectrum Radio Quasars (with redshift < 1.4),
- 68 High Synchrotron Peaked BL Lacs (where sources without redshift are put at the average redshift of BL Lac objects from 3LAC, $z = 0.4$),
- 24 Intermediate Synchrotron Peaked BL Lacs ($10^{14} < \text{synchrotron peak} < 10^{15}$, index in 3FGL < 2.25),
- 23 Low-frequency peaked BL Lacs (synchrotron peak $< 10^{14}$, index in 3FGL < 2.25),
- 2 Narrow Line Seyfert 1,
- 6 Radio Galaxies (index from 3FGL < 2.2 ; Variability index in 3FGL > 20),
- 2 Starburst Galaxies (NGC 253 and M 82)

Finally, there are 38 additional sources from 2FHL catalog, giving us the total of 551 sources. All these source models can be found at (http://cta.irap.omp.eu/ctools/users/tutorials/1dc/getting_data.html) inside the .tar.gz file containing the .xml (from eXtensible Markup Language) model, together with the files of the spectral information and the fits files. The proposed region simulated for the extragalactic survey can be seen in fig 4.1 below:

CTA will be very important for the study of AGNs. Allowing to probe the physical mechanisms that happen in these extreme environments, such as acceleration of particles,

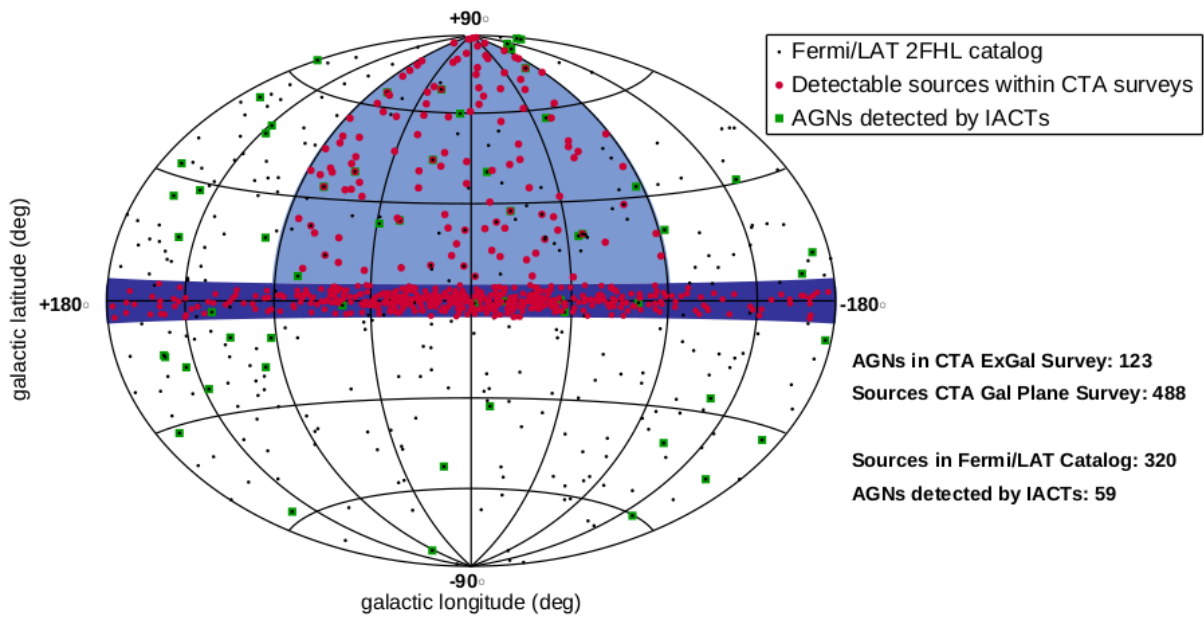


Figure 4.1: Region proposed for the extragalactic survey in light blue. The GPS is indicated in darker blue. The red points are a hypothetical example of the sources to be detected in the survey. The black points are the extragalactic and unidentified Fermi-LAT hard-spectrum sources (2FHL catalogue) and the green points show the AGNs that have already been detected so far by IACTs. Credits [22].

the origin of the extreme variability, formation of jets and the nature of the central black hole. To help solve these phenomena, it is necessary to look at different classes of AGN at different redshifts, and for that we need high-quality spectra, flux and spectral variability data on all timescales. Thus the key data products of the AGN variability program will include long-term monitoring light-curves, high quality spectral data, high resolution light curves during flares, as well as the timely detection and provision of alerts to other facilities concerning AGN flares, so that they can follow the very high energy (VHE) flux state in multi-wavelength observations.

In our particular task in the Data Challenge, we were interested in preparing the study of the origin of the variability in AGN, which can vary from few minutes to few years. The observations of the AGN KSP cover flux variations in three different time scales. The slow (annual timescales) and intermediate (timescale of days, weeks and months) will be part of the long-term monitoring program, which will provide light curves with regular (weekly) sampling over several years. Rapid variability (timescale of hours, minutes) will be carried out within the AGN flares program, which together with other multi-wavelength data will provide detailed data sets for time series analyses [22].

Here we will focus on the long term monitoring program. In this task our goal was to recover the light curves of the 24 simulated AGN variability models from the DC monitoring program (http://cta.irap.omp.eu/ctools/users/tutorials/1dc/getting_data.html).

Each KSP group provided the data, in other words the flux from a certain region of sky, in the form of XML files. The models provided were consistent with already existent TeV and Fermi-Lat data, and in some cases the spectra were extrapolated up to high TeV energies applying a redshift and energy-dependent absorption correction according with the EBL model of Franceschini et al(2008) [[26]]. For the AGN KSP, in total, 24 sources out of the 35 sources in the Fermi-LAT monitoring list were selected for temporal simulation in the first data challenge. All the 24 simulated sources are exhibited in the picture 4.2 and in the table 4.1 below:

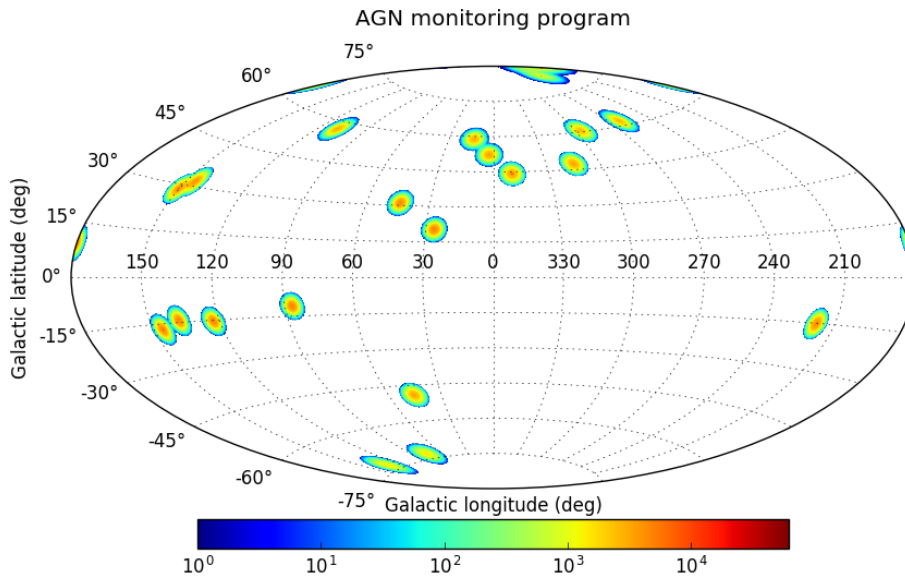


Figure 4.2: Simulated events for AGN monitoring program in the sky. Credits: Jürgen Knödlseeder, 08/25/2017

Table 4.1: AGN simulated sources for the long term monitoring

Sources	Right Ascension	Declination	Redshift	Flux($ph\,cm^{-2}\,s^{-1}$)	Spectral Index	Pivot Energy (GeV)
TeVJ0222+4302	35.665	43.0355	0.34	195.7	2.19	22.0253
TeVJ0721+7120	110.472	71.3434	0.127	93.25	3.43	19.0716
TeVJ1224+2122	186.227	21.3796	0.432	74.33	3.75	19.957
TeVJ1512-0906	228.2175	-9.106	0.361	73.5	3.26	17.5867
2FHLJ1104.4+3812	166.11958	38.20728	0.031	124	2.14	26.2669
2FHLJ1256.2-0548	194.06	-5.80458	0.5367	53.68	4.44	15.066
2FHLJ0622.9+3325	95.735	33.42808	0.000	12.08	3.14	17.338
2FHLJ1437.0+5639	219.26875	56.66039	1.003	29.91	3.12	15.2588
1FHLJ0007.7+4709	1.9469	47.1547	0.28	14.535	3.57	14.000
1FHLJ0050.6-0930	12.6716	-9.5104	0.63	17.94	2.175	21
1FHLJ0136.8+4754	24.2079	47.9013	0.859	9.73	3.468	14
1FHLJ0617.6-1716	94.4133	-17.2813	0.098	13.95	2.752	18.305
1FHLJ0805.4+7534	121.3687	75.5746	0.121	20.89	2.195	22.030
1FHLJ1154.0-0010	178.5248	-0.1693	0.254	11.61	2.211	21.356
1FHLJ1221.6+2814	185.4021	28.2473	0.103	34.07	2.181	22.451
1FHLJ1230.3+2522	187.5859	25.3769	0.135	7.27	3.292	15.281
1FHLJ1344.0-1722	206.0008	-17.3806	2.506	14.37	5.349	11.958
1FHLJ1504.3+1029	226.0951	10.4883	1.839	59.24	4.568	12.765
1FHLJ1512.2+0204	228.0644	2.074	0.219	11.07	2.977	16.612
1FHLJ1719.1+1745	259.7982	17.7502	0.137	19.15	2.849	19.166
Continued on next page						

Table 4.1 – continued from previous page

Sources	Right Ascension	Declination	Redshift	Flux $e - 11(phcm^{-2}s)$	Spectral Index	Pivot Energy (GeV)
1FHL J1730.7+0017	262.7	0.2974	1.335	11.9	3.242	15.509
1FHL J2116.2+3339	319.0518	33.6624	0.35	35.64	2.792	17.117
1FHL J2150.2-1413	327.5722	-14.2231	0.229	8	1.747	31.806
1FHL J2345.0-1556	356.2607	-15.9372	0.621	36.42	2.531	18.618

Table 4.1: All the point sources have a power-law type spectrum, where the spectral index is the best fit photon number power-law index and the pivot-energy is the energy at which the error on differential flux is minimal. The flux was obtained integrating the photons from 10 to 500 GeV according to 1FHL. The data of the first four sources were obtained from TeVcat catalogue(<http://tevcat.uchicago.edu/>), the fifth to ninth sources were taken from 2FHL(<https://fermi.gsfc.nasa.gov/ssc/data/access/lat/2FHL/>) and the remaining ones from 1FHL (<https://www.ssdsc.asi.it/fermi1fhl/>)

4.3 Data Model

In gamma-ray astronomy it is very difficult a priori to define if the observed event (i.e., photon) belongs to a source or to the background. To do that it is necessary to make a statistical treatment based on morphology, temporal variation and spectral characteristics of the event. Hence, the general data model used in ctools (a software package of CTA better described below) is split into spatial, spectral and temporal components [8]:

$$M(p, E, t) = M_{spatial}(p|E) \times M_{spectral}(E) \times M_{temporal}(t)$$

where $[M] = [ph \times cm^{-2} \times s^{-1} \times MeV^{-1} \times sr^{-1}]$

The spatial model describes the energy dependent morphology of the source; in the case of AGNs, this is a point source defined by the observational Point Spread Function, PSF, which is in turn a function of the energy of observations [see [12]]. The spectral model describes the spatially integrated spectral distribution of the source, and the temporal model describes the relative variation of the source flux with respect to the mean value given by the spectral model [8]. In the particular case of this first data challenge, the source's spectral model does not include any spectral variability, so that the flux is (unrealistically) modelled to vary equally at all energies, for simplicity.

The spectral model of the sources used in this analysis (table 4.1) is described by a power law function:

$$M_{spectral}(E) = k_0 \left(\frac{E}{E_0} \right)^\gamma$$

where k_0 is the prefactor ($ph \ cm^{-2} \ s^{-1} \ MeV^{-1}$), γ is the index and E_0 is the pivot energy (MeV) in other words is the energy at which the function above was normalized, in this analysis the pivot energy for all the sources was of 300000 MeV.

The original light curves of the simulated sources shown previously (fig. 4.2) were provided in a FITS file consisting of a binary table of TIME (seconds) and a normalization (NORM) which represents the light curve $r(t)$ at the time t , defined between 0 and 1. Below we show an example for the source PKS0716+714 (see figs.4.3 and 4.4). To read the FITS file we use e.g. NASA's software -fv (<https://heasarc.gsfc.nasa.gov/docs/software/ftools/fv/>).

To recover the source flux we have to multiply the NORM column for the normalization value stored in the CTA AGN XML model database, together with the values of Prefactor and Scale, then analytically integrating in the expected range of energy (0.03 to 50 TeV in our case). So the flux is:

$$\text{Flux} = \int_{e_{min}}^{e_{max}} K_0 \left(\frac{E}{E_0} \right)^{-\gamma} dE = \frac{k_0}{E_0^{-\gamma}} \frac{E_{max}^{-\gamma+1}}{-\gamma+1} - \frac{E_{min}^{-\gamma+1}}{-\gamma+1}$$

$[Flux] = [ph/cm^2/s]$

```

fv: Header of lightcrv_0716+714.fits[1] in /home/amanda/ctools/lightc...
File Edit Tools Help
Search for: [ ] Find Case sensitive? No
XTENSION= 'BINTABLE' / binary table extension
BITPIX = 8 / array data type
NAXIS = 2 / number of array dimensions
NAXIS1 = 16 / length of dimension 1
NAXIS2 = 2927 / length of dimension 2
PCOUNT = 0 / number of group parameters
GCOUNT = 1 / number of groups
TFIELDS = 2 / number of table fields
EXTNAME = 'Time profile' / name of this extension
MJDREFI = 59000 / [days] Integer part of time reference MJD
MJDREFF = 5.0000000000E-01 / [days] Fractional part of time reference MJD
TIMEUNIT= 's' / time unit
TIMESYS = 'TT' / time system
TIMEREF = 'LOCAL' / time reference
TTYPE1 = 'TIME'
TFORM1 = 'ID'
TTYPE2 = 'NORM'
TFORM2 = 'ID'
HISTORY File modified by user 'jungen' with fv on 2017-08-23T21:35:59
END

```

Figure 4.3: FITS header of the light curve file, where we can get information such as the dimension, length of the table and the reference MJD where observations started.

Table 4.2 below shows a printout of the model file for the source PKS0716+714, showing additional information such as the type of the source, type of the spectral model, as well as the already-mentioned model parameters Prefactor, Index and Scale.

Source Type: Point Source	Name: TeV_J0721+7120
Spectrum Type	
Power Law	
Parameter scale = 1e-17 name = Prefactor value = 2.40000	
Parameter scale = -1.0 name = Index value = 3.45	
Spatial Type	
SkyDirFunction	
Parameter scale = 1.0 name = RA value = 110.472	
Parameter scale = 1.0 name = DEC value = 71.3434	
Temporal Type	
LightCurve	
file = lightcrv_0716+714.fits Parameter scale = 1e+01	
name = Normalization value = 1.12670	

Table 4.2: Model file of the source PKS0716+714 containing the source type, spectral, spatial and temporal models. Where RA is the right ascension coordinate of the source, DEC is the declination, Prefactor and Index are the components of the power law function used to describe the source, already described above, and lastly the light curve file contain the values of time and normalized flux which needs to be multiplied by normalization value and scale to recover the real value. To recover all the different parameters real value it is necessary to multiply each value by the correspondent parameter scale.

This analytical treatment is valid for the first 9 sources of the table 4.1. For the last

	TIME	NORM
Select	ID	ID
<input checked="" type="checkbox"/> All		
Invert	Modify	Modify
1	0.000000000000E+00	8.875451236963E-02
2	8.640000000000E+04	8.875451236963E-02
3	1.728000000000E+05	8.875451236963E-02
4	2.592000000000E+05	8.875451236963E-02
5	3.456000000000E+05	8.875451236963E-02
6	4.320000000000E+05	8.875451236963E-02
7	5.184000000000E+05	8.875451236963E-02
8	6.048000000000E+05	8.875451236963E-02
9	6.912000000000E+05	8.875451236963E-02
10	7.776000000000E+05	8.875451236963E-02
11	8.640000000000E+05	8.875451236963E-02
12	9.504000000000E+05	8.875451236963E-02
13	1.036800000000E+06	8.875451236963E-02
14	1.123200000000E+06	8.875451236963E-02
15	1.209600000000E+06	8.875451236963E-02

Figure 4.4: Extract of the original light curve with the columns of norm and time. The time in the table is given in seconds so it was necessary to convert the TIME column to MJD dividing by 86400 s and adding the reference MJD where the observation started.

15 sources of the table the values of the spectral parameters were not available in the CTA database, so it was necessary to reconstruct the spectral model numerically. In this case the spectral model is available in the dat format, consisting of a binary table with columns of energy (MeV) and differential flux values ($phcm^{-2}s^{-1}MeV^{-1}$) and the only parameter is a multiplicative normalization(N_0):

$$M_{spectral}(E) = N_0 \frac{dN}{dE}$$

Below we show an example of the available model for the source Ton599 where we had to reconstruct the spectral model numerically (see table 4.3).

To calculate the flux numerically, first we interpolated the points of the spectral table and, after that, we integrated in energy and multiplied by the normalization.

Each source used in this analysis (see table 4.1) was observed in one weekly pointing of half an hour, for a total period of 80 weeks. The simulated dates for the AGN monitoring were from MJD59215 to MJD59769.

There are two current software prototypes for CTA science analysis tools: ctools and gammapy. Gammapy is an open source package made by the CTA consortium for analy-

Source Type: Point Source	Name: 1FHL_J0805.4+7534
Spectrum Type	
FileFunction file = spectra_1FHL_J0805.4+7534.dat Parameter scale = 1e+00 name = Normalization value = 1.00000	
Spatial Type	
SkyDirFunction Parameter scale = 1.0 name = RA value = 121.3687 Parameter scale = 1.0 name = DEC value = 75.5746	
Temporal Type	
LightCurve file = lightcrv_Ton599.fits Parameter scale = 1e+01 name = Normalization value = 2.02500	

Table 4.3: Model file of the source Ton599 containing the source type and the spectral model file. Where RA is the right ascension coordinate of the source, DEC is the declination, Prefactor and Index are the components of the power law function used to describe the source, already described above, and lastly the light curve file contain the values of time and normalized flux which needs to be multiplied by normalization value and scale to recover the real value. To recover all the different parameters real value it is necessary to multiply each value by the correspondent parameter scale. The spectra file contains columns of energy and the correspondent flux for each energy value.

sis of gamma-ray events. The DC-1 has been a great opportunity to test and improve the gammapy, but its features are not complete and stable yet, moreover its complete documentation is still under development. Thus we chose ctools to perform the time series analysis of the AGN monitoring KSP program, and recover the simulated source light-curves.

4.4 Ctools

Ctools is an open source software package developed for analysis of the Cherenkov Telescope Array (<http://cta.irap.omp.eu/ctools/about.html>). Its construction was made by the CTA Consortium and was inspired by the Fermi software -ftools- which also influenced the High Energy Astrophysics Science Archive Research Center (HEASARC) to create a standard software for X-ray astronomy that makes the x-ray analysis easy and more accessible for the scientists. Since these standard tools still did not exist for ground-based gamma-ray astronomy, ctools was created to provide an easy and complete analysis of the public gamma-ray data that will be generated by CTA.

Ctools is conceived to work on level 3 data (DL3), using as input the event files for the gamma-rays that produce Cherenkov showers in the atmosphere to generate final products such as sky maps and spectra. Ctools is made to be compatible also with data of all the current Imaging Atmospheric Cherenkov Telescopes (IACTs), such as H.E.S.S, MAGIC and VERITAS, thus being a standard ground-based gamma-ray analysis tool. In fact, a first set

of real data was already analysed using ctools, after HESS release some observations of the sources Crab nebula, MSH 15–52, RX J1713.7–3946, and PKS 2155–304 (see [35]). In general the analysis methods showed a good agreement between ctools results and the ones release by HESS collaboration, indicating that ctools is a good candidate for CTA data analysis. [33]

Each tool of the ctools package performs one step of the analysis and can be implemented using the executable scripts written in C++(ctool) and Python(cscript). The diagram 4.7 shows all tools available in ctools classified according to their functionality.

4.4.1 Data structure

The ctools data structure is divided into observations with a fixed pointing direction. The duration of each observation is 30 minutes for the Galactic Plane, 25 minutes for the Extragalactic Survey, 30 minutes for the Galactic Centre surveys, and 15 minutes for the AGN monitoring program. The simulations are divided in a simplified scheme, where for the equivalent of the first three years of CTA operations, 1980 hours were scheduled for the Southern array(S) and 1815 hours for the Northern array(N). The distribution of these simulated hours amongst the KSPs are:

KSP	Duration	Pointings	Simulated dates
Galactic Plane Survey	1620h (1020 S, 600 N)	3270	2021-01-01 - 2021-04-18
Galactic Centre Survey	825h (S)	1671	2021-01-01 - 2021-03-29
Extragalactic Survey	500h (200 S, 300 N)	1271	2021-01-01 - 2021-02-25
AGN monitoring	960h (N)	1920	2021-01-01 - 2022-07-09

In reality the date intervals of the four KSPs overlap and do not coincide with any particularly relevant real period in time. For the surveys, each day is arbitrarily split into 10 hours night time and 14 hours daylight. For the AGN monitoring, all sources are visited in sequence one time before moving to the next week. The data are provided in FITS format for the baseline arrays.

Ctools works with event lists (DL3). The events are described by the Instrument Response Function (IRF). The IRF is provided as FITS binary tables where each row corresponds to a registered event and each column to a property of the event. The IRFs describe how the reconstructed photon arrival direction p , energy E and trigger time t are connected with a real event with incident direction p , energy E and time t of a photon, p .

$$e(p', E', t') = \int dpdEdtR(p', E', t'|p, E, t) \times I(p, E, t)$$

where $e(p,E,t)$ is the expected event rate as function of the reconstructed direction p , energy E and trigger time t ; $I(p,E,t)$ is the gamma-ray intensity arriving at Earth as a function of direction p , energy E and time t and the expected event rate is obtained by integrating the product of the instrumental response function $R(p,E,t|p,E,t)$ and the emitted intensity $I(p,E,t)$ over the direction p , energy E and time t . [15]

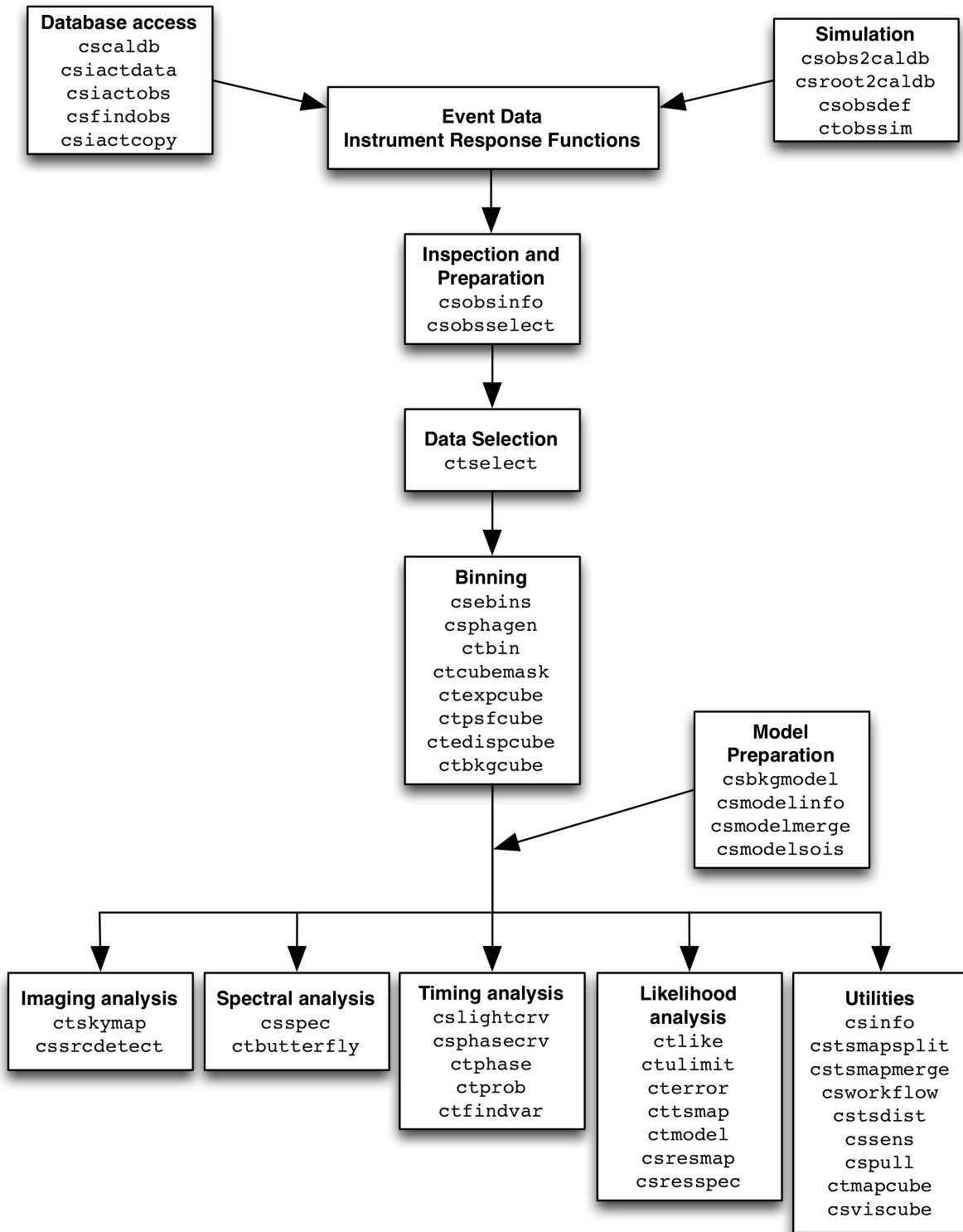


Figure 4.5: Overview of all the tools available in ctools. Credits: [32]

For CTA the IRFs are split into effective area $A_{eff}(p, E, t)$ [cm^2], point spread function (PSF)($p|p, E, t$), and energy dispersion $E_{disp}(E|p, E, t)$:

$$R(p, E, t|p, E, t) = A_{eff}(p, E, t) \times PSF(p|p, E, t) \times E_{disp}(E|p, E, t)$$

where

$$\int PSF(p|p, E, t) dp = 1$$

and

$$\int E_{disp}(E|p, E, t) dE = 1$$

The effective area relates the efficiency of the telescope with the observable area. It can be interpreted as the equivalent geometrical area of a perfect detector, obtained if throughout the detector surface the acceptance of events were of 100%:

$$A_{eff}(p, E, t) = \rho(p, E, t) \times A$$

where ρ is the detection probability of a gamma-ray with energy E , direction p and time t , and A is the total observable area. [6]

The Point Spread Function (PSF) gives the spatial probability distribution of the reconstructed events for a point source in the measured direction (p'). The probability distribution is:

$$\frac{dP}{d\Omega(r)}$$

where dP is the probability to find an event in a solid angle d at an offset r from the point source [12]. The PSF needs to be normalized, integrating to total probability:

$$\int \frac{dP}{d\Omega(r)} d\Omega = 1$$

The energy dispersion gives the true energy of the photon against the energies of the reconstructed events. In practice the energy dispersion is a matrix (FITS file) that stores $\frac{dP}{d\mu}$, a probability distribution function (PDF) for the energy migration as function of the true energy.

$$\mu = \frac{E_{recovery}}{E_{true}}$$

The energy dispersion also needs to be normalized:

$$\int_0^{\infty} \frac{dP}{d\mu} d\mu = 1$$

4.5 Methods

Here we will explain the main tools that we used to produce the light curves of the AGN KSP. One can download the data of the CTA DC-1 from here: (http://cta.irap.omp.eu/ctools/users/tutorials/1dc/getting_data.html). after downloading a folder will be available named 1dc whose internal structure is exhibited in the fig. 4.7:

Inside the caldb (calibration database) folder are stored the necessary IRFs for the analysis with CTA data. The simulated IRFs for DC-1 are exhibit in the table and correspond (are specific) to the array configuration that took a certain observation or dataset 4.4.

```

caldb/
caldb/data
caldb/data/cta
caldb/data/cta/1dc
caldb/data/cta/1dc/caldb.indx
caldb/data/cta/1dc/bcf
...
data/baseline/agn
data/baseline/agn/agn_baseline_510000.fits
data/baseline/agn/agn_baseline_510001.fits
...
data/
data/baseline/
data/baseline/egal
data/baseline/egal/egal_baseline_210000.fits
data/baseline/egal/egal_baseline_210001.fits
...
data/baseline/gc
data/baseline/gc/gc_baseline_310000.fits
data/baseline/gc/gc_baseline_310001.fits
...
data/baseline/gps
data/baseline/gps/gps_baseline_110000.fits
data/baseline/gps/gps_baseline_110001.fits
...
models/
models/models_agn.xml
models/models_egal.xml
models/models_gc.xml
models/models_gps.xml
...
obs/
obs/obs_agn_baseline.xml
obs/obs_egal_baseline.xml
obs/obs_gc_baseline.xml
obs/obs_gps_baseline.xml

```

Figure 4.6: 1dc folder structure. Inside the caldb folder is contained the instrument response functions that are necessary for the analysis of the simulated CTA data, in the data folder there is the calibrated, reconstructed and background reduced event data. The files `obs_agn_baseline.xml`, `obs_egal_baseline.xml`, `obs_gc_baseline.xml`, and `obs_gps_baseline.xml` are observation definition files containing a list of observations. Lastly the models folder contains the definitions of all source and background models that were used for simulating the data. Credits: [5]

First of all, to start the analysis you need to choose an event, the event data are split into observations, which for CTA are photon-counting event runs. Each event file is composed of event lists and a good time interval (GTI) binary table, which store the time between the start and stop of the observation. Below is shown an example of the structure of the event file:

In the header of the EVENTS one can find information about the observations, such as the name of the simulated sources, the duration of the observation as well as the date of

Response	Site	Duration	Configuration
South_z20_50h	South	50 hours	Baseline
South_z40_50h	South	50 hours	Baseline
North_z20_50h	North	50 hours	Baseline
North_z40_50h	North	50 hours	Baseline

Table 4.4: IRFs available in the first CTA Data Challenge for the northern and southern arrays, they were optimised for an exposure time of 50 hours and two different zeniths of 20 °and 40 °, specified in the IRF names respectively as z20 and z40.

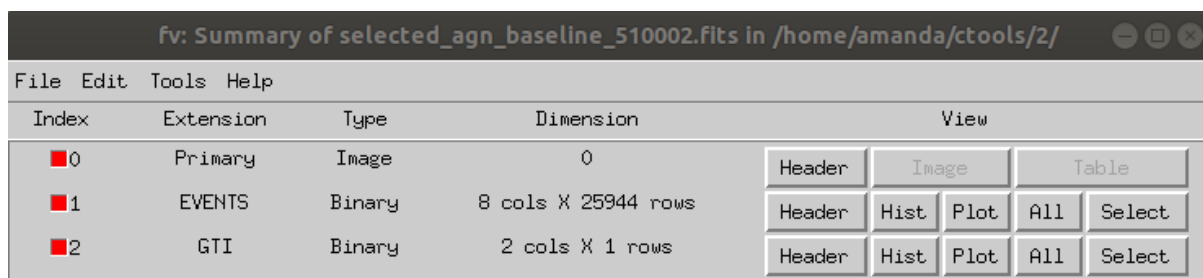


Figure 4.7: Format of the event file

start and stop of the observation, and the pointing direction in right ascension and declination. The good time interval (GTI) table is composed of two columns where each one represents the start and stop time successively, the time in GTI is given in MET (Mission Elapsed Time), measured in seconds. The correspond zero time is given in the header of each table in MJDREFF.

All the events in ctools are stored in observation definition files, which are ASCII files in XML format. After accessing the 1dc folder, you can find the observations of AGNs inside the observation folder in the obs_agn_baseline.xml. [5]

To start our analysis the first thing to do is select an event, for which we will use the *csobsselect* tool. In this tool one needs to give as input information the Region of Interest (ROI). As an example we will use the source PKS0716+714, which will guide us through the analysis. To use the *csobsselect* tool you just have to type it in the command line:

```
(cta) amanda@amanda:~\$ csobsselect
Input event list or observation definition XML file
[obs_agn_baseline.xml]
Pointing selection region shape (CIRCLE|BOX) [CIRCLE]
Coordinate system(CEL - celestial, GAL - galactic)(CEL|GAL)[CEL]
Right Ascension of selection centre (deg) (0-360) [110.471]
Declination of selection centre (deg) (-90-90) [71.3434]
Radius of selection circle (deg) (0-180) [5]
Start time (UTC string, JD, MJD or MET in seconds) [NONE]
```

Event selection	
CTA observation "AGN" (id=510002)	
Input filename	agn_baseline_510002.fits
Time range (MJD)	59215.5236111111-59215.5340277778 days
Time range (UTC)	2021-01-01T12:32:51 - 2021-01-01T12:47:51
Time range (MET)	662776440 - 662777340 seconds
Selected energy range	0.2 - 50 TeV
RoI of data	Centre(RA,DEC)=(110.472, 71.8434)deg, Radius=5 deg

Table 4.5: Output log event file from the `ctselect` tool. Where RoI is the region of interest which in this case is 5° around the central position of the source.

observation name	AGN id="510002
file	selected_agn_baseline_510002.fits
parameter name	Calibration
database	1dc
response	North_z40_50h

Table 4.6: Output XML file from the tool `ctselect` with details of each observation. Response specifies the instrument response function that applies to the event file. The IRF are stored in the `caldb` folder, its function is to classify the measured events into source and those attributed to any background.

Output observation definition XML file `[obs.xml]`

Overall this tool selected 3840 observations from the Extragalactic Survey containing a total of 104587675 events, then it wrote the events in another output list in an XML file, whose information will be used as input of the `ctselect` tool. `Ctselect` will select among the observed events the ones between the selected range of energy, as shown below:

```
(cta) amanda@amanda:~\$ ctselect
Input event list or observation definition XML file [obs.xml]
Radius of ROI around pointing or specified RA/DEC
(degrees) (0-180) [5]
Start time (UTC string, JD, MJD or MET in seconds) [MJD59200]
Stop time (UTC string, JD, MJD or MET in seconds) [MJD 59800]
Lower energy limit (TeV) [0.2]
Upper energy limit (TeV) [100]
Output event list or observation definition XML file [sel.xml]
```

This step returns an XML and a log file with the details of each observation as the name of the event, the range of time that the event was simulated for, and range of energy. A piece of both files are exhibited in the tables below 4.5 and 4.6:

After selecting the data, we want to visualise the corresponding sky map. To generate the sky map we use the `ctskymap` tool:

```
(cta) amanda@amanda: ~\ $ ctskymap
Input event list or observation definition XML file [sel.xml]
Coordinate system (CEL – celestial, GAL – galactic) (CEL|GAL)
[CEL]
Projection method(AIT|AZP|CAR|GLS|MER|MOL|SFL|SIN|STG|TAN)[CAR]
First coordinate of image center in degrees (RA or galactic l)
(0–360) [110.472]
Second coordinate of image center in degrees (DEC or galactic b)
(–90–90) [71.3434]
Image scale (in degrees/pixel) [0.02]
Size of the X axis in pixels [200]
Size of the Y axis in pixels [200]
Lower energy limit (TeV) [0.2]
Upper energy limit (TeV) [100]
Background subtraction method (NONE|IRF|RING) [IRF]
Output skymap file [sky.fits]
```

Subsequently, we want to identify the location of the source candidates; for that we use the tool *cssrcdetect*, which detects the source using a peak detection method on a smoothed version of the sky map. We need to choose a detection threshold such that only the most significant peaks above 10 sigma are retained.

```
(cta) amanda@amanda: ~\ $ cssrcdetect
Input sky map file [sky.fits]
Source model type (POINT) [POINT]
Background model type (NONE|IRF|AEFF|CUBE|RACC) [IRF]
Detection threshold (Gaussian sigma) [5]
Correlation kernel radius (deg) [0.1]
Output model definition XML file [det.xml]
Output DS9 region file [det.reg]
```

Using the SAOImage DS9 (<https://sites.google.com/cfa.harvard.edu/saoimageds9>) we open the generated sky map and load the point source model created with *cssrcdetect* tool (see fig. 4.8).

We then choose to perform an unbinned maximum likelihood analysis, because we expect that the number of events in each spatial bin to be small at high energies. The tool that executes the likelihood analysis is *ctlike*.

The likelihood function(L(M)) is the probability of obtaining the data given an input model. Ctlake performs the maximum likelihood estimation that best fits the model. The maximum likelihood estimation finds the best parameter that maximize the likelihood function, in this unbinned case, the Poisson formula:

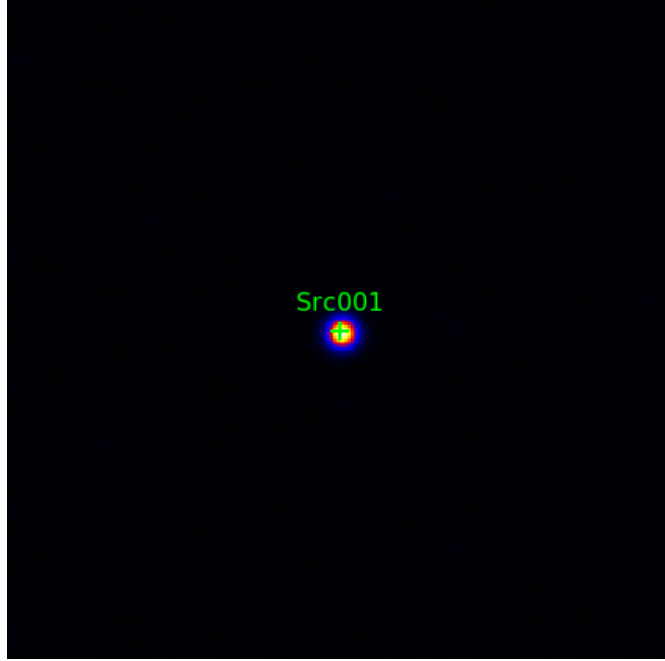


Figure 4.8: Sky map of the source PKS 0716+714

$$-\ln L(M) = E(M) - \sum_i \ln P(p_i, E_i, t_i | M)$$

where $\ln L(M)$ is the log-likelihood function. The sum is taken over all events i . $P(p, E, t | M)$ is the probability density that given the model M , an event with direction p , measured energy E and trigger time t occurs. $E(M)$ is the expected number of events to occur during an observation given the model M , computed by integrating the probability density over the trigger time, measured energy and instrument direction:

$$E(M) = \int GTI \int E_{bounds} \int ROIP(p, E, t | M) dp dE dt$$

where GTI are the Good Time Intervals defined in periods of time over which the data were taken, and the ROI is the Region of Interest (ROI). [11]

To execute the Maximum Likelihood Estimation, *ctlike* uses the algorithm Levenberg-Marquardt (see [10]). Since the Levenberg-Marquardt algorithm minimises a function, in this case $-\ln L(M)$.

Ctlike also calculates the significance of the source when requested. The TS is defined as:

$$TS = 2(\ln L(M_s + M_b) - \ln L(M_b))$$

where $\ln L(M_s + M_b)$ is the log-likelihood value obtained when fitting the source and the background together with the data, and $\ln L(M_b)$ is the log-likelihood value obtained when

fitting only the background model to the data. [11] To activate the test statistics we add the comand "tscal=1" in the output of the *cssrcdetect* tool. The output of this tool is exhibited below in table 4.7:

Source Type: Point Source	Source Name: Src001
Spectrum Type	
Power Law	
Parameter scale = 5.7e-18 name = Prefactor	
Parameter scale = -2.48 name = Index	
Parameter scale = 300000 name = Pivot Energy	
Spatial Type	
Point Source	
Parameter scale = 1.0 name = RA value = 110.502276381691	
Parameter scale = 1.0 name = DEC value = 71.3533974140418	
Source Name: Background	
Spectrum Type	
Power Law	
Parameter scale = 1 name = Prefactor	
Parameter scale = 0 name = Index	
Parameter scale = 1000000 name = Pivot Energy	

Table 4.7: Likelihood model of the source PKS0716+714 containing the source spectral parameters and the background. Where RA is the right ascension position of the source and DEC is the declination. The spectrum type of the source is described by a simple power law function where the pivot energy is the energy at which the function was normalized. To recovery the real values of the parameters they value needs to be multiplied by its correspondent parameter scale.

Then we run *ctlike* as below:

```
(cta) amanda@amanda:~\$ ctlike
Input event list, counts cube or observation definition XML file
[sel.xml]
Input model definition XML file [det.xml]
Output model definition XML file [like.xml]
```

Ctlike returns an XML file with the best fitting model parameters for every source with the significance value and the background:

Listing 4.1: Fitted model obtained with *ctlike* for the source PKS0716+714

```
<source name="Src001" type="PointSource" ts="287260.857"
tscal=1">
  <spectrum type="PowerLaw">
    <parameter name="Prefactor" value="31.2967365432705"
error="0.149133751112485"scale="5.7e-18"min="0"free="1"/>
    <parameter name="Index" value="1.40940515935952"
```

```

    error="0.00260219569086044" scale="-2.48"
    min="-4.03225806451613" max="4.03225806451613" free="1"/>
    <parameter name="PivotEnergy" value="1" scale="300000"
    free="0" />
</spectrum>
<spatialModel type="PointSource">
    <parameter name="RA" value="110.471171138739"
    error="0.000767507294198814" scale="1" free="1" />
    <parameter name="DEC" value="71.3433388568627"
    error="0.00024541538366295" scale="1" free="1" />
</spatialModel>
</source>
<source name="Background" type="CTAIrfBackground">
    <spectrum type="PowerLaw">
        <parameter name="Prefactor" value="0.999924750977184"
        error="0.000953441926747513" scale="1" min="0" free="1" />
        <parameter name="Index" value="-0.000212802922413001"
        error="0.000575502598176758" scale="1" min="-10"max="10"free="1"/>
        <parameter name="PivotEnergy" value="1" scale="1000000" free="0"/>
    </spectrum>
</source>]

```

To check that the model describes well the data we generate a residual map using the tool *csresmap*. This tool creates a residual map of the events from which the fitted model components were subtracted. To run the *csresmap* one can follow the prescription:

```

(cta) amanda@amanda:~\$ csresmap
Input event list, counts cube, or observation definition XML file
[sel.xml]
Input model definition XML file [like.xml]
First coordinate of image center in degrees (RA or galactic l) (0-360)
[110.472]
Second coordinate of image center in degrees (DEC or galactic b) (-90-90)
[71.3434]
Coordinate System (CEL|GAL) [CEL]
Projection method (AIT|AZP|CAR|GLS|MER|MOL|SFL|SIN|STG|TAN) [CAR]
Size of the X axis in pixels [200]
Size of the Y axis in pixels [200]
Pixel size (deg/pixel) [0.02]
Lower energy limit (TeV) [0.2]

```

```
Upper energy limit (TeV) [100]
Residual map computation algorithm (SUB|SUBDIV|SUBDIVSQRT|SIGNIFICANCE) [SIGNIFICANCE]
Output residual map file [res.fits]
```

To display the residual map we use ds9 again: (fig. 4.10)

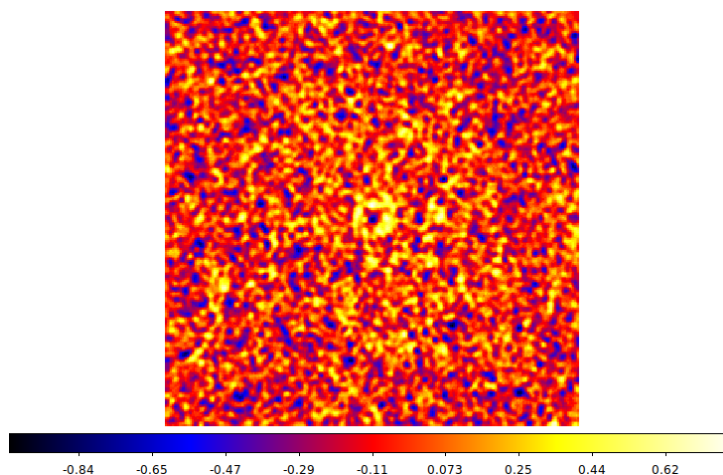


Figure 4.9: output of the csresmap tool

Through the residual map we can see that there is no obvious discrepancies in the residue, so we can say that the model reproduced well the data.

The light curves are produced with the **cslightcrv** tool. This script calculates a maximum likelihood analysis for every time bin from a time series, and generates a light curve. The input values that we use are:

```
(cta) amanda@amanda:~\$ cslightcrv
Input event list or observation definition XML file [sel.xml]
Input model definition XML file [like.xml]
Algorithm for defining time bins (FILE|LIN|GTI) [LIN]
Lightcurve start time (UTC string, JD, MJD or MET in seconds)
[MJD59200]
Lightcurve stop time (UTC string, JD, MJD or MET in seconds)
[MJD59800]
Number of time bins (1-10000) [100]
Analysis method (3D|ONOFF) [3D]
Source name [Src001]
Lower energy limit of events (TeV) [0.2]
Upper energy limit of events (TeV) [100]
Number of energy bins for binned(0=unbinned for 3D analysis
only)[0]
Output light curve file [lcrv.fits]
```

The output is a FITS file with values of TS, time and the fitted parameters of the model. We can use `fv` to displayed the header of the results file:

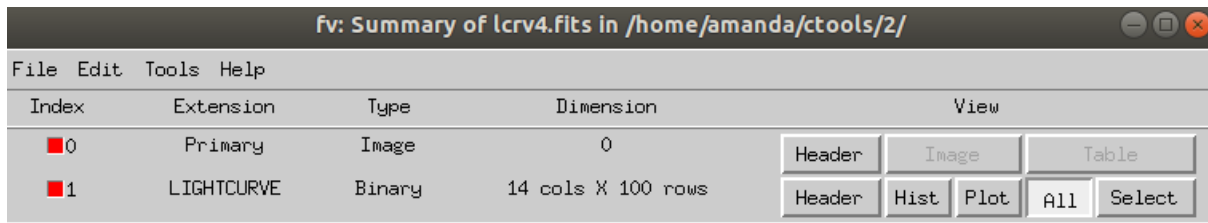


Figure 4.10: output of the `cslightcrv` tool

In the header of the Light curve table we can see all the information about the parameters, such as the units of prefactor, time, as well as number of columns and rows. (fig. 4.11)

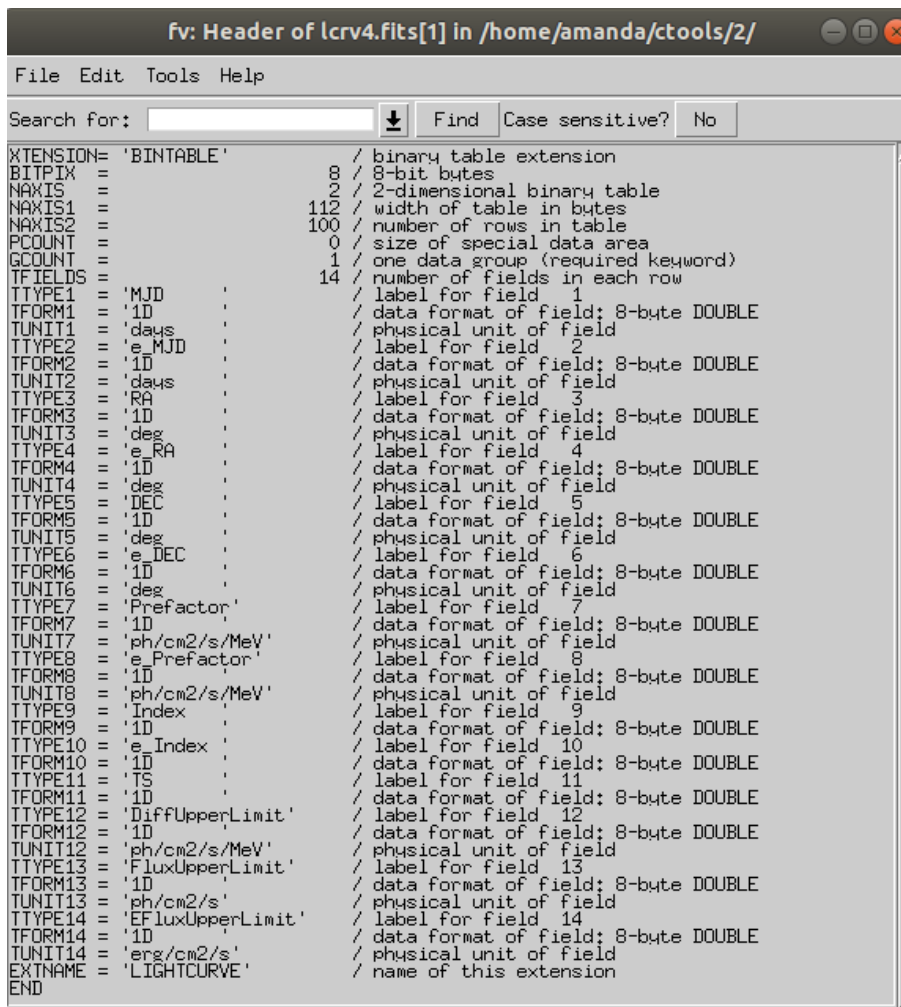


Figure 4.11: Header of the LIGHTCURVE table

We can plot the light curve using the script `show_lightcrv.py` that is located inside

the ctools example folder. This script requires matplotlib (<https://matplotlib.org/> installed). Then we just type:

```
amanda@amanda:~/ctools/share/examples/python show\_lightcurve.py
lcrv.fits
```

This script generates the light curve 4.12 below:

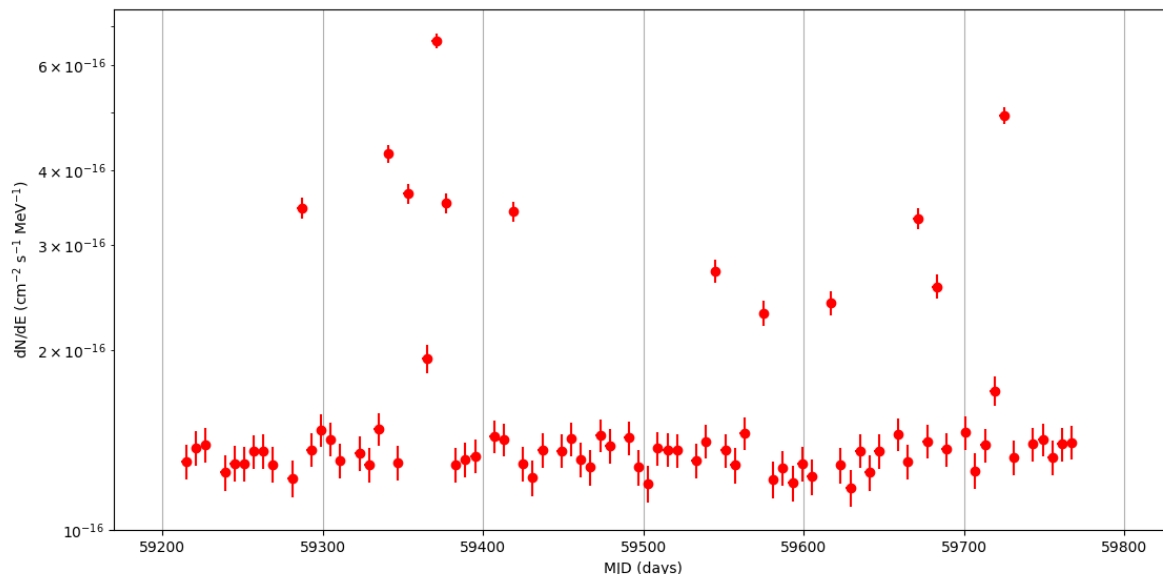


Figure 4.12: Light Curve of the source PKS0716+714 generated with ctools analysis

With the aim of comparing the ctools analysis results with the input model, we calculated the residuals between the light curves, to do this, first we had to calculate a weighted average among the time bins of the model, since in the analysis we had a regular time binning integration and in the model, the binning was irregular.

Below we plot the light curves of the analysis for each source, accompanied by the source model and the residuals.

As an example, we exhibit the light curve of the source PKS0716+714 analysed with ctools (red) and the simulated model (green) – fig. 4.13.

In general, to make the light curves, our first approach was to use the energy range from 0.2 to 100 TeV which does not require energy dispersion corrections due to the fact that the photons are more energetic, and energy reconstruction at these energies is good. Later, in order to perform an analysis which is more consistent with the modeled source, we lowered the energy threshold to 30 GeV and applied the full energy dispersion corrections in the analysis. This can be done by activating the command 'edisp' in ctlike:

```
(cta) amanda@amanda:~\$ ctlike edisp=yes
```

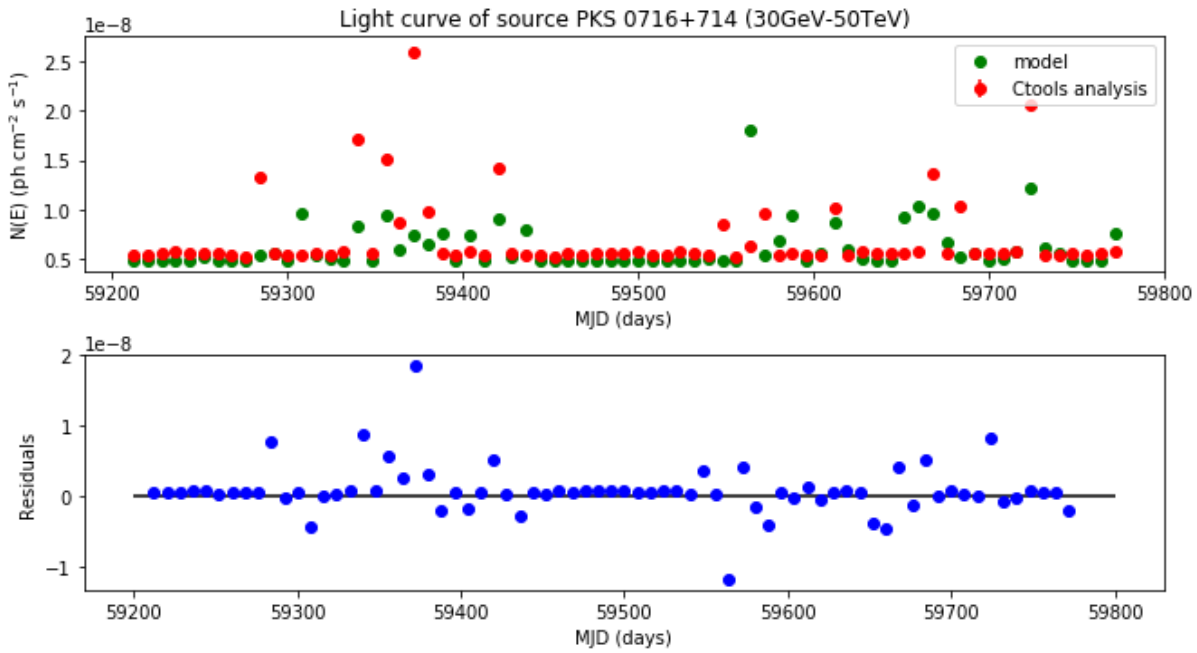


Figure 4.13: Light curve of the source PKS 0716+714

Input event list, counts cube or observation definition XML file [sel.xml]
 Input model definition XML file [det.xml]
 Output model definition XML file [like.xml]

Below we show the dispersion matrix plot (fig.4.14) produced with the migration energy values, which is the ratio between the reconstructed and the true photon energy for the source PKS0716+714:

Following the procedure outlined above, we produced all the light curves for the modelled sources in the data challenge, which are presented in the next section.

4.5.1 Light Curves

Throughout this section we used energy dispersion corrections for a complete analysis of the full energy-range light-curves down to 30 GeV. This is because some sources are not bright enough for detection above 200 GeV.

In general, the key values that we used in all sources to produce the light curves were: (see table 4.8)

Table 4.8: Light Curve parameters

Energy Range (TeV)	Radius (°)	Number of time bins	Detection threshold
0.03 to 100	5	100	5σ

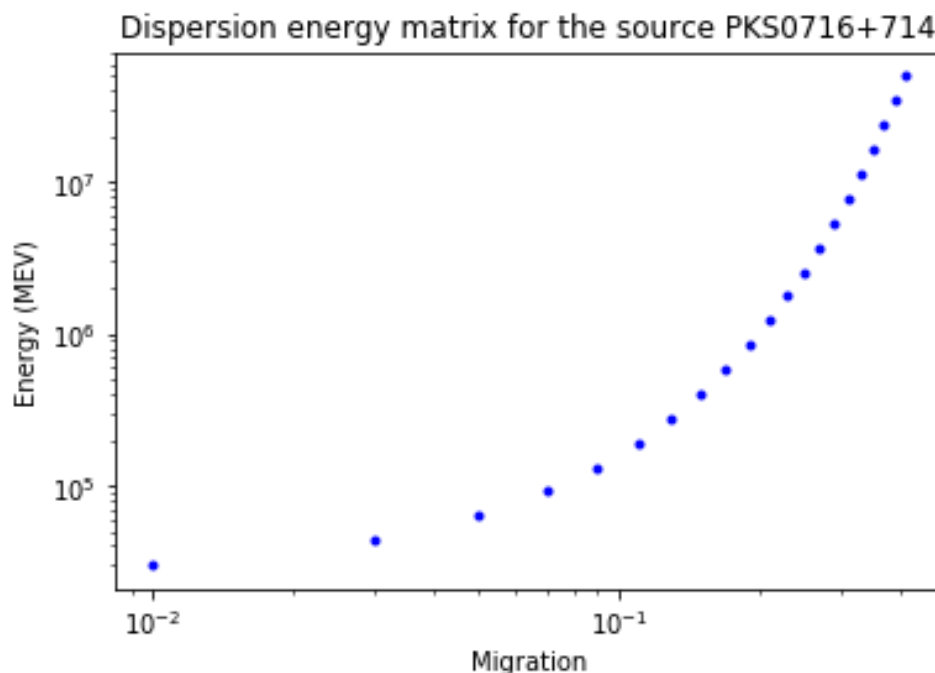


Figure 4.14: Energy dispersion matrix for the source PKS0716+714

We choose this energy range because this was the range in which the sources were simulated for the CTA database. 5° is approximately the field of view of the LST telescope, the dominant telescope for observations below 300 GeV. The time bins were chosen in a manner that was most adequate for the average source flux in the sample.

We created a python script to plot the light curves made with `ctools` together with the simulated models of each source to compare them and see if they have a good agreement. In the script, we created a function that calculates the flux and the upper limit of the analysis. The criteria used for flux detection in each light curve time bin was $TS > 9$, or least 3σ . Below we show the piece of the script used for the flux calculation:

```
def fluxo(lc): #calculates the flux of ctools analysis

    pivot_energy = 300000 #(Mev)
    emin = 30000 #(Mev)
    emax = 50000000 #(Mev)
    flux = []
    upper = []
    err = []
    for line in lc:
        ts = line[4]
        upperlim= line[5]
        prefactor = line[1]
```

```

index = line[2]
erroindex = line[3]
erroprefactor = line[7]

err =(math.sqrt((((pivot_energy**(index)*(-emax**(1+index)*prefactor*(1+(1+index))*np.log(pivot_energy)-(1+index)*np.log(emax))+((emin**(1+index)*prefactor*(1+(1+index))*np.log(pivot_energy)-(1+index)*np.log(emin)))/(1+index)**2))**2)*erroindex**2)+((((1/pivot_energy**index)*(np.power(emax,index+1)-np.power(emin,index+1))/(index+1))**2)*erroprefactor**2))))

if ts < 9:
    upper.append((line[0],upperlim,line[-2]))

else:
    prefactor = line[1]
    index = line[2]

    flux.append((line[0],prefactor*(1/pivot_energy**index)*(np.power(emax, index +1)-np.power(emin,index+1))/(index+1),err,index,erroindex))

return (np.asarray(upper),np.asarray(flux))

```

The python function created above 'fluxo()', returns a matrix with 3 columns, one with the time in MJD, the second with upper limit and the third with flux.

4.6 Results:

In this analysis we were able to detect all the 24 sources of the table 4.1. But we could only reproduce the light curves and compare with the model of some of them. The sources CGraBJ0211+1051, 4C14.23, BZUJ0742+5444, PKS0805-07, 4C+01.28, B31708+433, OT081 and BLLac were detect with $TS < 1$, and the sources PKS1830-211 and CGraBJ1849+6705 were detected with $TS < 21$, considering that the criteria for a reliable detection of the source is $TS > 25$, we believe that the detection of the sources mentioned above was actually an statistical random fluctuation. The sky map of all these sources are available in the Appendix A.

4.6.1 Source 3C66A:

We reproduced the light curve of the source 3C66A and through the light curve residuals(fig.4.15) we can see that the ctools analysis looks to overestimate the model. The residual map (fig.4.16) of this source showed that around the source position some negative and positive areas occur, which indicate that the analysis failed to make a good subtraction of the source. Using a complete energy dispersion analysis we found another source contributing for the flux of this event which we already suspected to be present and confused with 3C66A, due the irregularity found in the shape of the source.

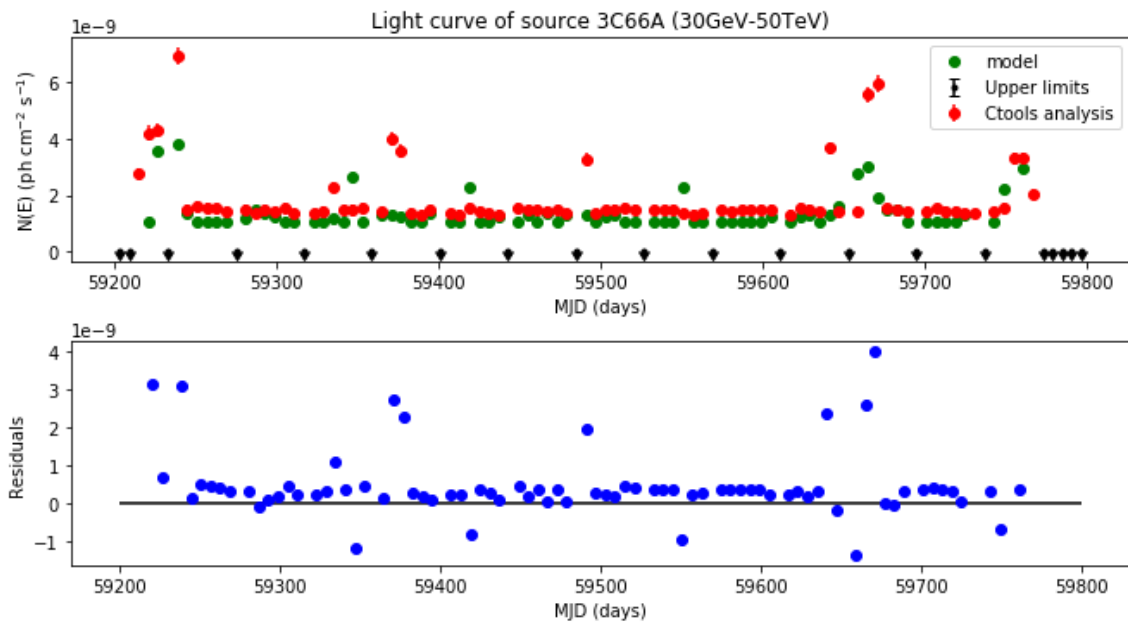


Figure 4.15: Light curve of the source 3C66A in 30GeV - 50TeV with energy dispersion.

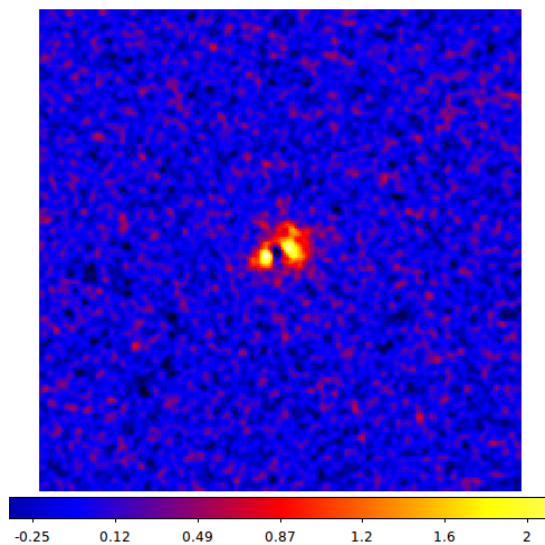
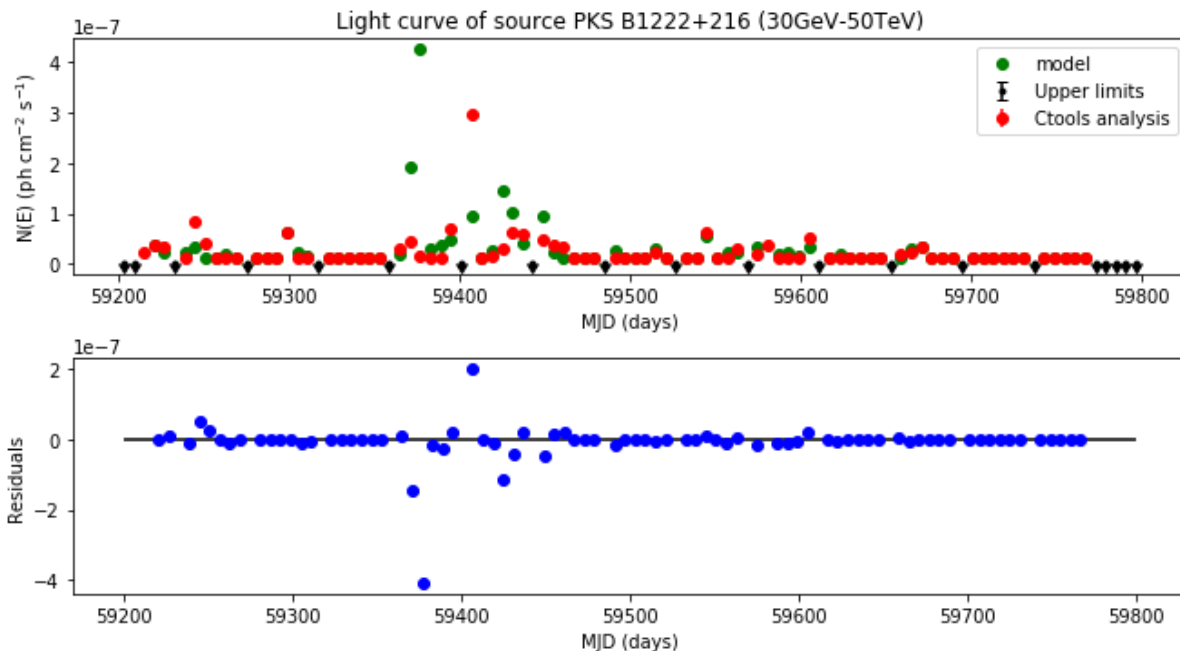


Figure 4.16: Residual map of the source 3C66A

4.6.2 Sources PKS0716+714, B1222+216, PKS1510-089, Mrk421, Ton 599, PMNJ2345-1555, 3C279, S41749+70, PKS 0454-234 and PKS 1424-41

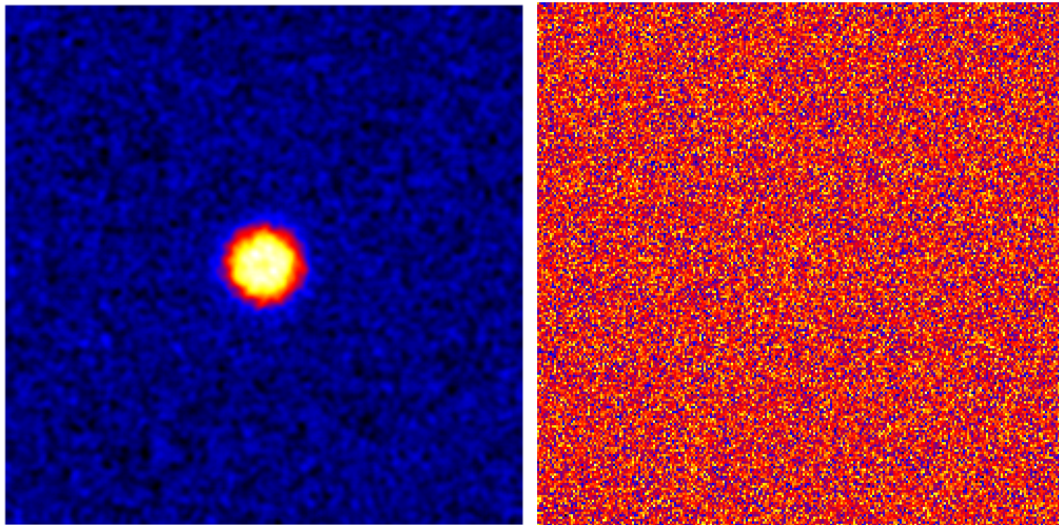
We were able to reproduce the light curve of all these detected sources using ctools, the light curves are available in appendix A. In general we notice that the reproduced light curves agree with the model, with exception of the moments when happens a flare. The algorithm has a failure in detect and subtract them. In addition, the sources PKS 1510-089, PKS 1424-41 and S41749+70 has the long term flux values slightly above the model, which indicates some bad subtraction of the background. In fact, with exception of source 3C279, all the other sources of this section, has a not very good residual sky map, showing some significant residual bright area in the position where the source is localized. In figure 4.18(a) we show an example of the residual map for the source B1222+216. Moreover, we reproduce this same analysis using ctools in high energies (100GeV -100TeV) and in this case, the residual map did not show any discrepancies see fig. 4.18(b) in the subtraction. Finally, we suggest that this bad subtraction is related with the fact that in low energies the angular resolution of CTA is not very good, as we show in the fig.4.6.2 for CTA North, this discrepancy will be reported for CTA AGN monitoring group for further investigation.

Figure 4.17: Light curve of the source B1222+216 with energy dispersion



4.6.3 Sources PKS1454-354, PKS2233-148 and PKS 1502+106

In the case of these sources there was no coincidence between the modeled period of the source and the observations. Therefore it is no possible to make a reasonable compari-



(a) Residual Map of the source B1222+216 in low energies (30GeV-50TeV)

(b) Residual Map of the source B1222+216 in high energies (100GeV-100TeV)

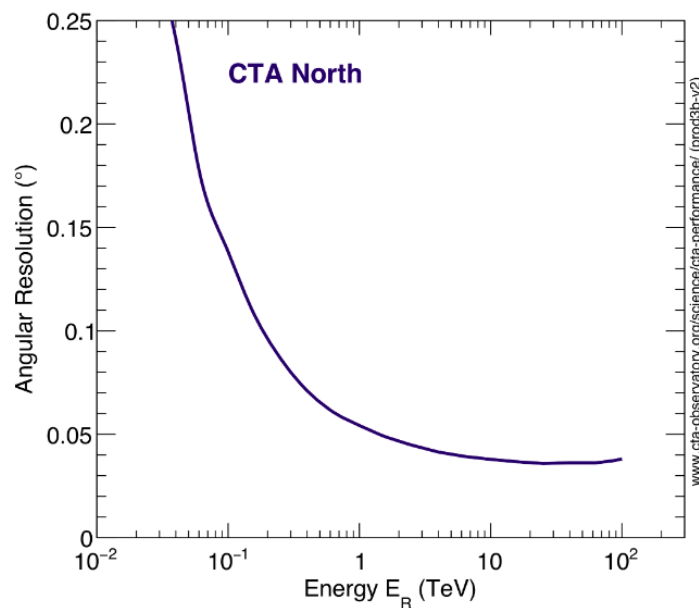


Figure 4.18: Angular Resolution of CTA North

son between them. Below we show an example of the light curve of the source PKS 2233-148 (see fig. 4.19) and the periods where the simulated model was available (see fig. 4.20).

Although the majority of the period of the simulated model was not available for us to compare it with the analysis, there are a few intervals accessible where we can comment both data for the sources PKS 1502+106 and for the source PKS 1454-354.

In the light curve of the both sources it is possible to notice that the light curve simulated did not correspond with the light curve of the analysis. In both cases our analysis has a considerable flux above the simulated one (see figs. 4.21, 4.6.3).

Through the spectra of the analyzed sources compared with the spectra of the simu-

Figure 4.19: Light curve of the source PKS2233-148 with energy dispersion

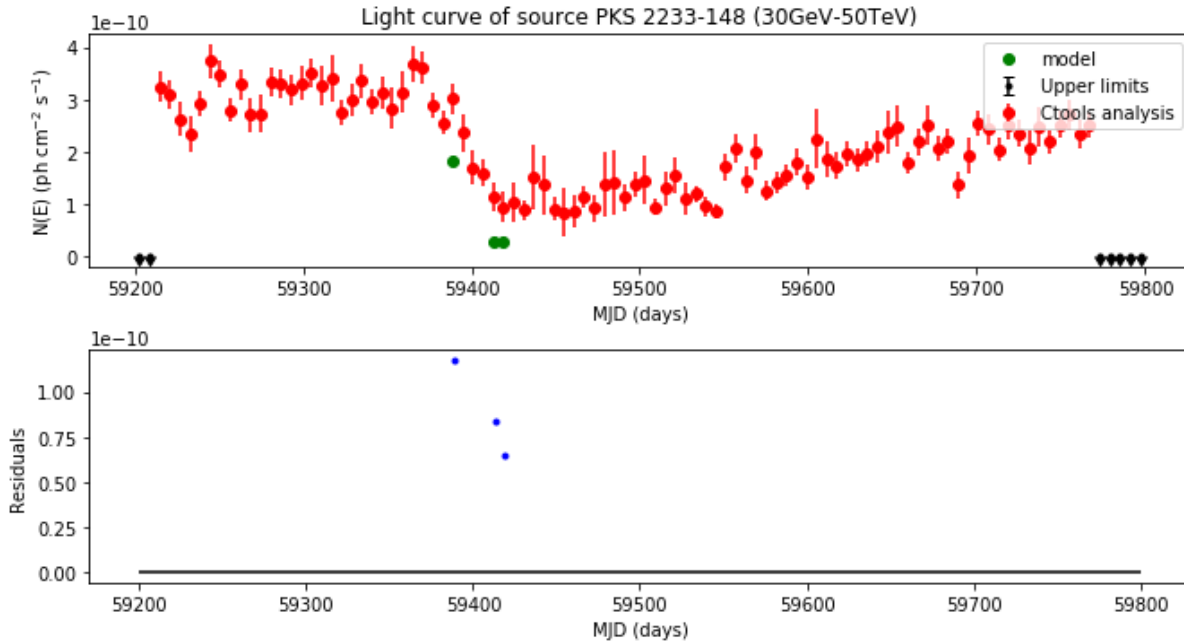
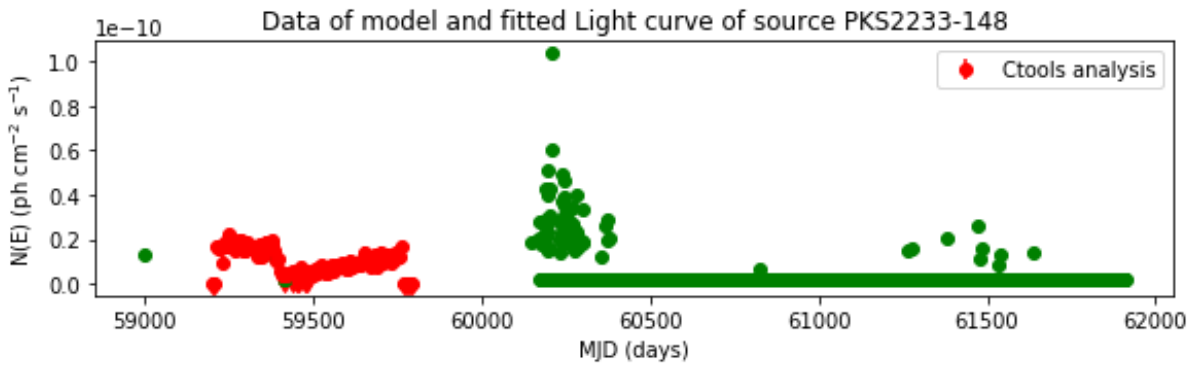


Figure 4.20: Data of the source PKS2233-148 available: model(green), analysis(red)



lated source we show the big discrepancy between them, demonstrating that there is some contamination in the source (see figs. 4.26(a), 4.25(a)). In fact the residual map of these sources is really bad confirming the bad subtraction performed by the algorithm (see figs. 4.26(b), 4.25(b)).

We also performed a spectral fit for these sources which reveals that the algorithm really did not subtracted the background in the analysis see fig. 4.26 as example for the source PKS 1454-354 remaining a relevant excess in low energies.

The results of these analysis will be reported for further investigations and possibles improvements in the algorithm.

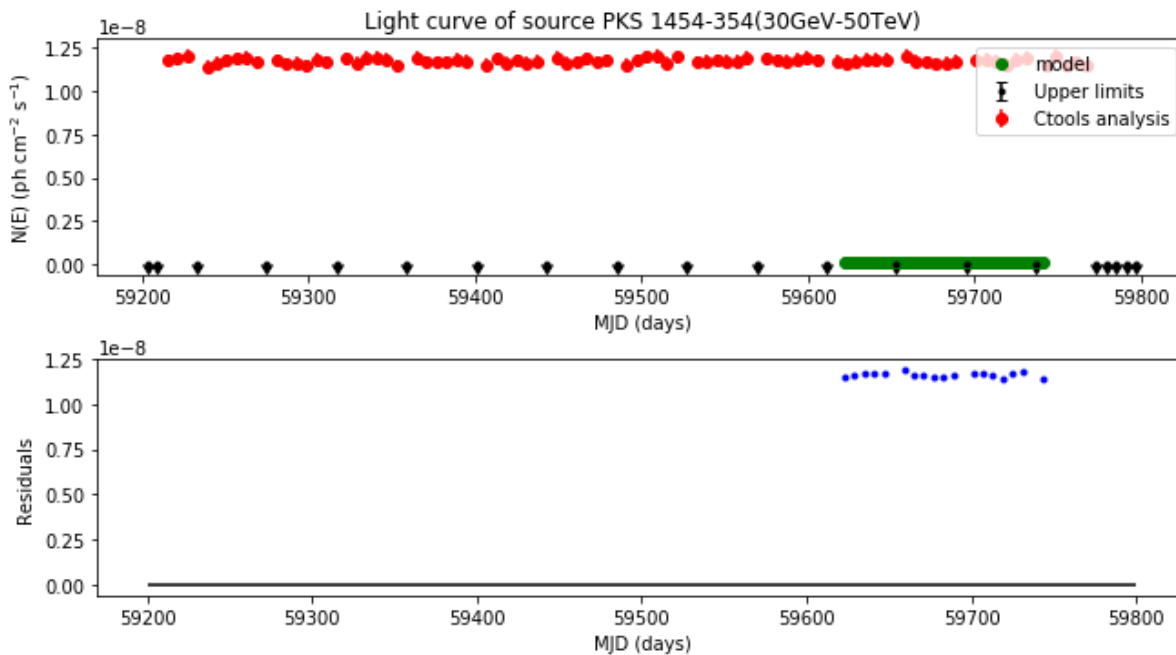


Figure 4.21: Light curve of the source PKS 1454-3541:

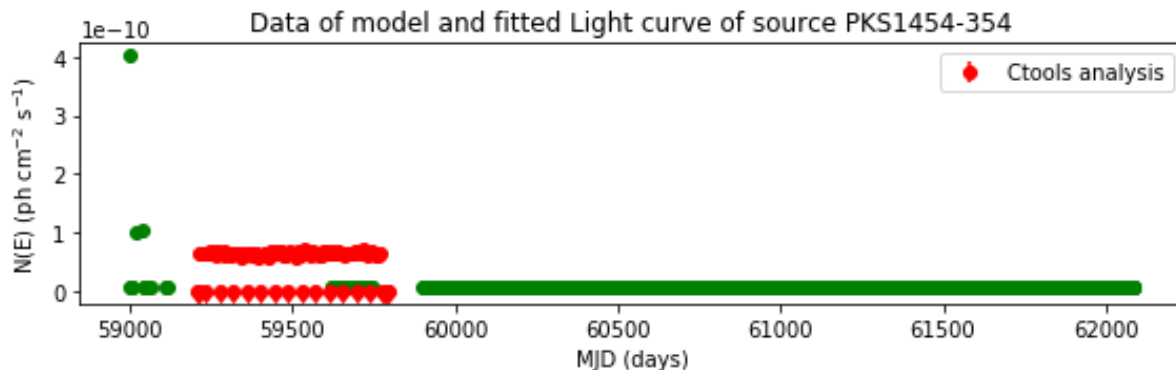


Figure 4.22: Data from the source PKS 1454-3541: model(green), analysis(red)

4.7 Discussion:

We can see in the light curves above that in general the analysis with ctools in long term is good, but it diverges from the simulated model during the flares, revealing some flaws in the algorithm during the detection and subtraction of them.

Another important consideration is about the excess found in the residual map at low energies. Besides the fact that the angular resolution of CTA is not very good at low energies, another possible explanation for this inaccuracy comes from the fact that the EBL was not simulated for all the simulated sources, only for the ones extracted from 1FHL catalog (see table 4.1).

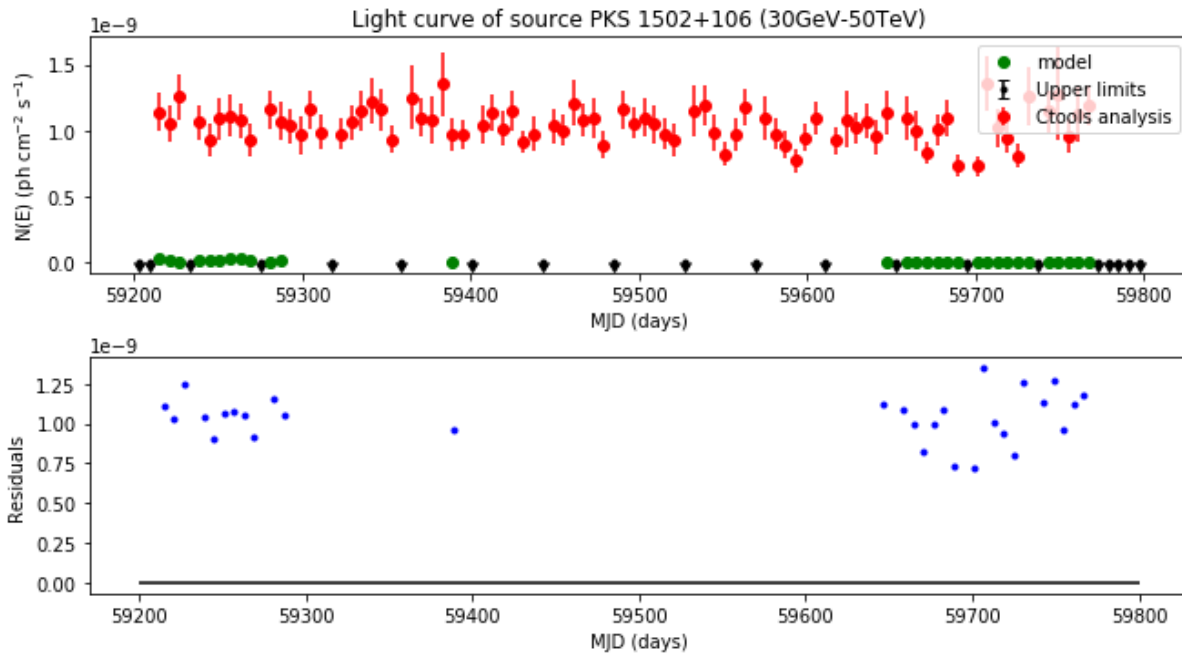


Figure 4.23: Light curve of the source PKS 1502+106

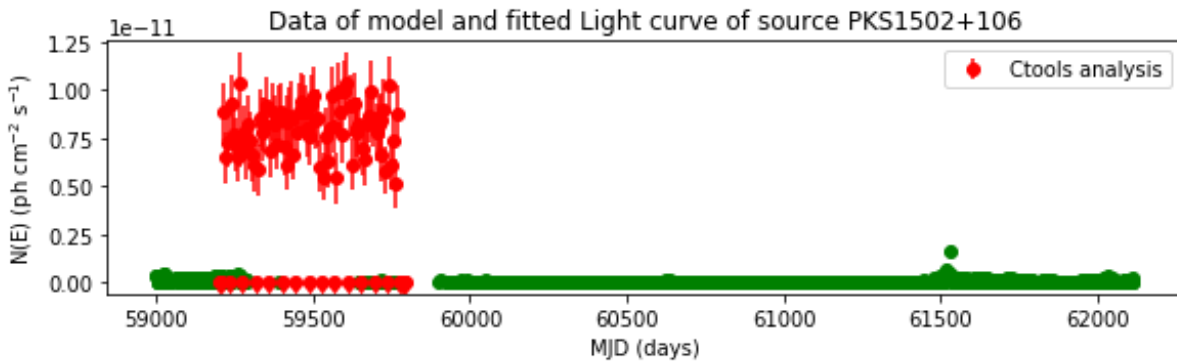
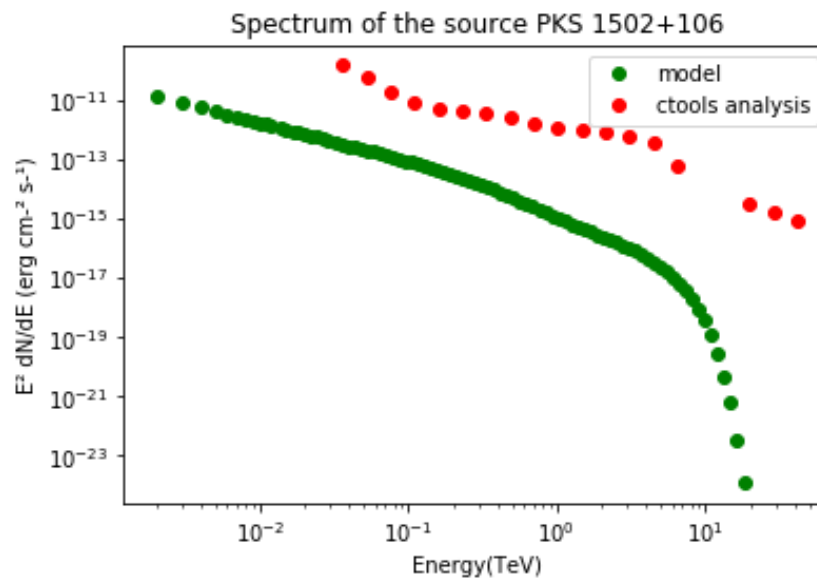
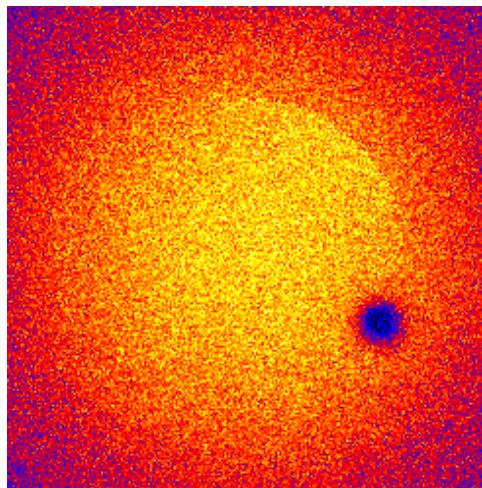


Figure 4.24: Data from the source PKS1502+106:model(green), analysis(red)

At the end, we were able to complete our goal which was contribute for the first CTA Data Challenge and test the analysis tools as well as reproduce the light curves of the sampled sources from table 4.1.

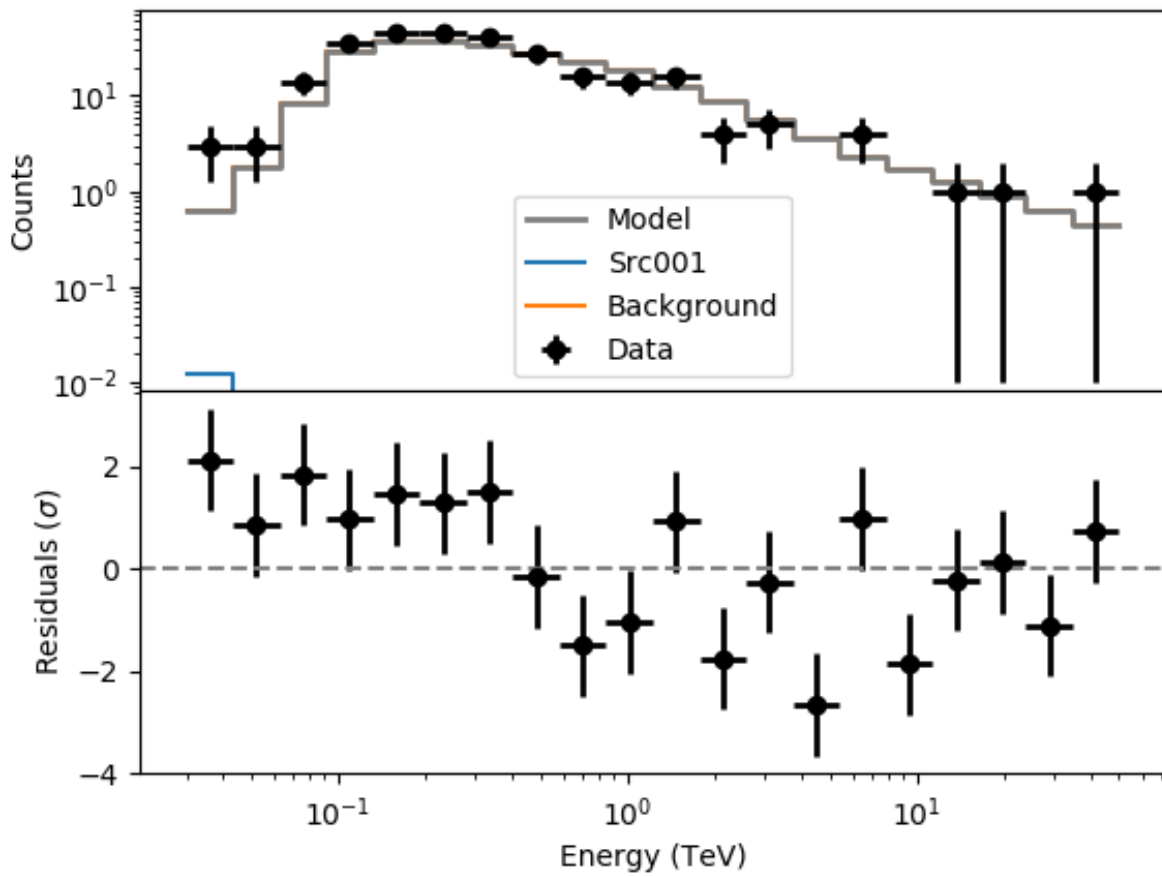


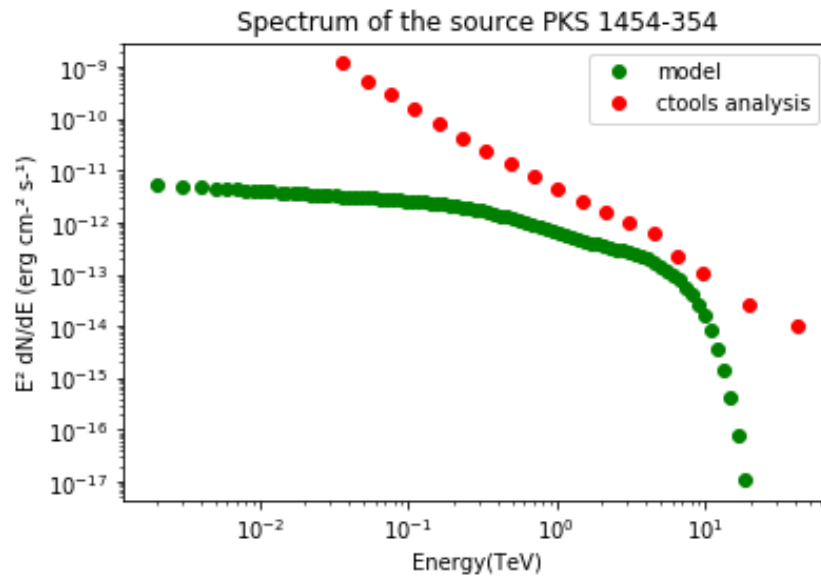
(a) Spectrum of the source PKS1502-106



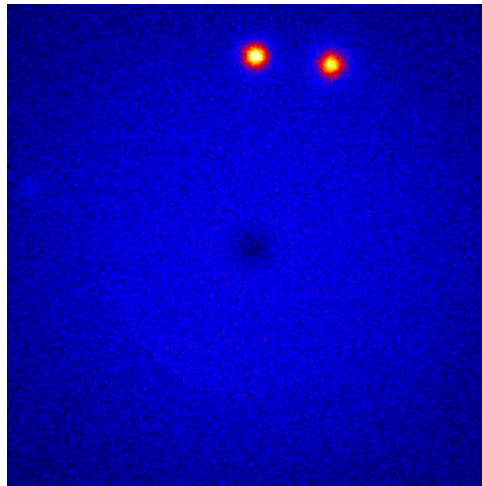
(b) Residual map of the source PKS1502-106

Figure 4.25: Residual fit of the source PKS 1502+106



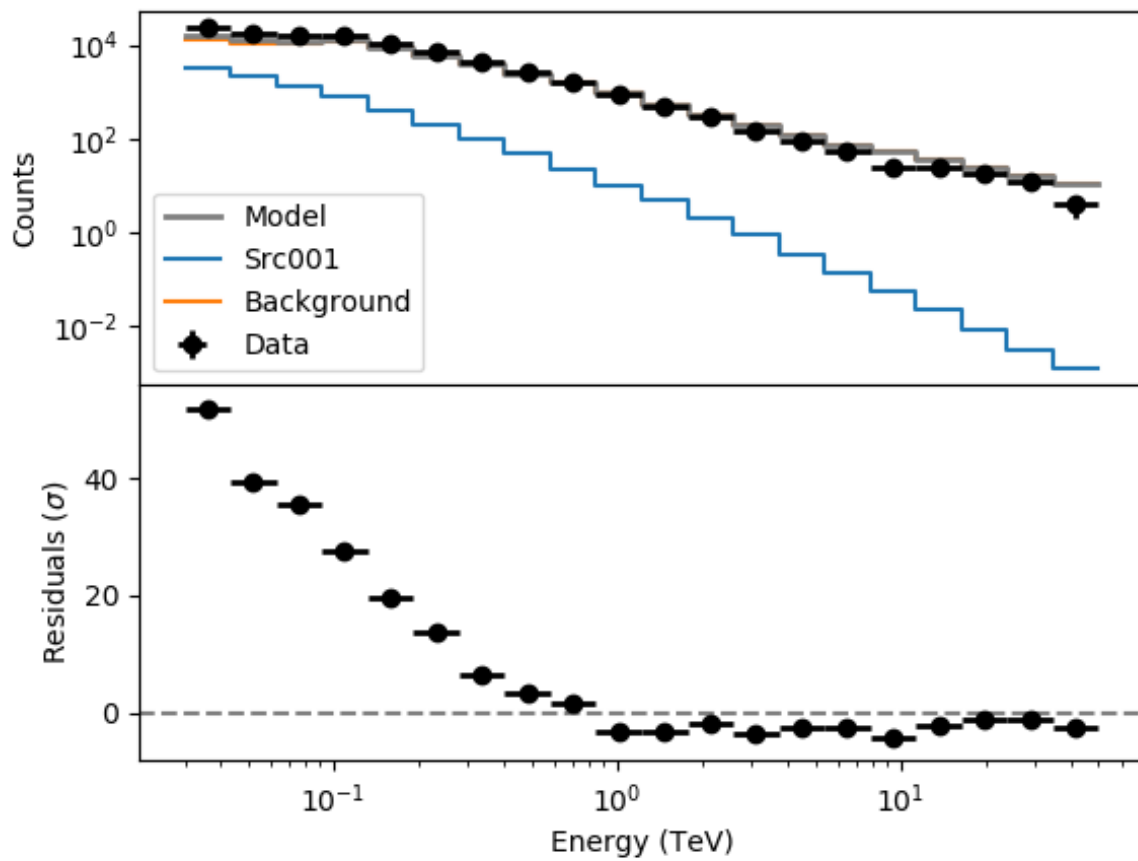


(a) Spectrum of the source PKS 1454-354



(b) Residual map of the source PKS 1454-354

Figure 4.26: Spectral fit of the source PKS 1454-354. The color black represents the data from the analysis and blue the simulated source



Chapter 5

Conclusion

The initial goal of this work was to participate in the first Data Challenge, therefore contributing to the preparation of the early science planning of CTA as well as the test and validation of the tools being prepared for the analysis of future CTA data. In our particular case, the collaboration task was focused on the case study of time series and variability analysis in AGNs, in which we successfully generated the light curves of the sources present in the CTA DC-1 sky model, using the ctools analysis suite.

With this set of analysis tools we were able to detect 14 of the 24 AGN sources present in the CTA sky model with good confidence. All of the detected objects were analysed within the full energy range of CTA, down to the low-energy threshold limit, where a complete energy dispersion analysis was included.

This allowed us to derive light curves and to evaluate the capabilities and shortcomings of the current CTA ctools analysis software, which still has some important flaws which needs improvement, according to the original goals of the DC-1. The majority of the discrepancies found in the analysis lie in the low-energy regime, where the detection algorithm was not able to resolve the source well, performing a bad background subtraction in the early-stage analysis, which resulted in a considerable amount of residual flux contaminating the source flux in the residual sky map. When performing an analysis at high energies for the same source, this discrepancy was not observed, constraining the problem to the reconstruction of the source in low energies.

Another important issue to consider in the future revision of the software is that the algorithm systematically missed some flares, as illustrated in the case of the source B1222+216. At other times the algorithm systematically overestimated the flares' fluxes, as in PKS 0716+714. This is due to the fact that, from the 24 simulated sources, only 16 were simulated including EBL absorption - the ones extracted from the 1FHL catalog (exhibit in table 4.1). We verified – although this was not present here for limitations on the time to conclude this work - that this factor can satisfactorily explain the recovered flux discrepancies in essentially all cases.

The results of this work will be made into a report for CTA and we aim to contribute

in the future DC-2 to implement part of the solutions to the issues identified.

When fully operational, CTA will detect more than one hundred VHE AGNs over the years of its KSP operation. The CTA AGN monitoring program will help us to study the physical processes that happens in these remarkable sources as well as understand their complex variability properties through its refined long-term light curves and high quality spectra. In this Master's Dissertation we took up the Consortium task of the DC-1 related to the AGN monitoring. This not only served as a relevant contribution to the preparatory work of the CTA Consortium towards its future operations, but formed the basis for the future continuation of our scientific, which will be dedicated to the planning and later the direct study of AGN variability with the CTA Observatory.

Appendix A

Light Curves

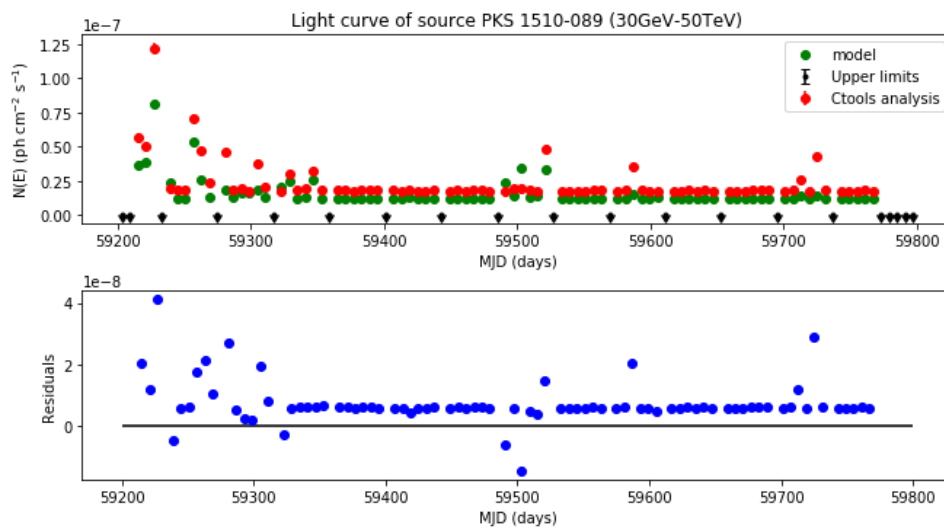


Figure A.1: Light curve of the source PKS1510-189. This analysis in general overestimate a little the simulated model during the long term component and during the flare.

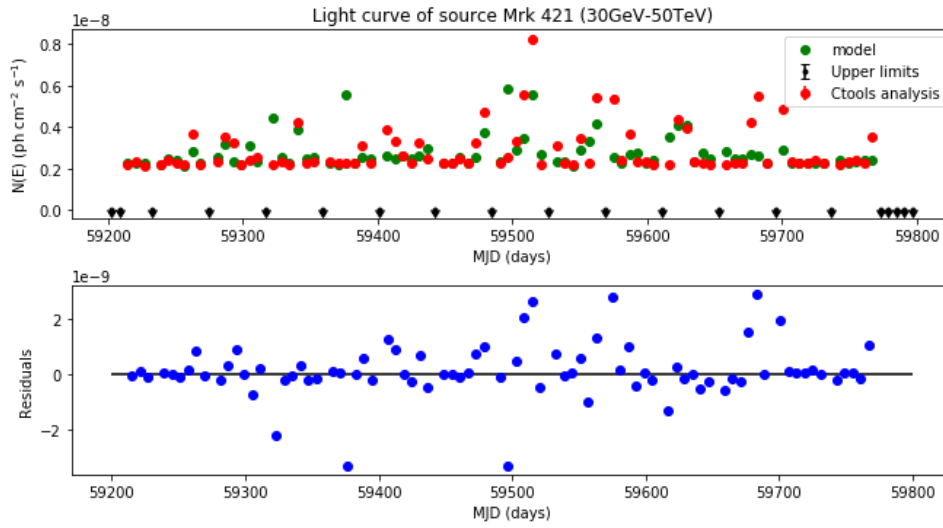


Figure A.2: Light curve of the source Mrk421. This light curve also shows a overestimation of the flux during the flares, revealing a problem in the algorithm during the background subtraction.

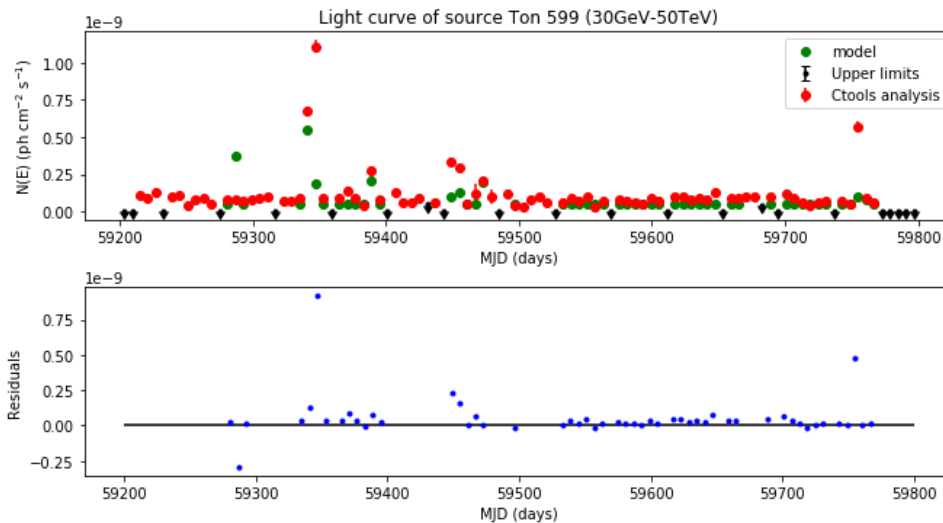


Figure A.3: Light curve of the source Ton 599. The long term component of this light curve is good, but the analysis overestimate the source during the flare

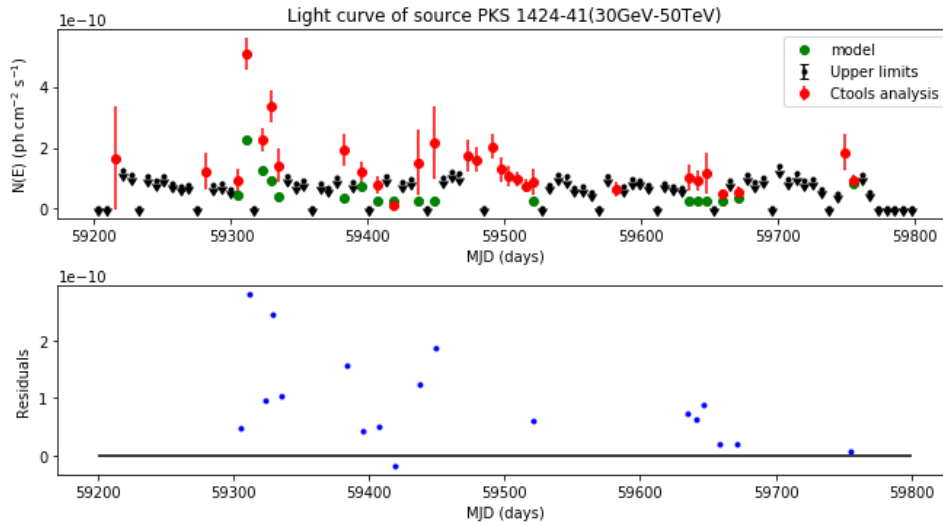


Figure A.4: Light curve of the source PKS1424-41. This light curve always overestimate the simulated model.

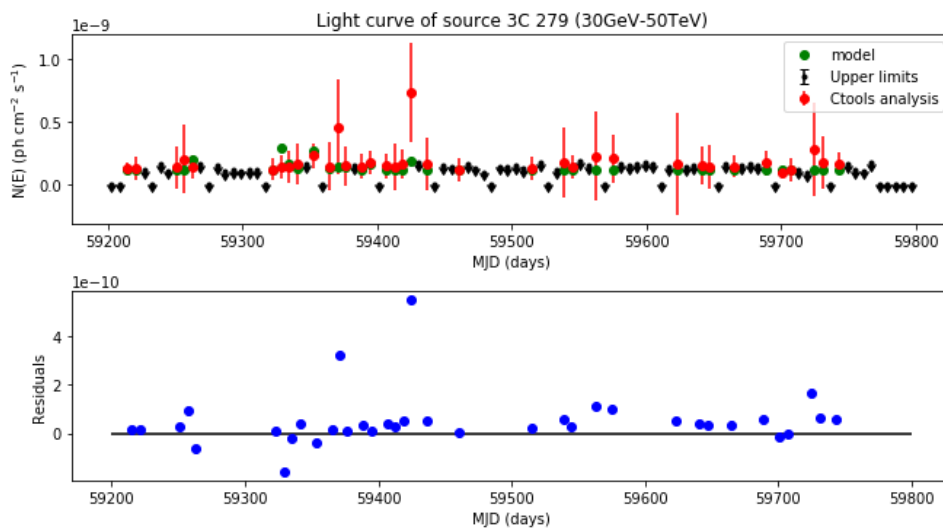


Figure A.5: Light curve of the source 3C279 with energy dispersion

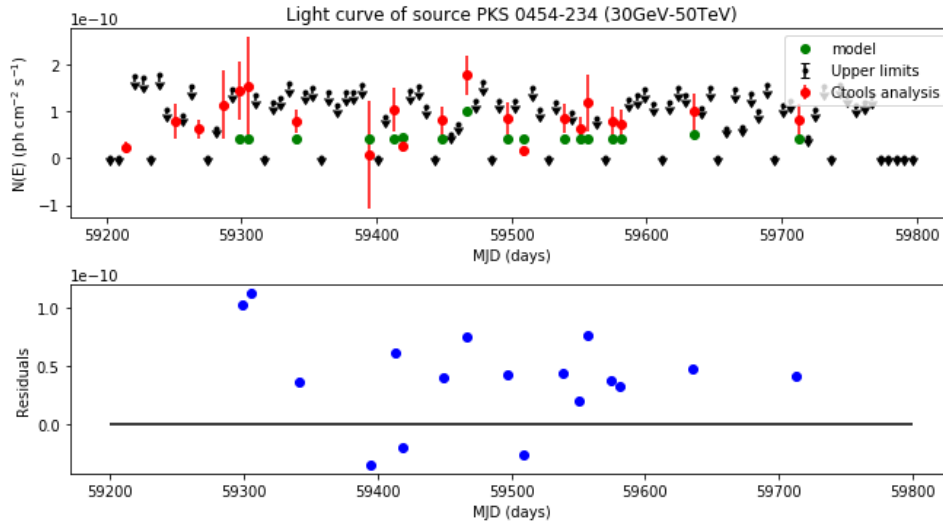


Figure A.6: Light curve of the source PKS 0454-234 with energy dispersion

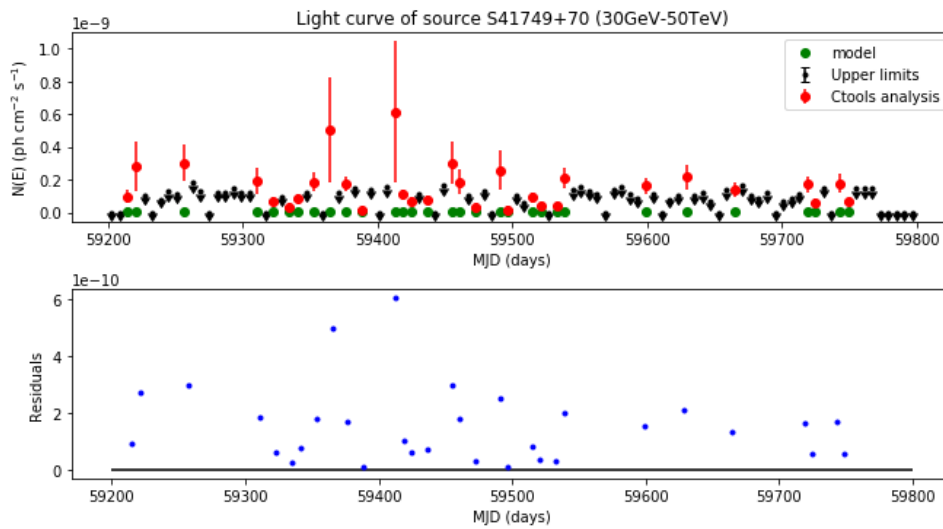
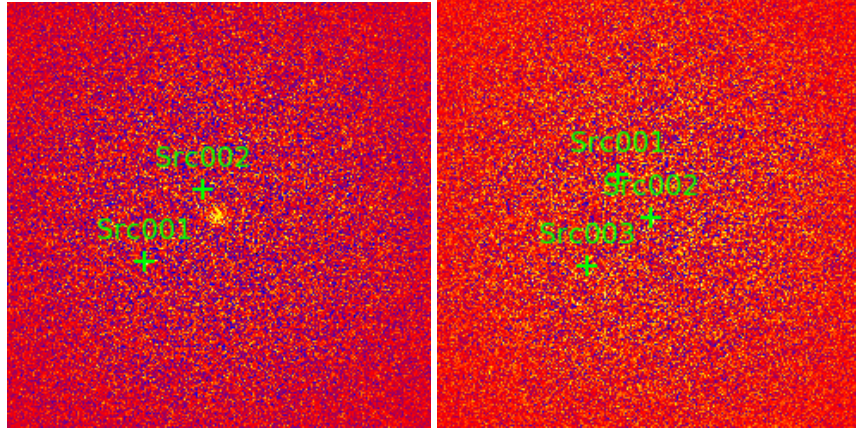
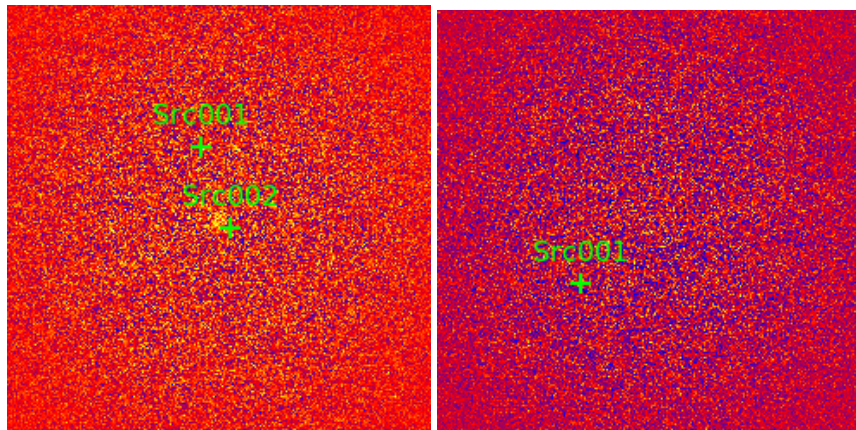


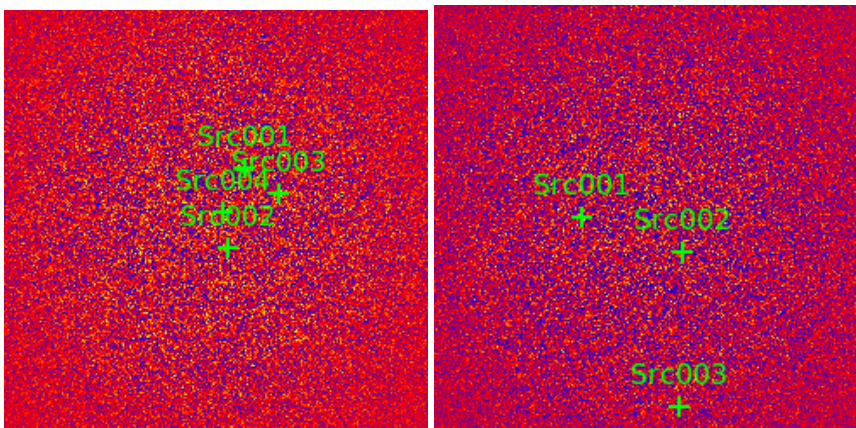
Figure A.7: Light curve of the source S41749+70.



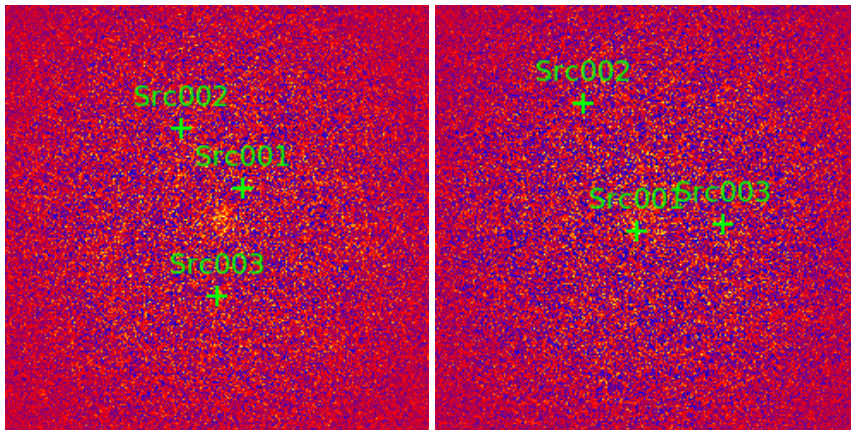
(a) Sky map of the source BZUJ0742. (b) Sky map of the source B31708+433.



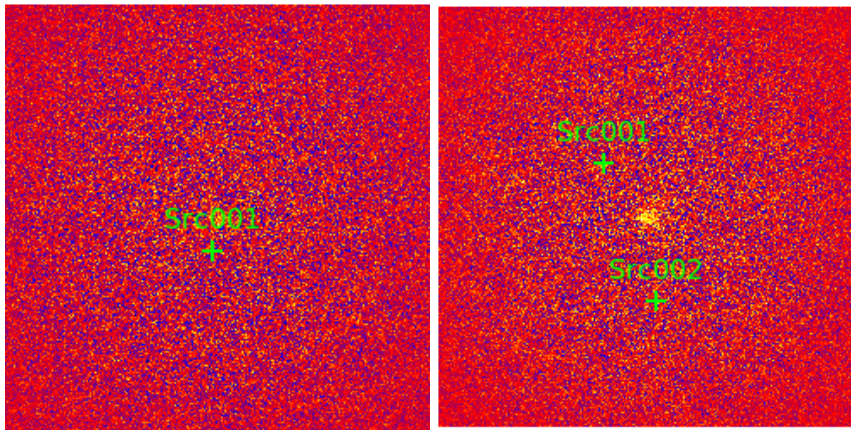
(c) Sky map of the source PKS1830 (d) Sky map of the source 4C14.23



(e) Sky map of the source PKS 0805-07 (f) Sky map of the source OT081



(a) Sky map of the source CGrabJ0211+1051. (b) Sky map of the source CGrabJ1849+6705.



(c) Sky map of the source 4C+01.28. (d) Sky map of the source BLLac

Bibliography

- [1] Cherenkov telescope array data using ctools. <http://userpages.irap.omp.eu/~ltibaldo>.
- [2] Circinus galaxy. <https://hubblesite.org/contents/media/images/2000/37/1010-Image.html>.
- [3] Cosmic-ray air showers. <https://www.mpi-hd.mpg.de/hfm/CosmicRay/Showers.html>. Accessed: 2020-03-03.
- [4] Cta technology. <https://www.cta-observatory.org/project/technology/>.
- [5] Data organisation. http://cta.irap.omp.eu/ctools/users/tutorials/1dc/data_organisation.html.
- [6] Effective area. https://gamma-astro-data-formats.readthedocs.io/en/latest/irfs/irf_components/index.html.
- [7] Glimpsing the hearts of galaxies. <https://astronomy.com/magazine/2019/02/glimpsing-the-heart-of-galaxies>.
- [8] Implementation. http://cta.irap.omp.eu/ctools/users/user_manual/models_implementation.html. Accessed: 2020-04-05.
- [9] The jets in m87. <https://www.eso.org/public/brazil/images/eso9203a/>.
- [10] Levenberg-marquardt algorithm. http://cta.irap.omp.eu/ctools/users/user_manual/likelihood.html.
- [11] Maximum likelihood estimation. http://cta.irap.omp.eu/ctools/users/user_manual/likelihood.html.
- [12] Point spread function. http://cta.irap.omp.eu/ctools/users/user_manual/irf_cta.html.
- [13] Scope of first cta data challenge. <http://cta.irap.omp.eu/ctools/users/tutorials/1dc/scope.html?highlight=ksp>.
- [14] Unified model of agn. <https://fermi.gsfc.nasa.gov/science/eteu/agn/>.

- [15] What are instrument response functions? http://cta.irap.omp.eu/ctools/users/user_manual/irf_intro.html.
- [16] F. Aharonian, J. Buckley, T. Kifune, and G. Sinnis. High energy astrophysics with ground-based gamma ray detectors. *Reports on Progress in Physics*, 71(9):096901, September 2008.
- [17] F. Aharonian, J. Buckley, T. Kifune, and G. Sinnis. High energy astrophysics with ground-based gamma ray detectors. *Reports on Progress in Physics*, 71(9):096901, 2008.
- [18] J. A. Baldwin, M. M. Phillips, and R. Terlevich. Classification parameters for the emission-line spectra of extragalactic objects. , 93:5–19, February 1981.
- [19] Ulisses Barres de Almeida. *Physics from Time Variability of the VHE Blazar PKS 2155-304*. PhD thesis, -, October 2010.
- [20] W. Benbow, C. Boisson, L. Costamante, O. de Jager, G. Dubus, D. Emmanoulopoulos, B. Giebels, S. Pita, M. Punch, C. Raubenheimer, M. Raue, H. Sol, and S. Wagner. A spectacular vhe gamma-ray outburst from pks 2155-304 in 2006, 2007.
- [21] Markus Böttcher. Modeling the emission processes in blazars. In *The Multi-Messenger Approach to High-Energy Gamma-Ray Sources*, pages 95–104. Springer, 2007.
- [22] cta Consortium et al. Science with the cherenkov telescope array. *Science with the Cherenkov Telescope Array*, 2019.
- [23] Charles Dennison Dermer and Berrie Giebels. Active galactic nuclei at gamma-ray energies. *Comptes Rendus Physique*, 17(6):594 – 616, 2016. Gamma-ray astronomy / Astronomie des rayons gamma - Volume 2.
- [24] David J Fegan. /hadron separation at tev energies. *Journal of Physics G: Nuclear and Particle Physics*, 23(9):1013, 1997.
- [25] Bruno Fontes Souto. *Configurações para um Arranjo de Telescópios Cherenkov por Otimização Evolutiva Multiobjetivo*. PhD thesis, 2018.
- [26] A. Franceschini, G. Rodighiero, and M. Vaccari. Extragalactic optical-infrared background radiation, its time evolution and the cosmic photon-photon opacity. , 487(3):837–852, 2008.
- [27] Christian Fruck. *The Galactic Center resolved with MAGIC and a new technique for Atmospheric Calibration*. PhD thesis, Technische Universität München, 2015.
- [28] T. M. Heckman. An optical and radio survey of the nuclei of bright galaxies. Activity in normal galactic nuclei. , 500:187–199, July 1980.

- [29] A Michael Hillas. Cherenkov light images of eas produced by primary gamma. 1985.
- [30] Walter Jaffe, Holland Ford, Laura Ferrarese, Frank van den Bosch, and Robert W. O'Connell. The Nuclear Disk of NGC 4261: Hubble Space Telescope Images and Ground-based Spectra. , 460:214, March 1996.
- [31] John Vernon Jelley. *Cherenkov radiation and its applications*. Pergamon, London, 1958.
- [32] Jea Knödlseder, M Mayer, C Deil, J-B Cayrou, E Owen, N Kelley-Hoskins, C-C Lu, R Buehler, F Forest, T Louge, et al. Gammalib and ctools-a software framework for the analysis of astronomical gamma-ray data. *Astronomy & Astrophysics*, 593:A1, 2016.
- [33] Jürgen Knödlseder, Luigi Tibaldo, Domenico Tiziani, A Specovius, Josh Cardenzana, Michael Mayer, Nathan Kelley-Hoskins, Leonardo Di Venere, Simon Bonnefoy, Andreas Ziegler, et al. Analysis of the hess public data release with ctools. *Astronomy & Astrophysics*, 632:A102, 2019.
- [34] Jürgen Knödlseder. The cherenkov telescope array, 2020.
- [35] S Lombardi, O Catalano, S Scuderi, LA Antonelli, G Pareschi, E Antolini, L Arrabito, G Bellasai, K Bernlöhr, C Bigongiari, et al. First detection of the crab nebula at tev energies with a cherenkov telescope in a dual-mirror schwarzschild-couder configuration: the astri-horn telescope. *Astronomy & Astrophysics*, 634:A22, 2020.
- [36] Rachel E Mason. Dust in the torus of the agn unified model. *Planetary and Space Science*, 116:97–101, 2015.
- [37] Paolo] Padovani.
- [38] Paolo Padovani. The faint radio sky: radio astronomy becomes mainstream. *Astron. Astrophys. Rev.*, 24(1):13, 2016.
- [39] Paolo Padovani. On the two main classes of active galactic nuclei. *Nature Astronomy*, 1(8), Jul 2017.
- [40] Paolo Padovani, DM Alexander, RJ Assef, B De Marco, P Giommi, RC Hickox, GT Richards, Vernesa Smolčić, E Hatziminaoglou, V Mainieri, et al. Active galactic nuclei: what's in a name? *The Astronomy and Astrophysics Review*, 25(1):2, 2017.
- [41] Bradley M. Peterson. *An Introduction to Active Galactic Nuclei*. 1997.
- [42] MJ Rees. The m87 jet: internal shocks in a plasma beam? *Monthly Notices of the Royal Astronomical Society*, 184(1):61P–65P, 1978.
- [43] George B Rybicki and Alan P Lightman. *Radiative processes in astrophysics*. John Wiley & Sons, 2008.

- [44] Peter Schneider. *Extragalactic Astronomy and Cosmology*. 2006.
- [45] C. Megan Urry and Paolo Padovani. Unified schemes for radio-loud active galactic nuclei. *Publications of the Astronomical Society of the Pacific*, 107:803, sep 1995.
- [46] RM Wagner. Synoptic studies of 17 blazars detected in very high-energy γ -rays. *Monthly Notices of the Royal Astronomical Society*, 385(1):119–135, 2008.
- [47] Robert Marcus Wagner. Measurement of very high energy gamma-ray emission from four blazars using the magic telescope and a comparative blazar study. *Publications of the Astronomical Society of the Pacific*, 119(860):1201–1203, 2007.